NONINVASIVE DIAGNOSIS AND TREATMENT OF IN SITU EARLY-STAGE CANCERS ASSISTED BY BIOMIMETIC NANOPLATFORMS

HUANG XIAZI

PhD

The Hong Kong Polytechnic University

2023

The Hong Kong Polytechnic University

Department of Biomedical Engineering

Noninvasive diagnosis and treatment of in situ early-stage cancers assisted by biomimetic nanoplatforms

HUANG Xiazi

A thesis submitted in partial fulfilment of the requirements for the degree of Doctor of Philosophy

March 2023

CERTIFICATE OF ORIGINALITY

I hereby declare that this thesis is my own work and that, to the best of my knowledge and belief, it reproduces no material previously published or written, nor material that has been accepted for the award of any other degree or diploma, except where due acknowledgement has been made in the text.

_____ (Signed)

__ HUANG Xiazi_____ (Name of student)

ABSTRACT

Cancer claims nearly 10 million lives each year and is the second leading cause of death worldwide. Increasing the rate of early diagnosis could considerably increase the 5-year survival rate from 26% to 91%. At present, the ultimate standard for clinical diagnosis of cancer is the pathological section, which depends on the localization and preliminary judgment of imaging diagnosis, and usually reflects advanced stages of development. It is clinically impactful if the changes in the tumor microenvironment and biological organization in the early stage of cancer can be sensed and identified. That said, these microenvironment changes are subtle and difficult to be accurately identified with existing imaging techniques. Therefore, early, stable, and reliable imaging modalities play a crucial role in cancer diagnosis and therapy. In recent years, innovative imaging methods have been explored to achieve higher sensitivity, specificity, and accuracy, improving the state of the art for early diagnosis and therapy-efficacy detection of tumors.

In this thesis, to achieve early theranostic of tumors, we explored the application of two new imaging methods, photoacoustic imaging (PAI) and magnetic particle imaging (MPI), combined with functional optimization of imaging contrast agents. Aiming at the challenges of poor targeting ability, immune rejection, and poor biocompatibility of contrast agents, a set of strategies of cell membrane modification were proposed to enhance the imaging performance.

Firstly, we utilized PAI that combines the advantages of optical imaging and ultrasound imaging to achieve deep-tissue (liver) penetration and high-contrast imaging. The abundant sinusoids in the liver provides a strong background photoacoustic (PA) signal, and the liver, the main organ of the immune system, traps many nanoprobes in order to remove foreign substances, greatly reducing the signal-to-noise ratio (SNR). Therefore, we proposed to use the erythrocyte membrane to modify gold nano-stars to prolong the

circulation time of the nanoprobes *in vivo* to enhance the enrichment of the nanoprobes in tumors. Owing to the immune-escaping property from the erythrocyte membrane, we successfully verified that the functionalized gold nano-stars can assist PAI to detect small tumors up to 2 mm in diameter in the liver, demonstrating the biomimetic nanoplatforms are phenomenal in cancer theranostic.

However, the accumulating effect of nanoprobes in brain glioma imaging is still unsatisfactory due to the presence of the blood-brain barrier (BBB), which impedes the delivery of theranostic agents to the tumor site. Therefore, to improve the BBB penetration and active targeting properties of the nanoprobes, homologous tumor cell membranes were extracted and coated with magnetic nanoparticles (MNPs). In this thesis, we demonstrated depth-independent and highly sensitive MPI as well as its usage as a precise and quantitative imaging method, as its signal comes directly from the magnetic moment of MNP with no background signal interference.

In the first two works, we demonstrated the promising performance of the biomimetic NPS for early diagnosis of cancers. Moreover, their safety in *in-vivo* and non-invasive photothermal therapy could also be achieved. In the experiments, the heterogeneity of tumors and individual differences among patients will lead to differences in treatment efficacies, and new drug delivery methods were hence explored in this thesis. In addition to assessing the efficacy by studying the recovery from cancer, it is desirable to visualize the delivery of drugs during treatment process. Therefore, in the third study, we used PAI to monitor drug delivery in real time, providing valuable information on the distribution and concentration of the drugs in the tumor. This information can be used to optimize the therapeutic strategy and improve the treatment outcomes for patients with cancer.

Collectively, the three studies discussed in this thesis highlight the emerging bio-imaging modalities and the versatility and effectiveness of biomimetic nanoplatforms in liver cancer and glioblastoma, providing new opportunities for early cancer diagnosis and therapy.

PUBLICATIONS ARISING FROM THE THESIS

Peer-reviewed Journal Publications

(*equal contribution)

1. **X. Huang**, H.Hui, W. Shang, P. Gao, Y. Zhou, W. Pang, CM. Woo, J. Tian, P. Lai, Deep Penetrating and Sensitive Targeted Magnetic Particle Imaging and Photothermal Therapy of Early-Stage Glioblastoma Based on a Biomimetic Nanoplatform. Advanced Science, 2023, 2300854

2. P. Gao, H. Hui, C. Guo, Y. Liu, Y. Su, **X. Huang**, K. Guo, W. Shang, J. Jiang, J[#]. Tian[#]. Renal clearing carbon dots-based near-infrared fluorescent super-small nanoprobe for renal imaging. Carbon, 2023, 201805-814

3. Y. Zhou*, **X. Huang***, J. Li, T. Zhu, W. Pang, L. Chow, L. Nie, L. Sun, P. Lai[#]. Small Animal In Situ Drug Delivery Effects via Transdermal Microneedles Array versus Intravenous Injection: A Pilot Observation Based on Photoacoustic Tomography. Pharmaceutics, 2022, 14(12): 2689

4. Z. Yu, H. Li, T. Zhong, J.H. Park, S. Cheng, C.M. Woo, Q. Zhao, J. Yao, Y. Zhou, **X. Huang**, W. Pang, H. Yoon, Y. Shen, H. Liu, Y. Zheng, Y. Park, L.V. Wang, P. Lai[#]. Wavefront shaping: A versatile tool to conquer multiple scattering in multidisciplinary fields. The Innovation, 2022, 3(5): 623-637

5. Y. Zhou*, C. Liu*, **X. Huang***, X. Qian, L. Wang[#], P. Lai[#], Low-consumption photoacoustic method to measure liquid viscosity. Biomedical Optics Express, 2021, 12(11): 7139-7148

6. **X. Huang***, Y. Zhou*, CM. Woo, Y. Pan, L. Nie, P. Lai[#], Multifunctional layered black phosphorene-based nanoplatform for disease diagnosis and treatment: a review. Frontiers of Optoelectronics, 2020, 13(4), 327-351

7. Z. Yingying, F. Cao, H. Li, **X. Huang**, D. Wei, L. Wang[#], P. Lai[#], Photoacoustic imaging of microenvironment changes in facial cupping therapy. Biomedical Optics Express, 2020, 11(5), 2394-2401

8. **X. Huang***, W. Shang*, H. Deng, Y. Zhou, F. Cao, C. Fang, P. Lai[#], J. Tian[#], Clothing spiny nanoprobes against the mononuclear phagocyte system clearance in vivo: Photoacoustic diagnosis and photothermal treatment of early stage liver cancer with erythrocyte membrane-camouflaged gold nanostars. Applied Materials Today, 2020, 18, 100484

Conference Presentation

1. **X. Huang**, H.Hui, P. Lai, J. Tian. (2023). A biomimetic superparamagnetism nanoparticle assisted MPI for early glioblastoma diagnosis in deep brain. International Workshop on Magnetic Particle Imaging, Aachen, Germany (Poster)

2. **X. Huang**, H.Hui, P. Lai, J. Tian. (2023). Targeted magnetic particle imaging and photothermal therapy of brain glioma based on biomimetic nanoplatform. China Biomedical Engineering Conference and Innovative Medical Summit, Suzhou, China (Poster)

3. P. Lai, **X. Huang**, Y. Zhou, Nanoparticle-enhanced photoacoustic diagnosis and photothermal treatment of small-animal early-stage liver cancer. The Journal of the Acoustical Society of America, 2020 (Oral)

4. **X. Huang**, P. Lai. Red blood cell membranes-camouflaged gold nanostars for enhanced photoacoustic diagnosis and photothermal treatment of liver cancer SPIE Photonics West 2020, San Francisco, USA, 2020 (Oral)

5. **X. Huang**, P. Lai, Red Blood Cell Membranes Camouflaged Gold Nanostars for Enhanced Photoacoustic Imaging and Tumor Photothermal Therapy in Mice. IEEE photonics society HK section postgraduate conference, Hong Kong, China, 2019 (Oral)

6. **X. Huang**, W. Shang, P. Lai. Enhanced in situ Liver Cancer Photoacoustic Imaging and Photothermal Therapy in Mice with Red Blood Cell Membranes Camouflaged Gold Nanostars. IEEE International Conference on Nanotechnology，2019, Macau SAR, China (Oral)

7. **X. Huang**, W. Shang P. Lai. Erythrocyte Membrane Camouflaged Carbon Nanotubes for Enhanced Photoacoustic Imaging and Tumor Photothermal Therapy. World Molecular Imaging Congress, 2018 (Poster)

ACKNOWLEDGEMENTS

My PhD study has been a long journey, along which I have learned a lot and met many important people in my life. Therefore, I would like to express my most sincere and deep gratitude to them in this thesis.

First of all, I would like to give my sincere gratitude to my supervisor, Prof. Puxiang Lai, for his generous and patient help and support. He gives me lots of confidence from the beginning to the whole study period. His positive and optimistic attitude has influenced me, enabling me to face difficulties positively instead of being depressed. His innovation and bold ideas in scientific research have inspired my enthusiasm for scientific research, and he also encourages and supports me to have my own ideas.

I also want to express my gratitude to Prof. Jie Tian of the Institute of Automation, Chinese Academy of Sciences, who provide me with the opportunity to be a visiting scholar in his lab. In his team, I met many doctors and researchers in the field of clinical medicine, engineering, and artificial intelligence, which enriched my knowledge in interdisciplinary fields and helped me to be more innovative in my own research. Here, I encountered mentors of my scientific path, Dr. Wenting Shang, who provided research guidance at the start of my research projects, and Dr. Hui Hui, who broadened my research field from PAI to MPI. I would also like to thank my best friends, Dr. Han Deng and Dr. Yingying Zhou, who are honest and enthusiastic and have helped me a lot in my scientific research and life.

I am more than appreciated to my parents, who have always supported me. Since I was a child, they placed a high value on education and gave me a conducive learning atmosphere. They gave me comfortable living arrangements, and helped me develop an optimistic and positive attitude, which is a very important part of my doctoral career. They have invested a lot on me and become my strong backing, so that I can devote

myself to scientific research without any concerns. I am also thankful to Mr. Chengsi Fu, who stood by me when I was feeling down, gave me comfort and moral support, and accompanied me along my academic journey.

Finally, I would like to thank all the team members, including Dr. Lizhi Shao, Dr. Huanhao Li, Dr. Tianting Zhong, Dr. Fei Cao, Dr. Zhipeng Yu, Mr. Shengfu Cheng, Miss Chiman Woo, Mr. Qi Zhao, Miss Yu Liu, Miss Pengli Gao, Mr. Kun Su, *etc*. They have helped me a lot in my work, and brought friendship and happiness to my life.

TABLE OF CONTENS

TABLE OF FIGURE

LIST OF ABBREVIATIONS

acoustic resolution	AR
bioluminescence imaging	BLI
blood-brain barrier	BBB
computed tomography	CT
computed tomography	CT
deoxyhemoglobin	Hb
diffuse optical tomography	DOT
enhanced permeability and retention	EPR
ethylenediaminetetraacetic acid	EDTA
field-free point/line	FFP/FFL
fluorescence protein tomography	FPT
fluorescence reflectance imaging	FRI
fluorescence-mediated tomography	FMT
Food and Drug Administration	FDA
glioblastoma multiforme	GBM
gold nanoparticle	AuNP
gold nanostars	AuNSs
high-resolution fluorescence reflectance imaging	HR-FRI
Hyaluronic acid	HA
indocyanine green	ICG
localized surface plasmon resonance	LSPR
lymphotropic nanoparticle-enhanced MRI	LN-MRI
magnetic nanoparticles	MNPs
magnetic particle imaging	MPI
magnetic resonance imaging	MRI
mesenchymal stem cells	MSCs

Microneedles	MNs
mononuclear phagocyte system	MPS
multiphoton microscopy	MPM
multislice CT	MSCT
optical coherence tomography	OCT
optical frequency-domain imaging	OFDI
optical resolution	OR
oxyhemoglobin	HbO_2
paclitaxel	PTX
phosphate buffered saline	PBS
photoacoustic	PA
photoacoustic imaging	PAI
photoacoustic microscopy	PAM
photoacoustic tomography	PAT/PACT
positron emission tomography	PET
propidium iodide	PI
recombinant human tumor necrosis factor	rhTNF
region of interest	ROI
reticuloendothelial system	RES
superparamagnetic iron oxide	SPION
transendothelial electrical resistance	TEER
ultrasound	US
World Health Organization	WHO

Chapter 1 Introduction

1.1 Prevalence of cancer

1.1.1 Cancer and its early diagnosis

Cancer is the second leading cause of mortality worldwide, accounting for one in every six fatalities and taking the lives of almost 10 million people yearly [1]. If it can be diagnosed early and treated appropriately, cancer is mostly curable. The average 5-year survival rate for patients with cancer in its early stages is 91%, compared to 26% for advanced stage patients [2]. However, about 50% of cancer cases are detected at an advanced stage. Therefore, it is necessary to establish early, stable, and reliable cancer diagnosis methods to prolong the survival of cancer patients. Cancer typically arises from the disorganization of normal tissues, which first manifests as lesions. Different phases of cancer development afford various opportunities for early identification: the detection results rely on how much information future tests provided and how certain it is caused by the captioned condition; each development stage offers featured information and possibilities. Therefore, a better understanding of the changes that occur throughout each stage of cancer progression is critical to enhance the accuracy of cancer diagnosis (Figure 1) [3]. Numerous studies have identified characteristic molecules in the development of early cancer lesions, such as metabolites, circulating tumor genes, and microbes, which enable early cancer identification and therapy [1, 4, 5]. However, the concentration of these biomarkers is typically insufficient in the early stages of the process, necessitating exceptional specificity and detection sensitivity.

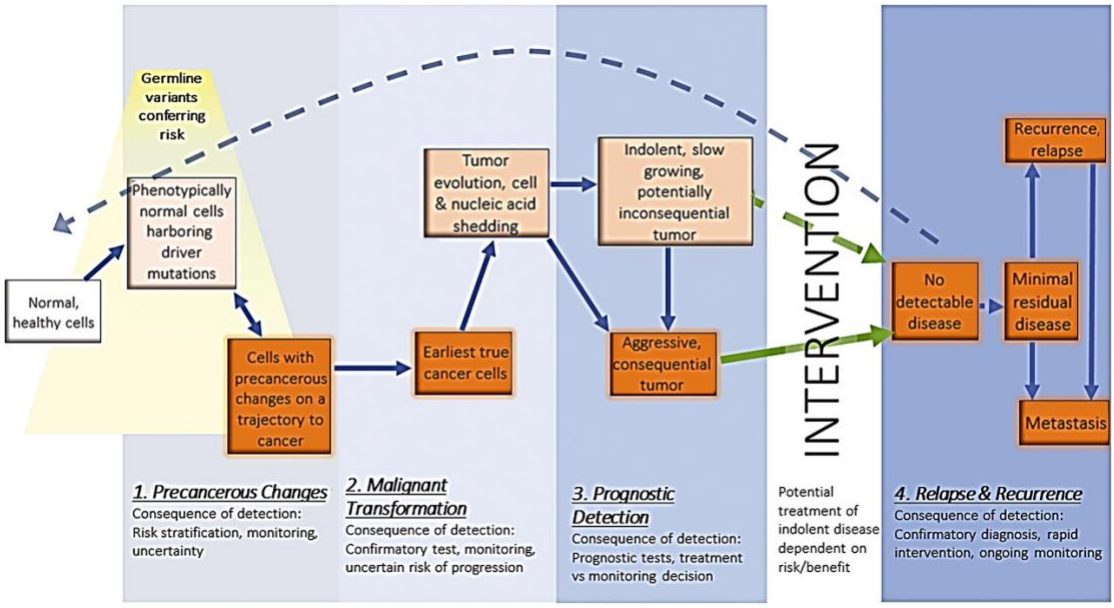

Figure 1. Detection and treatment of different stages of tumor. Image modified from Ref. [3].

1.1.2 Challenges in current cancer diagnosis

Research and development in early cancer detection have yielded significant health benefits. For example, colorectal cancer is more often detected at an early stage, which considerably prolongs patient survival [6]. That said, many malignancies, including pancreatic cancer, liver cancer, and glioma, are still mostly identified at advanced stages when the prognosis is already dismal. One of the obstacles in cancer diagnosis is that the tumor grows too quickly before it can be perceived. The tumor develops from a single tumor cell to newly emerging solid tumors, and the tumor microenvironment is gradually formed to promote angiogenesis and provide the nutrients required for tumor growth to enter the rapid growth period. Even if there were anti-tumor immunosuppression, the treatment would become less effective. The newly emerging solid tumors are immunogenic, sensitive to treatment, and unlikely to metastasize, which is considered at the early detection stage [8]. However, the tumor at this phase is usually one millimeter or less in diameter (approximately 10^5-10^6 cells), and most imaging techniques in clinical use nowadays, such as: magnetic resonance imaging (MRI), computed tomography (CT), and positron emission tomography (PET), are

unable to detect such small tumors. Thus, it is imperative to develop diagnostic methods that are sufficiently sensitive and specific to target and identify tumors in their early stages and hence reduce the possibilities of false positives.

1.2 Biomedical imaging for cancer diagnosis

1.2.1 Molecular imaging

Imaging methods, such as X-ray, MRI, CT, and nuclear medicine imaging, have been used for cancer diagnosis for decades. In recent years, molecular imaging, which allows for visualization of biochemical processes and targeting tracking at the cellular and subcellular structural levels, is rapidly emerging as a field with tremendous potentials to improve patient diagnosis and management [9]. Molecular imaging provides information that goes beyond the anatomical imaging model, enabling a more fundamental level of insight into pathophysiological processes [10, 11]. Based on their inherent ability to visualize the functional properties of malignant cells, molecular imaging techniques are promising to enhance cancer detection and staging, and tumor characterization at multiple levels [12]. These techniques, accompanied with ultrasound (US), PET, MRI, CT, *etc.*, have shown their contributions in clinical cancer diagnosis (Figure 2) [13]. For example, abnormal glucose metabolism in malignant cells occurs at early time points of carcinogenesis. PET imaging using 18 F-FDG allows to observe these changes, albeit with limited specificity and resolution. Besides, optical imaging is also applied in some superficial diseases, such as skin and ocular cancer, on account of their superior sensitivity and contrast, with limited penetration depth though. US offers the benefits of no ionizing radiation, moderate spatial resolution and sensitivity, and real-time capability, but whole-body imaging is unachievable. And its contrast agents are so far limited to the vascular systems. Without ionizing radiation, MRI provides the advantage of infinite penetration depth and great soft tissue contrast. However, it is costly, its acquisition time is long, and its sensitivity for detecting molecular contrast agents is relatively weak. CT is capable of producing anatomical

images with high spatial resolution and a fast acquisition time, and PET provides quantitative molecular imaging. But they both involve radiation exposure. Therefore, many of the aforementioned imaging modalities are combined (*e.g.*, PET-CT) to maximize the benefits of each imaging modality, and new imaging techniques continue to be developed.

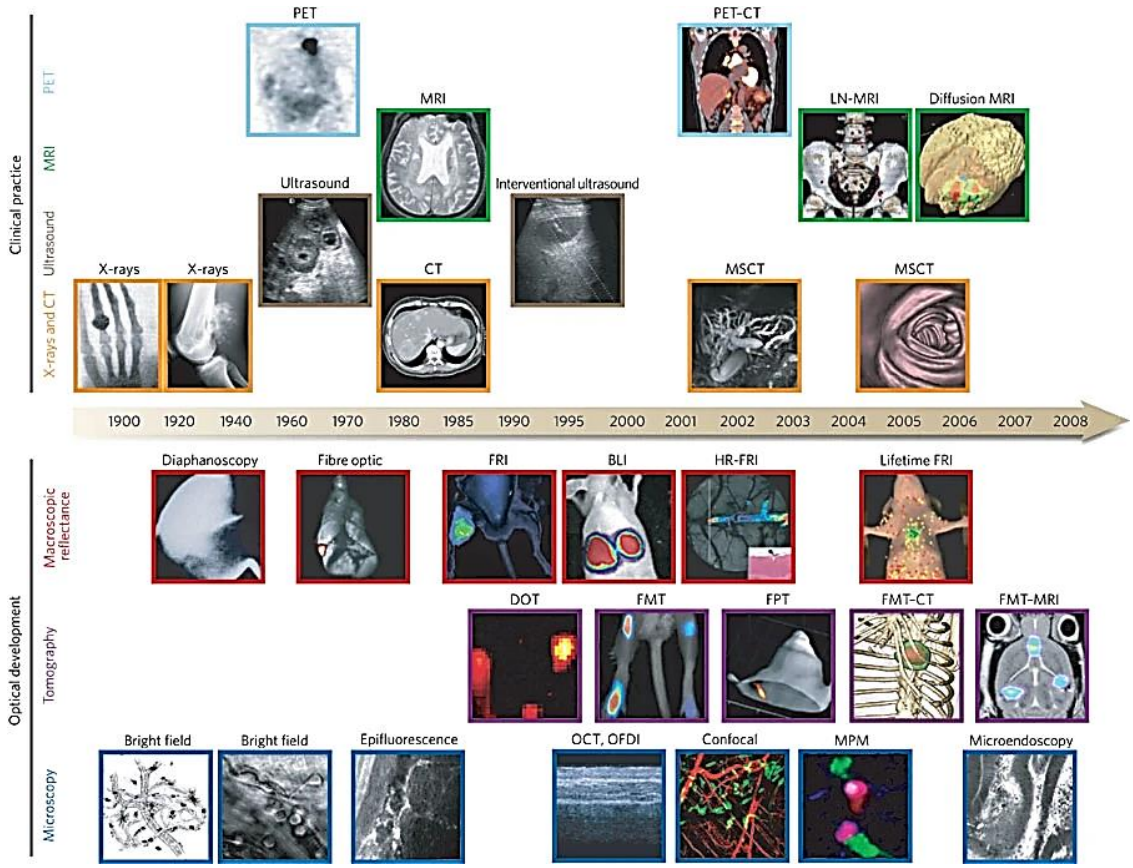

Figure 2. Some examples of bioimaging with timeline. Above: there are figures of bones, soft tissues, three-dimensional organs, and physiological imaging obtained through various methods like X-rays, ultrasound, MRI, and CT scans. Below: the figures show surface-weighted, whole-mouse, two-dimensional techniques, tomographic three-dimensional techniques, and intravital microscopy techniques. The timeline presented is approximate and not drawn to scale. Abbreviations are indicated in the *List of Abbreviations*. Image modified from Ref. [13].

1.2.2 Photoacoustic imaging

Photoacoustic imaging (PAI) is a relatively new technology that emerged in the field around the year 2000 and it has attracted wide attention. PAI is a noninvasive and non-ionizing imaging technology that combines the elevated contrast of optical imaging with the deep penetration of the US [14-17]. The principle is depicted in Figure 3: After being irradiated by a pulsed laser beam of specific wavelength, the excited molecules often convert a portion or all of the absorbed optical energy into heat through nonradiative relaxation, raising the local temperature and producing thermal expansion. The vibrations are eventually transmitted in the form of ultrasonic waves to a transducer placed around the tissue [18]. The ultrasonic transducer converts the detected acoustic signal into an electrical signal, and the image information corresponding to the optical absorption information of the biological tissue can be obtained after signal processing procedures such as forward amplification, filtering, and beamforming. By converting the specific absorption of light by biological tissue into weakly scattered ultrasound within the tissue, PAI allows for the acquisition of optical information with ultrasonic spatial resolution (even sub-ultrasonic spatial resolution if the light spot focused on the target is smaller than the sensitive area of the acoustic transducer). The photoacoustic signal generation does not distinguish the excitation light from the convergence, plane, or scattered light. Therefore, PAI technology features high contrast and breaks the imaging depth defect of traditional optical techniques.

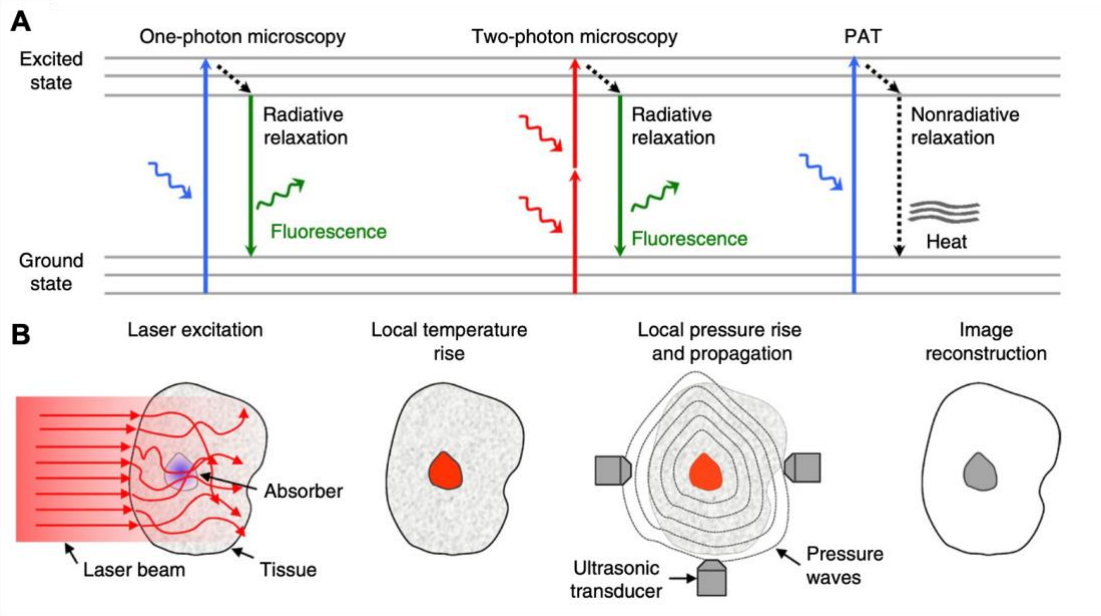

Figure 3. The principle of PAI: After laser irradiation, excited molecules transform optical energy into heat and lead to thermal expansion, which is detected by the transducer through the ultrasonic waves.

Depending on the system design and application, PAI has evolved into various implementations, the most common of which are photoacoustic tomography (PAT/PACT) and photoacoustic microscopy (PAM) [19, 20]. PAM relies on the mechanical focus scanning of the optical focusing and the single array ultrasonic transducer, whereas PACT depends on the mechanical/electronic scanning of the multi-array ultrasonic transducer and the reconstruction method. PAM exhibits higher resolution yet shallower penetration depth, can locally image tiny tissue structures (micron-scale resolution), and can visualize metabolic activities and molecular functions at superficial penetration (submillimeter imaging depth) due to the scattering of incident light. These capabilities make PAM attractive for a range of structural, functional, and molecular microscopic applications. Depending on whether optical focus remains at the region of interest (ROI), PAM can be further classified into two types: optical resolution (OR)-PAM and acoustic resolution (AR)-PAM [21-23]. In contrast, PACT can detect tissue structure and function at the macro level (millimeter

to centimeter imaging depth) with ultrasonic resolution (sub-millimeter to millimeter), which is widely employed in animal and clinical applications with a wider and deeper field of view at moderate US resolution [24-26]. Figure 4 displays the multiscale PAI representatives of organelles, cells, tissues, and organs *in vivo*. Therefore, PAI technology can be used in a wide range of micro and macro applications.

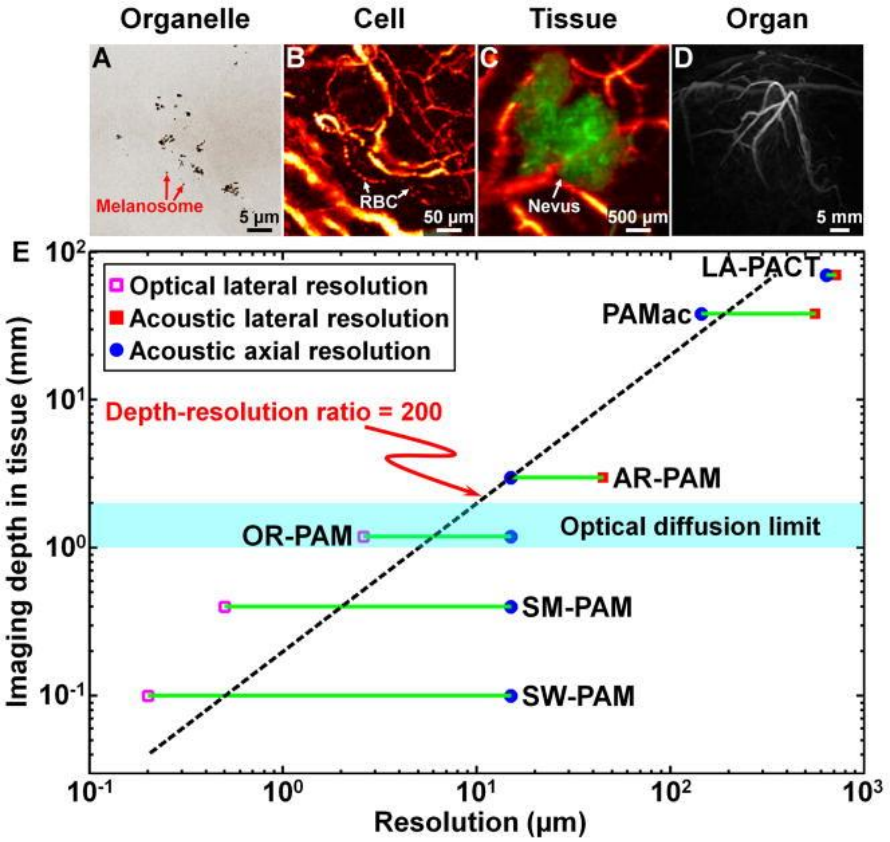

Figure 4. Multiscale PAI of various biological entities *in vivo*, from organelles to cells, tissues, and organs. (A) Subwavelength PAM imaging of melanosomes in the ear of a black mouse. (B) OR-PAM imaging of individual red blood cells in a mouse ear capillary. (C) AR-PAM imaging of a nevus on a human forearm. (D) PACT imaging of a human breast. (E) Tissue penetration depth versus spatial resolution in PAT. Abbreviations: SM, submicrometer; LA, linear array. Image modified from Ref. [27].

PAI distinguishes signals from different tissues according to their featured optical absorption, which has been used in lots of medical applications, such as 1) real-time PAM imaging as a supplement to the optical microscope-based method used in eyes'

choroidal neovascularization [28]; 2) real-time PAM imaging of melanoma [29]; 3) microangiography in cancer and neuroscience to provide information on vascular morphology, oxygen metabolism, blood flow, and blood oxygenation [30-32]; 4) 360-degree field of view PA endoscopy to detect gastrointestinal cancer with higher sensitivity and faster speed [33, 34]; 5) PA visualization and monitoring of inflammatory systemic skin diseases, like psoriasis and eczema [35, 36]; 6) different types of adipose PAI to help explore the fundamentals of adipose tissue metabolism and even the role of adipose tissue in controlling obesity and diabetes [37]; 7) PAI-guided molecular level cancer detection [38, 39]; 8) high-resolution PAT as an adjunct to the conventional method of reporter genes imaging for the study of biological processes [40]; 9) sentinel lymph node mapping and needle guidance with clinical handheld PAI system [41]; and 10) breast cancer detection with enhanced contrast by the clinical system. A Food and Drug Administration (FDA)-approved handheld PAI system (Imagio) is illustrated in Figure 5 [42]. Numerous instances have shown that PAI is promising for use in biomedical applications at both micro and macro scales.

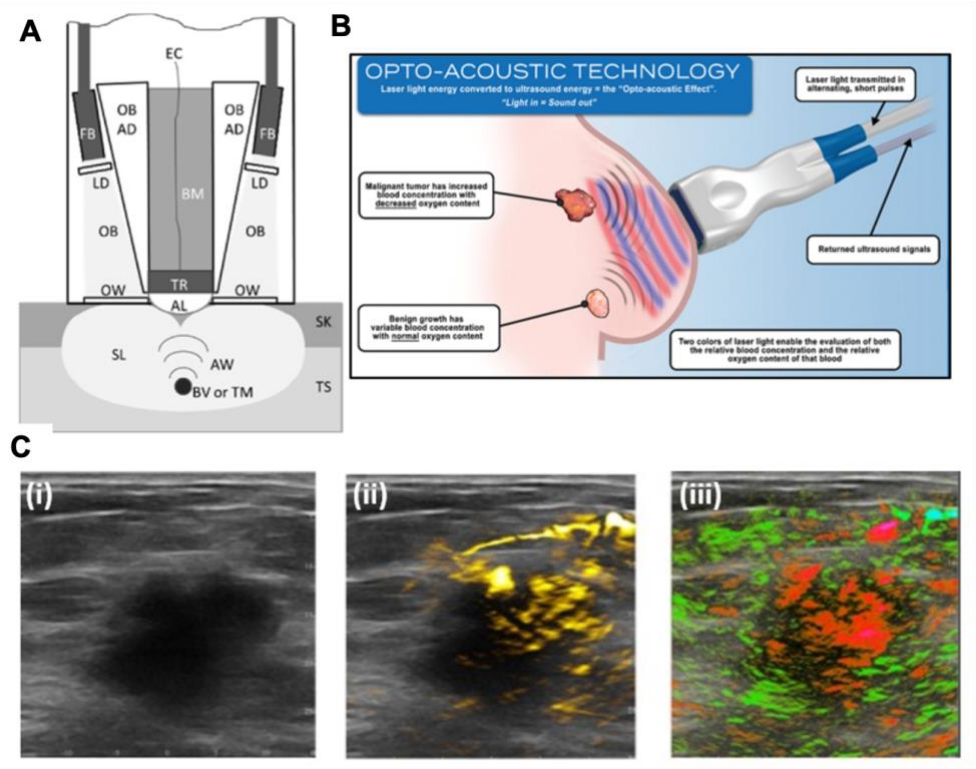

Figure 5. (A) Scheme of the Imagio system. Abbreviations: TS, Tissue TS; SK, skin; SL, scattered light; OB, optical beams; FB, fiber bundles; LD, light diffusers; OW, optical windows; AW, acoustic waves; BV/TM, blood vessels/tumors; AL, acoustic lens; TR, transducers; EC, electrical cables; BM, backing material. (B) Laser radiation at wavelengths corresponding to oxygenated and deoxygenated hemoglobin absorption peaks generate sonic signals, which could be utilized to rebuild the distribution maps of oxygen saturation. (C) An example of combined US/PA images of breast cancer—i) the US grayscale image of a 2.6-cm-diameter tumor, ii) regions of increased hemoglobin, and iii) the oxygenation map. Images modified from Ref. [42].

1.2.3 Magnetic particle imaging

As another new imaging modality, magnetic particle imaging (MPI) has also gained lots of attention since its introduction in 2005, owing to its extremely high sensitivity and unlimited penetration [43, 44]. Unlike US, CT, MRI, and PA, MPI is unable to produce structural images. Instead, it is a tracking visualized modality, similar to PET. MPI signals are generated directly from the magnetic moment of magnetic nanoparticles (MNPs) in the presence of magnetic fields [45]. The imaging principle of MPI is illustrated in Figure 6 [44]. An applied magnetic field can induce a change in magnetization's strength or direction, leading to a dynamic process of magnetic moments of MNPs. Based on Langevin's theory, the magnetization of particles can rapidly reach saturation and then plateau as the magnetic field is applied. The applied magnetic field in MPI consists of two fields that are crucial: the selective field and the driving field. The selective field characterized by a strong magnetic gradient is utilized for spatial encoding over a zero-field region at the field-free point/line (FFP/FFL), where the remaining MNPs other than the FFP/FFL are saturated. In order to generate the signal, the magnetization response of the particles changes nonlinearly as the FFP/FFL passes through the particles' site. The variation in magnetization resulting from the selective field generates a voltage in the receiver coil, which corresponds to

the position of the FFP/FFL at any given moment and produces an MPI image. The voltage induced is directly proportional to the number of particles located at the FFP/FFL position, allowing for accurate particle quantification. The driving field has no effect on MNPs in the saturation state. Only MNPs at the FFP/FFL exhibit a magnetization response to the driving field, hence producing MPI signals [44, 46]. In summary, the MPI signal is generated by the nonlinear magnetization response of particles to applied magnetic fields. The magnetization detected by MPI is 22 million times stronger than that seen in MRI which with a magnetic flux density of 7 T [47]. Thus, MPI with MNPs produces an image with a superior contrast and an extremely high SNR ratio.

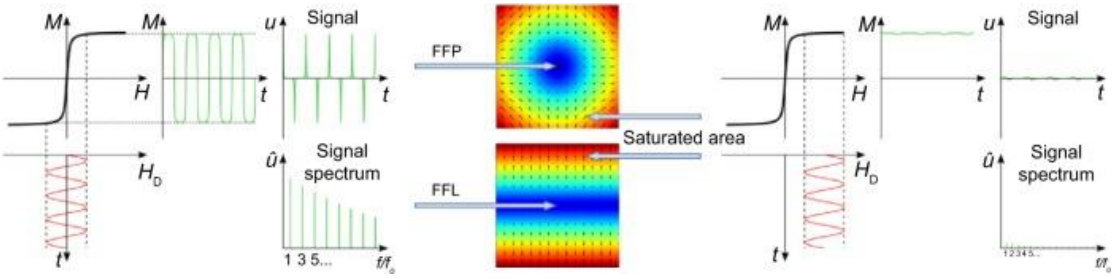

Figure 6. Basic principle of signal generation in MPI. Left: the response of MNPs located at the FFP/FFL, which is composed of the excitation frequency (f) as well as its higher harmonics. Middle: the graphical representation of an FFP and an FFL, with only the MNPs inside and close to non-saturated regions reacting to the excitation field. Right: MNPs outside the FFP/FFL are saturated without response to the excitation field. Abbreviations: H, magnetic field strength; H_D, the magnetic field strength of the driving field; M, the magnetization of MNPs; u, voltage; t, time; f/f_0, higher harmonics of excitation frequency; û, Fourier transform of the voltage signal. Image modified from Ref. [44].

The MPI theory reveals that the MPI signal is linearly proportional to the number of particles in the momentary FFP/FFL region, which allows us to determine the magnetic quantity based on the signal density. As the MPI signal is generated solely from the

MNP, excellent contrast and SNR can be achieved without background noise [48]. Specifically, MPI can only detect the injected particles and is unaffected by endogenous iron in the body, similar to PET. However, it usually takes a few minutes for PET to produce images due to the limitations of the reconstruction algorithm, making them inappropriate for dynamic imaging applications. PET tracers are radioactive, and their half-life periods range from a few minutes to a few hours, whereas MPI tracers are non-radioactive and can last from days to weeks [49]. MPI's spatial resolution and sensitivity are affected by the magnetic gradient intensity and the properties of the MNPs. In current research, MPI can achieve sub-millimeter spatial resolution and nanomolar sensitivity [46, 50].

The enhanced SNR ratio of MPI and the long half-life of MPI particles allow for more comprehensive approaches, including perfusion imaging and cell tracking [51, 52]. This advantage is superior to conventional structural imaging techniques such as MR and CT, which encounter challenges to obtain reliable perfusion images [53, 54]. MPI perfusion imaging can assess various pathophysiology related to vascular changes, such as blood-brain barrier permeability, stroke diagnosis, and tumor grading. One representative example is the MPI pulmonary perfusion for pulmonary embolism diagnosis [54]. The most significant advantage of MPI is that it can track cells, which offers non-radioactive long-term tracking, which has great potential for cell therapy monitoring and evaluation [55, 56]. The extremely high sensitivity affords MPI a detection limit of as few as 200 cells [57]. Wang *et al.* plotted the trajectory of magnetic nanoparticle-labeled mesenchymal stem cells (MSCs) after injected into the mouse according to the MPI/CT images (Figure 7) [55]. In addition, MPI has demonstrated its flexibility in lipoprotein metabolism [58], cancer diagnosis and disease progression prediction [59, 60], cardiovascular functional disordered diagnosis [61, 62], neuroimaging including traumatic brain injury [63], ischemic stroke [53], neural progenitor cell implantation [57], and glioma imaging [64].

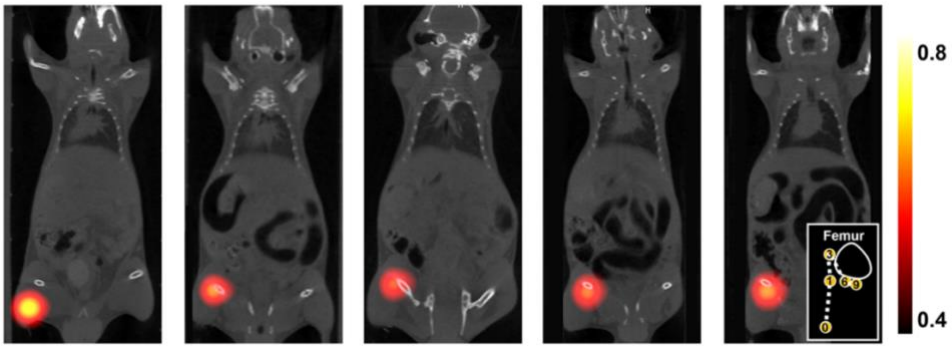

Figure 7. MPI/CT images after injection of magnetic particle-labeled MSCs in a hindlimb ischemic mouse. The inset is the illustrative trajectory of transplanted stem cells. Images modified from Ref. [55].

1.2.4 Contrast agents for bioimaging

Although endogenous imaging contrast agents can be exploited or induced within tissues, such as blood for photoacoustic imaging, many molecular imaging scenarios require the use of exogenous agents that target the tumor microenvironment to discover biological pathways. The practical application of molecular imaging to detect small malignant lesions through whole-body scans of high-risk patients depends on the availability of more specific contrast agents. These contrast agents should ideally target pathological features using a radiation-free imaging modality to ensure patient safety [12]. Nanoparticles (NPs), typically 1 to 100 nm in size, are currently the most commonly used contrast agents for molecular imaging. They have remarkable bio-reactivity, tunable surface characteristics, opto-electromagnetic capabilities, as well as strong chemical, physical, and biological flexibility [65]. NPs benefit functional imaging by diagnosing and defining disease, monitoring the efficacy of treatments, enhancing imaging effect, or enabling imaging of cellular and molecular events. In general, these NPs often have to adhere to the following standards: 1) excellent biocompatibility, which allows the implant to maintain its function and not cause clotting or thrombosis once it enters the body; 2) non-toxicity, which means it would not affect healthy organs; 3) high contrast, which can increase the SNR of the imaging;

4) the capacity to get through circulatory and cellular obstacles in order to efficiently reach the desired locations.

Specific requirements should apply to different imaging modalities. For PA, the contrast agents typically require a high molar extinction coefficient, good photostability, as well as a sharply peaked and distinct absorption spectrum that is in the near-infrared (NIR) region but avoids the intrinsic chromophores (*e.g.*, oxy/deoxy-hemoglobin) absorption peaks so that they can be extracted from the background (tissue) signal [66, 67]. With improved SNR and deeper penetration from NIR excitation light, these characteristics can benefit PAI by allowing more precise detection. Examples of PA contrast agents that conform to these particular requirements will be covered in the next chapter.

In contrast to PA, the feasibility and quality of MPI imaging depends primarily on the contrast agents, also known as MPI tracers. Three essential characteristics of these MNPs provide the foundation of MPI. First, the NPs are superparamagnetic, which means that the magnetization of the particles is lost as soon as the applied magnetic field is removed. Second, MNPs can be magnetically saturated, and third, their magnetization curves are nonlinear without hysteresis [68]. According to Langevin's theory, MNP maintains thermal equilibrium and experiences a net magnetization of zero when there are no extrinsic influences. The magnetization of MNP rises dramatically in response to increasing magnetic fields and reaches a plateau upon saturation. These intrinsic properties of MNP constitute the fundamental principle for the differentiation and detection and therefore play a critical role in MPI [69]. In addition to system parameters, the MPI sensitivity also depends on the magnetic moment of the MNPs, which can be raised by increasing the core diameter of particles, as the signal strength increases in proportion to the third magnitude of the core diameter. Along with the strength of the gradient selection field, the magnetization curve of the

particles plays a major role in determining the spatial resolution; steeper slope of the MNPs ' magnetization curve allows for less spatial confinement of their signals, which improves the image quality [70].

So far, clinically used NPs are mostly limited to sulfur colloid, gold, silica, and iron oxide [71]. Special features are given to these functional NPs for particular applications. However, they all face obstacles to meet the aforementioned standards. Generally, the enormous surface area of these particles allows for the attachment of numerous targeting agents, which increases the target-binding probability. However, due to their increased size, NPs often accumulate in the reticuloendothelial systems (RES, also called the mononuclear phagocyte systems (MPS), a group of organs containing phagocytic cells) for a long time after injected into the bloodstream (Figure 8), resulting in reduced effect and poor biocompatibility [72]. This is the major impediment for NPs towards clinical utilization [73, 74]. Additionally, NPs with good dispersion and stability are urgently required. Although PEGylation can somewhat improve the stability and biocompatibility of the NPs, they remain controversial due to their significantly increased size, immunogenicity, reduced intracellular uptake, and non-degradable nature [75]. Therefore, more ingenious functionalization techniques for NPs are crucial prior to clinical use.

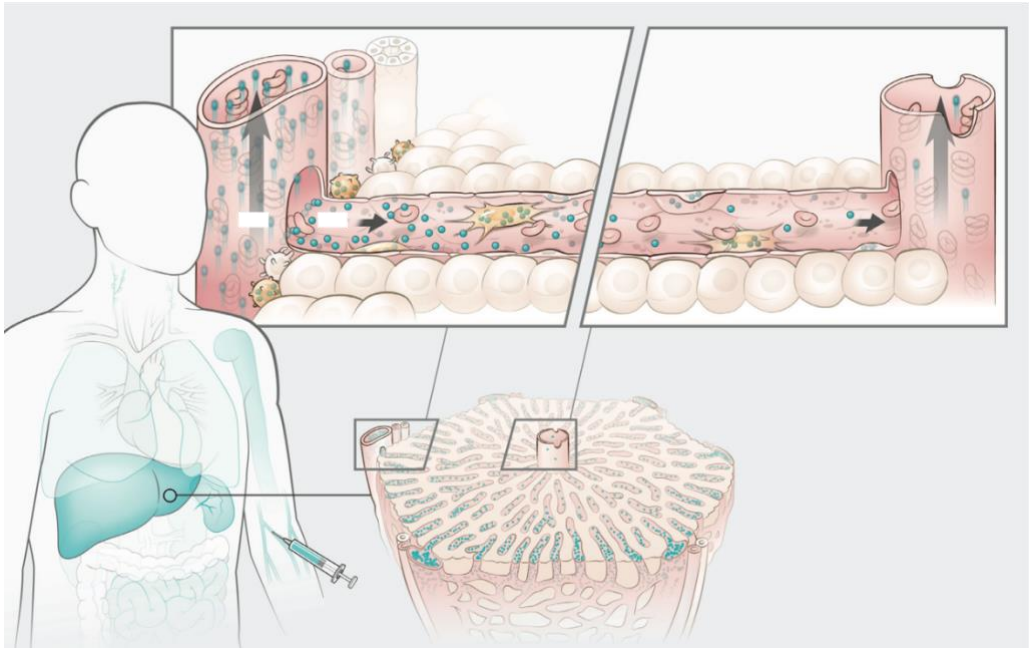

Figure 8. Transport mechanism of nanomaterials in liver. The degree of nanomaterial uptake within each MPS organ is represented by the intensity of the blue color. Nanomaterials circulate rapidly from the periphery to reach the liver, where their speed is greatly reduced to promote interactions with various cells, resulting in their gradual removal from the blood. Image modified from Ref. [76].

1.3 Cell membrane-coated biomimetic nanoparticles

1.3.1 Basic concept

Biomimetic NPs combine the properties of biomaterials and synthesized components to enable effective navigation and connection in complicated biological systems [77]. Cell membrane-coated NP is a bionic platform for transporting imaging NP and therapeutic medication, which combines the capacity of the cell membrane with the properties of the core nanostructures [78]. Phospholipids are semi-permeable structure, which are the major components of cell membranes containing both hydrophilic and hydrophobic regions, as well as embedded and bound characteristic proteins and glycans that represent their certain functions (Figure 9) [79]. Cell membrane camouflaged strategy has greatly improved the NPs' biocompatibility and immunogenicity so that the cell membrane coated NPs have lower possibilities to be

captured by the RES and are more likely to take their own responsibilities [80]. Moreover, the membranes of various origins give them a unique identity that may open up new opportunities in certain situations [81]. Inspiration of biomimetic membrane materials motivated by natural components, including innate host cellular components and invasive pathogens, and mainly developed from: 1) red blood cells which could help prolong the circulation in the body [82]; 2) leukocytes, which have great selectivity in specific diseases and in regulating the inflammatory response [83]; 3) macrophages, which have innate inflammatory directed chemotaxis [84]; 4) platelets, which have an excellent capacity in treating hemorrhage, hemostasis and targeted dug delivery[78]; 5) exosomes, which is an effective deliver platform [85]; 6) viruses, which have favorable properties in cell targeting and avoiding recognition by the immune system [86]; 7) bacteria, which are nature materials for great antibacterial vaccines [87]; and 8) cancer cells, which can homogenously target the tumor [88].

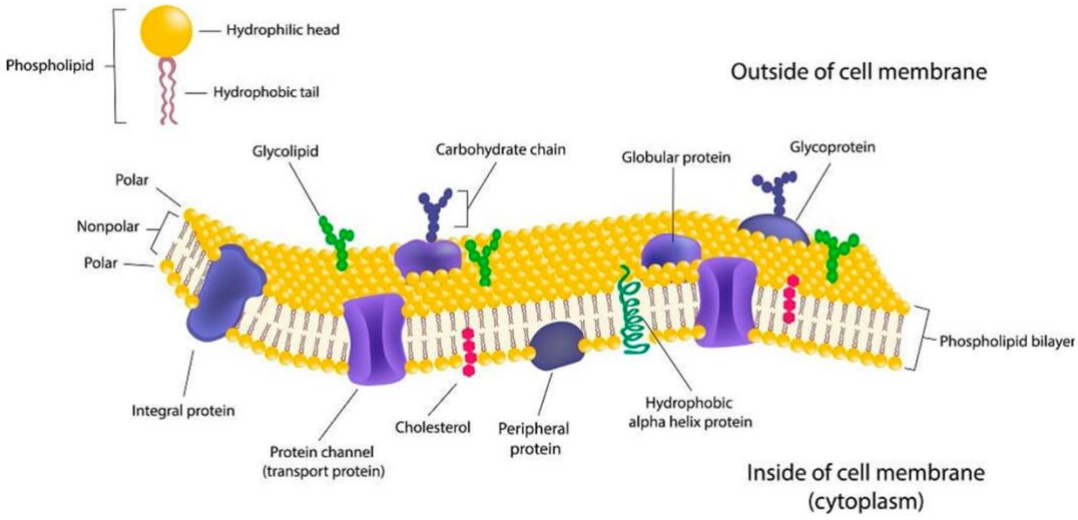

Figure 9. Illustrative structure and components of cell membranes. Image modified from Ref. [79].

1.3.2 Fabrication

Cell membrane-wrapped NPs usually consist of NPs that hold an effective contrast agent in the core and a thin membrane on the outside, creating a core-shell structure

(Figure 10) [89]. The fabrication of membrane camouflage NPs usually involves three processes: 1) First, extracting the cell membrane from the original cells. The separation of cell membranes mainly includes sequential steps of hypotonic lysis, mechanical fragmentation, and differential centrifugation to empty the cytoplasm. Typically, cell membrane vesicles for core NP coatings are collected by a combination of hypoosmotic lysis and freeze-thawing. Then, the separated cell membrane is mechanically broken by a homogenizer, ultrasound treatment, and/or extrusion. Finally, differential high-speed centrifugation is performed to obtain membrane vesicles. The resultant cell membrane vesicles are precipitated and suspended in sufficient phosphate buffer and cryopreserved for later use. 2) Design of the core NP, which includes the preparation of various contrast agents and nanomaterials. Two kinds of NPs used in specific scenes will be introduced respectively in the next two chapters. 3) Finally, the cell membrane and the core NPs are fused together to form a core-shell structure. Typically, an extruder is utilized to uniformly apply the membrane on the NP surface so that membrane vesicles and core NPs are co-extruded multiple times through polycarbonate porous membranes. Ultrasound preparation and microfluidic electroporation are the alternative techniques for the fusion [90]. Electroporation involves applying an enhanced external electric field pulse to reconstruct cell membranes, resulting in the formation of multiple holes in these membranes through which the NPs can disperse into the vesicles.

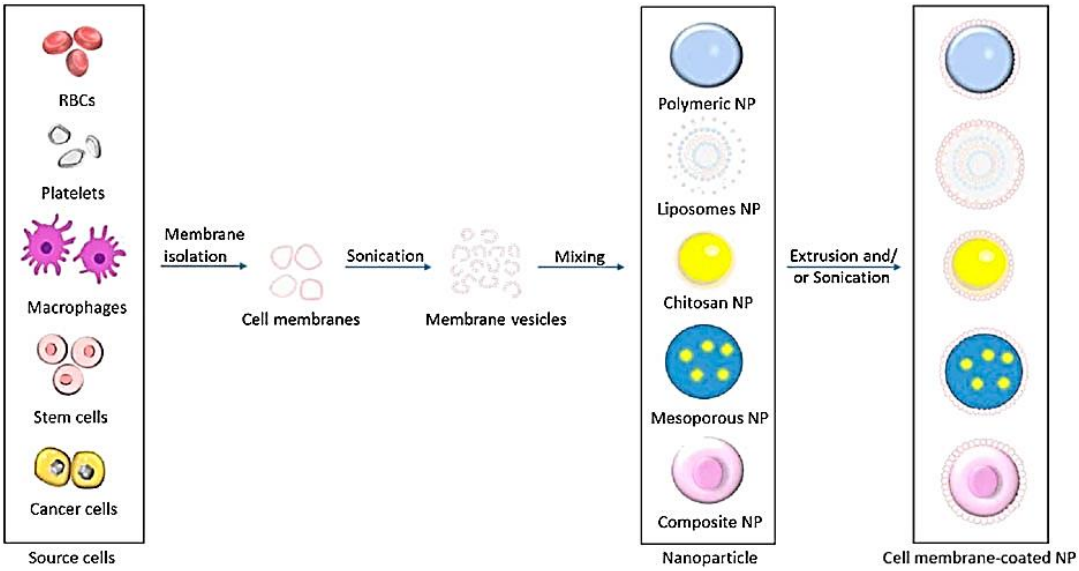

Figure 10. Scheme of fabrication of cell membranes isolating from kinds of source cells camouflaging various core NPs. Image modified from Ref. [89].

1.3.3 Representative biomedical applications

Due to the inherent properties of the cell membrane, there is limited loss of function in the preparation and delivery of cell-membrane coated contrast/therapeutic agents, such as the membrane binding antigens necessary for immune escape and targeting, which can protect the functions of kernel NPs [91]. Membrane-loaded NPs have been shown to be useful in tumor diagnosis, targeted chemotherapy, photothermal diagnosis and treatment, and immunotherapy. For example, the reconstruction of natural macrophage cell membranes with the associated membrane proteins into membrane vesicles does not lose the inflammatory tumor targeting ability. The macrophage membrane serves as a hidden cloak against opsonin and RES clearance during systemic circulation and as a tumor targeting navigator to promote tumor accumulation. The anti-cancer drug paclitaxel (PTX) is encapsulated in a PEG self-assembled structure with targeted peptides and then wrapped around a macrophage membrane to help reach the tumor site (Figure 11). The whole nanoparticle can sense the change of PH in the tumor microenvironment and release PTX layer by layer to achieve the effect of tumor inhibition [84]. Liu *et al*. used tumor cell membranes to develop glycan delivery systems that can differentiate different cancer subtypes and selectively image them [92].

In a multi-tumor mouse model inoculated with a HeLa tumor (left) and an MCF -7 tumor (right) of similar size, glycan NPs coated with HeLa cell membrane (GL@Hela) and MCF-7 cell membrane (GL@MCF) were injected, respectively (Figure 12). It can be seen from fluorescence imaging that the Hela tumor of mice injected with GL@Hela showed a large number of fluorescence signals. It was demonstrated that GL@Hela can actively identify and "homing" homologous Hela tumors. The same results were seen in another group of mice injected with GL@MCF. This study showed that the selective glycan labeling of homologous cancer cells was achieved through multi-receptor mediated targeting, which is 1.7 times more effective than the single ligand targeting strategy *in vitro*. In another study, RBC and platelet membranes were fused together as coating materials to create hybrid [RBC-P]NPs [93]. Physically, the resultant particles are similar to single membrane prepared NPs with a bilayer cover. At the protein and functional levels, the [RBC-P] NPs represent a crossover between the two original cell types, while preserving the RBC's prolonged circulation and platelets' effective targeting of metastatic cancers. Cell membranes exhibit different properties, such as controlling biological interactions, immune escape, and homologous targeting. These properties are maintained after coating on the NPs. Of course, the wide applications of these nano-carriers are yet to be explored.

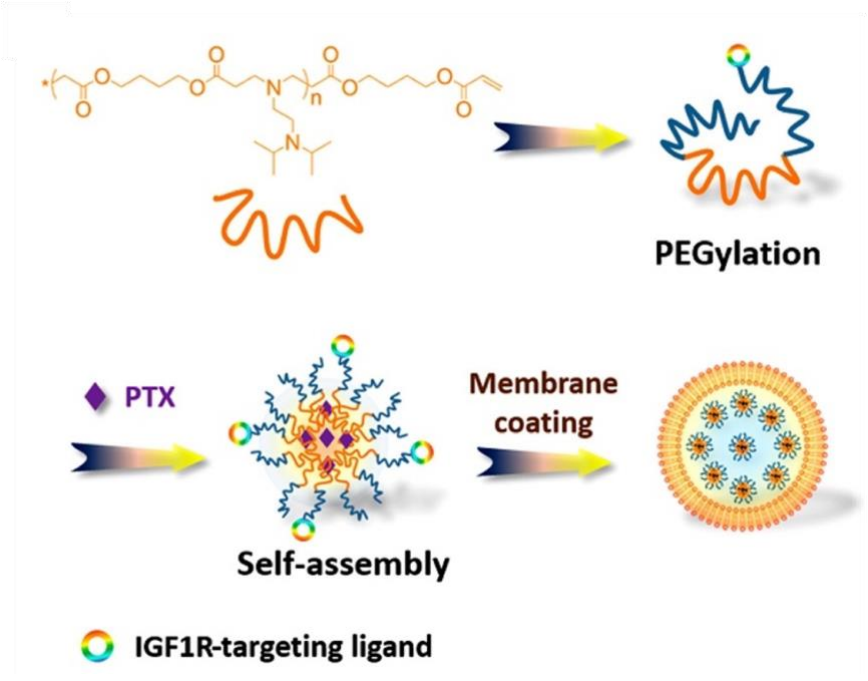

Figure 11. Scheme of the preparation of PH responding macrophage membrane-coated tumor inhibition. Image modified from Ref. [84].

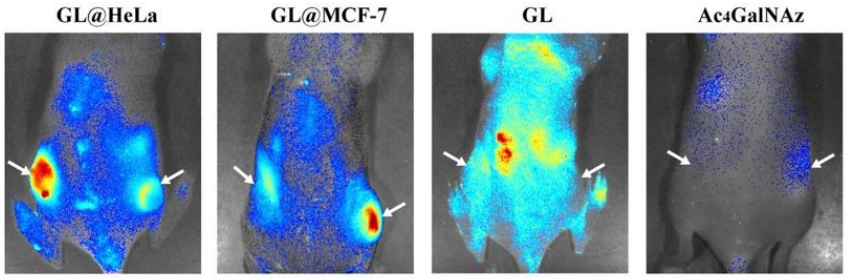

Figure 12. In vivo fluorescence visualization of mice with tumors administered with GL@HeLa, GL@MCF-7, GL, and Ac4GalNAz. Image modified from Ref. [92].

In this thesis, studies are carried around two kinds of cell membrane source: red blood cell and tumor cell. Details will be specified in the corresponding chapters.

1.4 Monitoring of drug delivery

Thanks to molecular imaging, which can help to detect the location and progression stage of tumors as early as possible, doctors can provide active intervention or personalized treatment to different patients. In the development of cancer therapies, the speed and efficiency of drug delivery to the tumor are major evaluation criteria. For almost all medications, it is important to probe issues such as poor solubility, high toxicity, high dose, poor solubility aggregation, non-specificity of delivery, bio-degradation, and short cycle half-life, *etc*. [94]. Image guidance can be used to evaluate the characteristic principles of drugs, including pharmacokinetics, biological distribution, active or passive tumor targeting ability, and ultimately precise drug release [95]. In addition, tumors are heterogeneous, and monitoring drug delivery during treatment can be used to select patients who respond to drug therapies and to track their pharmacokinetic behavior in a timely manner to rationally improve the treatment strategy [96]. Image-guided drug delivery is becoming an ideal or desired

strategy for real-time vehicle evaluation of drug design rationality, *in vivo* safety, and anticancer effect, especially for new drugs.

Figure 13 displays the imaging modes that have been developed for drug delivery monitoring and the processes involved. Although many imaging methods are used to track the delivery of nanomedicine, it is challenging to accurately capture the entire drug delivery process with any of the existing imaging methods in clinics [97]. More imaging effort should be made to target and accumulate in primary and metastatic tumors that are tiny and usually neglected. Therefore, it is important to develop more sensitive imaging modalities with high spatial resolution to track drug delivery.

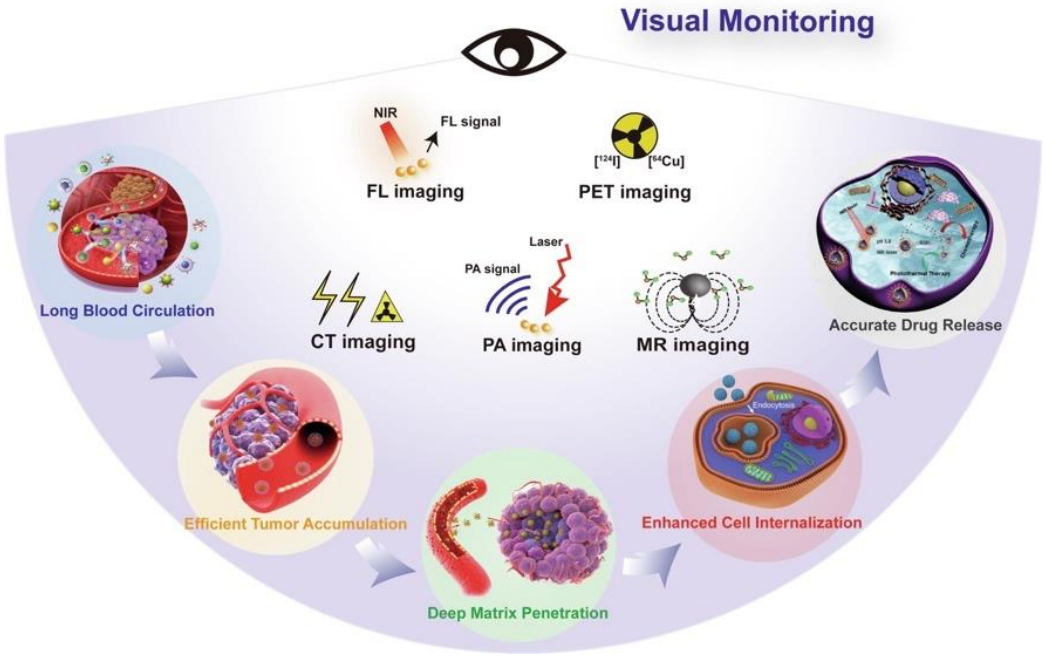

Figure 13. The scheme of imaging-guided nanomedicine delivery. Image modified from Ref. [95].

Chapter 2 Immune-escaped red blood cell membrane nanoplatform for photoacoustic imaging and photothermal therapy in liver cancer

This chapter is reproduced with some adaptations from the manuscript "X. Huang, W. Shang, H. Deng, Y. Zhou, F. Cao, C. Fang, P. Lai, J. Tian, Clothing spiny nanoprobes against the mononuclear phagocyte system clearance in vivo: Photoacoustic diagnosis and photothermal treatment of early stage liver cancer with erythrocyte membrane-camouflaged gold nanostars. Applied Materials Today, 2020, 18, 100484". The contributions of authors are as follows: X. Huang, W. Shang and J. Tian conceived the idea. X. Huang and H. Deng designed and ran the experiments. X. Huang, W. Shang and P. Lai prepared the manuscript. All authors were involved in the analysis and discussion of the results and manuscript revision.

This chapter is about a study showing how red blood cell membrane camouflaged photoacoustic NPs used for photoacoustic diagnosis and photothermal therapy (PTT) for liver cancer, with more details on methodology and experimental results.

2.1 Motivation of this study

2.1.1 PAI for liver cancer diagnosis

As introduced in Chapter 1, PAI is a noninvasive hybrid modality capable of revealing high optical contrast at ultrasonic resolution in relatively thick soft tissue, like liver, by converting nonionizing optical radiation into not-so-scattered ultrasonic waves [27, 98-100]. PAI has many advantages, such as safety, high resolution, high specificity, and relatively low cost compared with traditional imaging modalities such as CT and MRI. More importantly, many endogenous tissue chromophores (optical absorbers), such as oxy-/deoxy-hemoglobin, melanin, and water, can provide rich structural and functional information [101]. Therefore, this technology is intrinsically promising for precise detection of tissue heterogeneities, especially in cancer [102]. However, the photon flux,

and hence the PA signal strength attenuates very rapidly with penetration depth. Moreover, for deep organs, especially the liver, the background (normal tissue) poses strong optical absorption and scattering over the visible optical spectrum, severely impairing the diagnosis of liver cancer [103], the fourth leading cause of cancer-related death worldwide [104] In this scenario, exogenous agents with excellent NIR absorption are of great significance: the NIR light yields deeper penetration depth [105, 106].

2.1.2 Photoacoustic contrast agent

As introduced in Section 1.2.2, the essence of PAI is that the excited light is absorbed by endogenous chromophores or exogenous contrast agents to generate heat and produce thermal vibration, thus emitting ultrasonic waves with a wide frequency range. The commonly used light source for PAI is in the NIR window with a wavelength between 680 and 970 nanometers for deeper penetration. Thus, the absorption spectra in the NIR range become an important requirement for PA contrast agents. Photoacoustic contrast agent includes both organic and inorganic materials, such as metallic nanomaterials, transition-metal chalcogenides, carbon-based nanomaterials, small molecular dyes, and semiconducting polymer NPs [107]. Here, we focus on plasmonic noble metal NPs, which have seen extensive exploitation in PAI. Localized surface plasmon resonance (LSPR) is an optical phenomenon caused by the confinement of a light wave within conductive NPs smaller than the wavelength of light. Due to the LSPR effect, metallic nanomaterials exhibit outstanding light absorption and photothermal conversion capability, which shows the optical absorption a few orders of magnitude larger than that of traditional contrast agents such as dyes [108, 109]. Consequently, metallic NPs are utilized in both PAI and cancer treatment by converting plasmon resonance into heat due to their exceptional light absorption properties [110]. Gold nanoparticle (AuNP) is one such representative owing to its favorable and tunable absorption spectrum in the NIR region. AuNP can be synthesized into various shapes,

such as nanospheres, nanorods, nanostars, nanocages, and nanoprisms (Figure 14) [111]. By adjusting the size and shape, the absorption wavelength of AuNP can be controlled within the ideal range due to the change of resonance frequency. For example, as the branch of gold nanostars (AuNSs) becomes longer, their peak absorption shifts to longer wavelengths [112] (Figure 15). Moreover, AuNP has received FDA approval for clinical trials for cancer treatment. One of the clinical phase I trials is that the CYT-6091 (recombinant human tumor necrosis factor (rhTNF) bound colloidal gold) was investigated for solid tumor treatment [113].The rhTNF was bonded to gold NPs using a PEG linker that also served as a biocompatible antifouling layer.

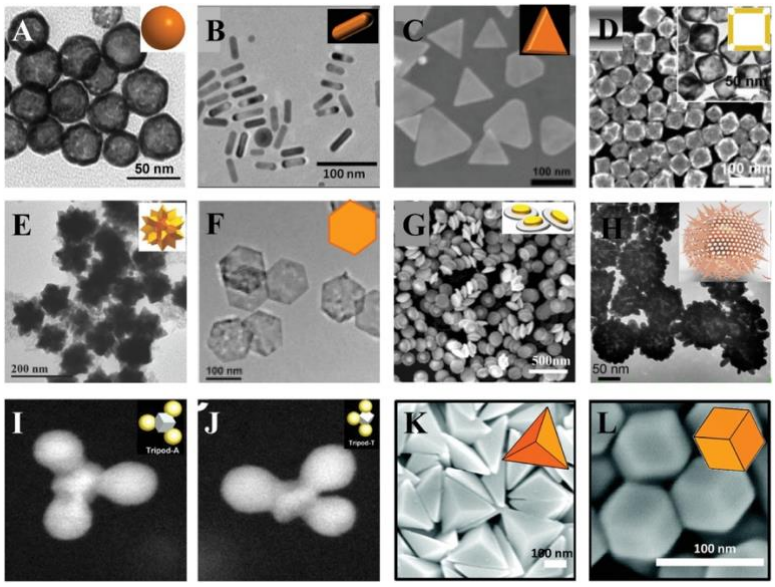

Figure 14. SEM and TEM images of gold nanocrystals of various categories: (A) nanospheres, (B) nanorods, (C) nanoprisms, (D) nanocages, (E) nanostars, (F) nanoplates, (G) nanodisks, (H) nanoshells, (I, J) nanotripods, (K) bipyramids, and (L) rhombic dodecahedrons. Image modifier from Ref. [111].

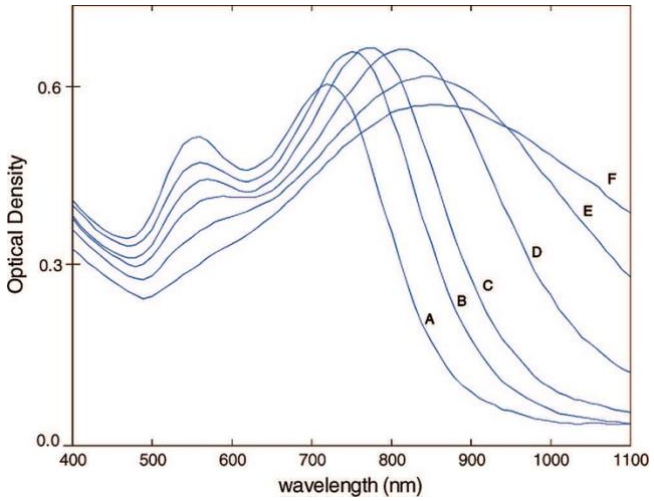

Figure 15. Absorption spectra of AuNSs of increasing size (A: 45 ± 4, B: 52 ± 4, C: 57 ± 5, D: 72 ± 6 E: 94 ± 9, F: 116 ± 11 nm) [112].

AuNS has a high surface area to volume ratio, high photothermal conversion efficiency, and can also be used as a carrier of drugs or photosensitizers, which has high loading efficiency [114, 115]. Furthermore, the sharp branches of AuNS can act as 'lightning antennas', strongly enhancing the onsite optical absorption [116, 117]. Such tunable increase in absorption can benefit not only PAI diagnosis but also photothermal therapy (PTT), a technique that has gained great attention in recent years with the goal of treating primary tumors and preventing metastatic cancer [118, 119]. The mechanism of PTT is similar to that mediating the photoacoustic effect, *i.e.*, it is based on tissue absorption, whereby light is converted into thermal energy after appropriate accumulation within tumors (Figure 16) [120, 121]. Consequently, AuNS represents an attractive choice of exogenous probe to probe (via PAI) and treat (via PTT) early-stage liver cancers. With optically absorbing AuNSs as microscopic heat sources, the therapeutic accuracy of PTT can be considerably improved while injury to the surrounding normal tissues can be minimized. In 2015, Wang *et al.* investigated the pharmacokinetics and biodistribution pathway of AuNS with multispectral optoacoustic tomography, showing that it can be rapidly cleared in the blood and accumulated in the liver and spleen [122]. The anticancer drug, doxorubicin (DOX),

carrier prepared by AuNS has excellent control ability for DOX release, which can realize photoacoustic diagnosis and chemotherapy-photothermal synergic therapy for tumors [73].

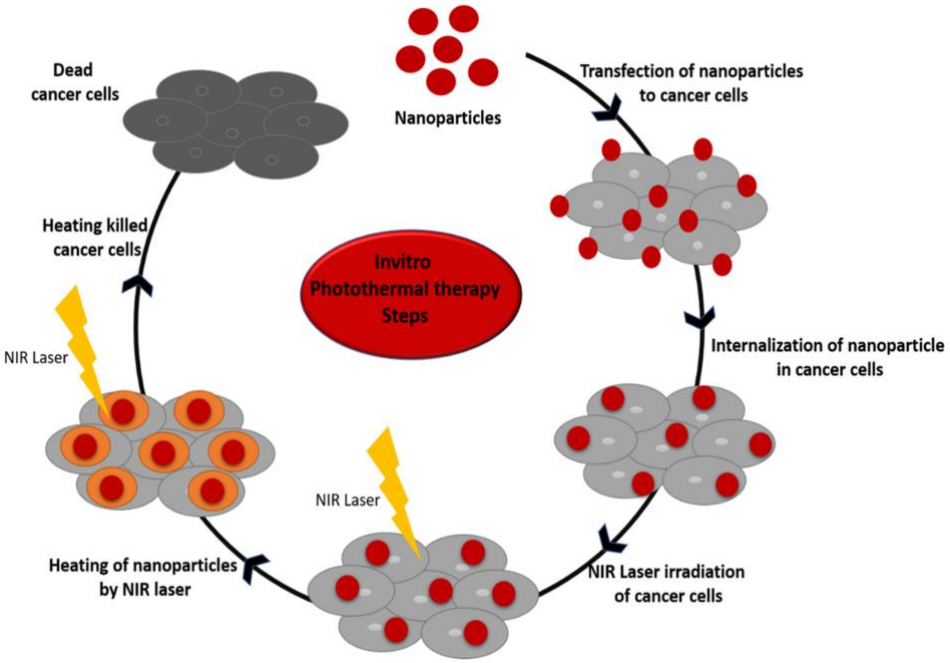

Figure 16. Illustration of the basic principle of photothermal therapy. Image modified from Ref. [121].

2.1.3 Red blood cell membrane coating strategy overcoming mononuclear phagocytic systems uptake

The efficiency of NPs delivery to the tumor sites is one of the challenges for NPs development [123]. MPS populate richly in organs like liver and spleen with a key function to filter out toxins and foreign invaders in the blood and maintain the stability of the blood [124]. This action, however, also prevents AuNS from reaching and accumulating at the target diseased site(s) [76], posing a major challenge of early liver cancer diagnosis: how to ensure an effective yet controllable accumulation of nanoprobes at the hepatic tumor. In the meanwhile, since NPs have 10^2 - 10^3 times greater probability of being sequestrated in the liver sinusoid than in the extra-hepatic circulation [76], the whole liver is “lightened” photoacoustically, resulting in a low SNR of liver tumor detection. Therefore, it is imperative to design novel nanoparticle

materials or structures to overcome the MPS clearance and effectively accumulate at hepatic tumors. To address this challenge, biologically natural or biomimetic nanostructures take their responsibility that allow them to escape the MPS [125, 126].

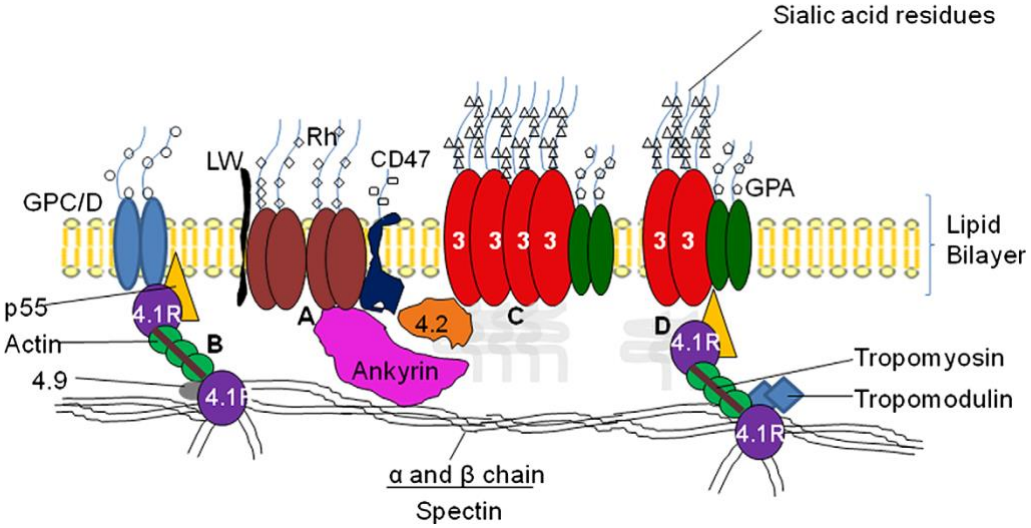

Figure 17. Simplified diagram of the RBC membrane structure. (A) Rh complex; (B) protein 4.1 complex; (C) and (D) are band 3 macrocomplex: (C) band 3 in tetrameric form and (D) band 3 in dimeric form. Image modified from Ref. [127].

The red blood cell membrane (RBCm) is one such promising option for *in vivo* liver applications due to its many advantages, including immune escape ability and prolonged blood circulation [128, 129]. Furthermore, "self-markers" on the surface of the RBCm, such as CD47 proteins, acidic sialyl moieties, and glycans (Figure 17), can be easily encoded to entrust NPs coated by the membrane with special biofunctions [130]. Therefore, RBCm-camouflaged NPs have great potentials in cancer applications, such as photothermal-chemotherapeutic synergistic treatment [131], photodynamic therapy [132], pro-drug delivery systems [133], and starvation therapy [91]. At the cellular level, NPs camouflaged by the erythrocyte membrane have been confirmed to exhibit immune escape and slower blood clearance [93, 134]. Benefits of reduced MPS clearance and prolonged blood circulation *in vivo* are obvious: a greater amount of probe can accumulate at the tumor site(s) and produce much stronger PA signals from the region of interest, resulting in improved diagnostic and therapeutic outcomes.

In this chapter, we will design and assemble a novel RBC membrane-coated AuNS probe (RBCm-AuNS) in this study (Figure 18). AuNSs with desired NIR absorption characteristics are enveloped with RBC membranes, which successfully eludes the MPS clearance and, at the same time, substantially enhances the accumulation of nanoprobes in the hepatocellular carcinoma model with prolonged circulation time. Such a clothed probe provides an effective and accurate model for the diagnosis and treatment of early stage liver cancer, as demonstrated experimentally. Three *in situ* tumors of mouse's liver smaller than 2 mm in diameter can be identified with PAI, and treatment with PTT can significantly reduce the tumor size and double the survival time of affected mice. Collectively, RBCm-AuNSs can potentially serve as a promising nanoprobe to improve the optical diagnosis and treatment of small liver tumors *in vivo*.

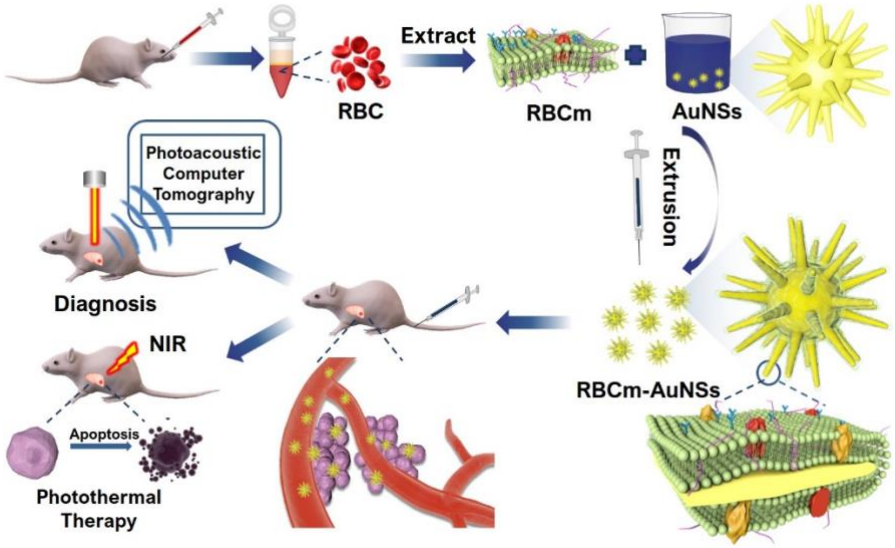

Figure 18. Schematic illustration of RBCm-AuNSs for enhanced liver cancer photoacoustic diagnosis and photothermal therapy.

2.2 Methodology

2.2.1 Synthesis and characterization of RBCm-AuNSs

RBC membrane-derived vesicles were prepared as described previously [135] with a few modifications. Briefly, whole blood (~2 mL) was collected from Kunming mice (males, 38 - 40 g) using a syringe that lightly pierced the submaxillary venous plexus. The blood was suspended in 10 mL erythrocyte preserving fluid and centrifuged at 3000 rpm for 5 min at 4°C to collect RBCs. RBCs were washed three times with ice cold 1× phosphate buffered saline (PBS) containing 1 mM EDTA-2Na, suspended in excess 0.25 mM EDTA-2Na in an ice bath for 12 h to allow for hemolysis to occur, and then collected again by centrifugation at 10,000 rpm for 15 min to remove serum and buffy coat. Following three washes with cold hypotonic solution, the collected RBC membranes were sonicated in a capped glass bottle for 10 min using a bath sonicator (Fisher Scientific, Waltham, MA, USA) set at 42 kHz and a power of 100 W. The resultant vesicles were subsequently extruded in sequence through 1000-nm, 400-nm, 200-nm, and 100-nm polycarbonate porous membranes using an Avanti mini extruder (Avanti Polar Lipids, Alabaster, AL, USA) (Figure 19).

Figure 19. The process of extrusion by Avanti Polar Lipids.

AuNSs were prepared using a seed-mediated growth method [136]. The gold seeds were firstly synthesized by adding trisodium citrate (6 mL, 1%) into a $HAuCl_4$ solution (40 mL, 1 mM) with heating (95°C) and stirring (500 rpm). After 5 min, a zinzolin gold seed solution was obtained, and heating and stirring were stopped to let the solution cool down to room temperature. Subsequently, $HAuCl_4$ (50 mL, 1 mM), HCl (0.2 mL, 1 M), and double-deionized water (150 mL) were mixed and stirred at 500 rpm. A 2-

mL aliquot of the gold seed solution was added to the mixture and let stand for 1 min. After that, $AgNO_3$ (2 mL, 2 mM) and ascorbic acid (2 mL, 0.1 M) were added simultaneously to generate the AuNS solution. The original AuNS solution was stored in the refrigerator at 4°C until use, following prior centrifugation at 6,500 rpm for 10 min.

To synthesize the final RBCm-AuNSs, we mixed the prepared RBC membrane-derived vesicles and AuNS solution at a 1:1 surface area ratio (S_{RBCm}/S_{AuNSs}), following the surface area analysis. The number of erythrocytes in 1 mm^3 (i.e., 1 μL) of mouse blood was 5×10^6, as reported, and the surface area of a single RBC was ~75 μm. Thus, the total surface area of RBCs (SRBC) in 1000 μL of blood was

$$S_{RBC} = 1000 \times 5 \times 10^6 \times 75 = 0.375 \times 10^{12}\ \mu m^2.$$

The AuNS NPs were spherical with a diameter (R) of ~104 nm according to the dynamic light scattering (DLS) measurements. As a result, the surface area of single AuNS NPs (S_0) was

$$S_0 = 4\pi R^2 = 4\pi \left(\frac{104}{2} \times 10^{-3}\right)^2 \approx 0.034\ \mu m^2,$$

and the volume of a single AuNS nanoparticle (V_0) was

$$V_0 = \frac{4}{3}\pi R^3 = \frac{4}{3}\pi \left(\frac{104}{2} \times 10^{-7}\right)^3 \approx 5.89 \times 10^{-16}\ cm^3.$$

As the mass density of AuNSs (ρ) is ~1 g/cm3, the mass of each AuNS nanoparticle (M_0) can be calculated as follows:

$$M_0 = V_0\rho = 5.89 \times 10^{-16} \times 1 \approx 5.89 \times 10^{-16}\ g.$$

Therefore, the total surface area of AuNS NPs in stock solution (10 mg/mL, 1 mL) was:

$$S_{\text{AuNSs}} = \frac{VC}{M_0} \times S_0 = \frac{1\times10\times10^{-3}}{5.89\times10^{-16}} \times 0.034 \approx 5.77 \times 10^{11}\mu m^2.$$

The mixtures were extruded sequentially through 400-nm and 200-nm polycarbonate porous membranes using an Avanti mini extruder. Afterwards, the mixtures were centrifuged at 10,000 rpm for 10 min to remove the excessive free RBC membrane vesicles and were washed three times with deionized water. The resultant RBCm-

AuNSs were then re-dispersed for further transmission electron microscopy (TEM), DLS, zeta potential, and ultraviolet-visible (UV-VIS) characterizations.

2.2.2 RBCm-AuNS characterization

The morphology of AuNSs and RBCm-AuNSs were characterized by TEM using a JEOL-1011 microscope (JEOL, Tokyo, Japan) with a 100-kV acceleration voltage. Zeta potential and size were analyzed with a ZEM 3600 Malvern Zetasizer (Malvern, UK). Optical absorption spectra were monitored using a UV-VIS-NIR spectrophotometer (Shimadzu, Kyoto, Japan). Sodium dodecyl sulfate-polyacrylamine gel electrophoresis (SDS-PAGE) was utilized to characterize membrane proteins.

2.2.3 Stability test of RBCm-AuNSs

The stability of RBCm-AuNSs were tested with the UV-VIS-NIR spectrophotometer by monitoring the change in optical absorption spectra. To this end, 100 μg/mL RBCm-AuNSs were dissolved in 5 mL FBS and stored at room temperature. Optical absorption spectra were recorded every 12 h.

2.2.4 Photothermal performance assay

Continuous 785-nm NIR laser illumination with a spot size of 4–5 mm was used to test the photothermal effect. The power density was 2 W/cm^2. The distance between laser source output and sample was set at 1 cm. Before irradiation, samples were dissolved in deionized water to achieve an RBCm-AuNSs concentration of 0, 20, 60, and 100 μg/mL, respectively. Then, 200 mL of each sample were used for photothermal measurements. Temperature variations of all samples were acquired using a FLUKE Ti25 infrared thermal imaging camera (Everett, WA, USA) at 50 s intervals, with an accuracy of 0.1°C. For optical stability detection, 60 and 100 μg/mL RBCm-AuNSs solutions were analyzed at 5-min intervals by fits and starts using the same laser conditions stated above. All experiments were conducted in triplicate.

2.2.5 Cell culture

Hep-G2 and HUH-7 cells were cultured separately in DMEM supplemented with 10% (v/v) FBS and 1% penicillin-streptomycin solution, under a 5% CO_2 atmosphere and 37°C. RAW264.7 cells were cultured in DMEM supplemented with 10% (v/v) FBS and 1% penicillin-streptomycin solution, under a 5% CO_2 atmosphere and 37°C.

2.2.6 Cytotoxicity assay

The cytotoxicity of probes was tested on Hep-G2 and HUH-7 cells. Cells were seeded at a density of 1×10^4/well in 96-well cell culture plates and incubated at 37°C under a 5% CO_2 atmosphere for 24 h. Then, cells were treated with various concentrations (0, 20, 60, 100, 140, 180, and 220 μg/mL) of RBCm-AuNSs (100 μL/well) for 24 h. Finally, 100 μL/well of CCK-8/culture medium (10 μL/100 μL) was supplemented in each well and the plates were incubated for an additional 3 h under the same conditions. A Synergy HT microplate reader (BioTek, Winooski, VT, USA) was used to measure the absorbance of each well at 450 nm (OD 450). The following formula was used to calculate cell viability: Cell Viability (%) = [(As-Ab)/(Ac- Ab)] × 100%, where As, Ac, and Ab represent the OD 450 of treatment group, control group, and blank, respectively.

2.2.7 *In vitro* PTT assay

We used calcein-AM and propidium iodide (PI) staining to visually test the photothermal effect of RBCm-AuNSs. Hep-G2 cells were seeded in 6-well plates at 37°C under 5% CO_2 atmosphere for 24 h. The original medium was washed off, followed by the addition of medium containing 60 μg/mL or 100 μg/mL RBCm-AuNSs, whereas medium without nanotubes was used as a control. After 4 h of continuous incubation, the cells were exposed to 785-nm laser illumination (1 W/cm^2) for 5 min in an already outlined area. Subsequently, the cells were washed gently twice with 1× Assay buffer, after which calcein-AM and PI were added. The cells were incubated for

another 15 min and visualized by an inverted Leica M205 FA fluorescence microscope (Leica, Jena, Germany).

For quantitative analysis, Hep-G2 cells were cultured at a density of 1×10^4/well in a 96-well plate at 37°C under a 5% CO_2 atmosphere for 24 h. Then, cells were randomly divided into four groups: control group, RBCm-AuNSs group, laser group, and RBCm-AuNSs with laser group. In the control group, cells were replaced with new routine culture medium as stated before. In the RBCm-AuNSs group and RBCm-AuNSs with laser group, cells were treated with various concentrations (10, 20, 40, 60, 80, and 100 μg/mL) of RBCm-AuNSs for 4 h. After that, cells in the RBCm-AuNSs with laser group were washed three times with PBS and then irradiated with a 785-nm laser under 2 W/cm^2 for 3 min. The same laser treatment procedure was applied also to the laser group but in the absence of RBCm-AuNSs. Afterwards, CCK-8 was used as discussed earlier.

2.2.8 Intracellular uptake assay

RAW264.7 cells were cultured to 70% confluence in a 10-mm dish at 37°C under a 5% CO_2 atmosphere, and were then incubated with DMEM containing 100 μg/mL RBCm-AuNSs for another 6 h. Following the incubation, DMEM was poured off from the dish without any rinsing, the cells were immediately covered with electron microscope fixative, and collected into a centrifuge tube by scraping them gently off the dish. After further addition of electron microscope fixative, the cells were fixed for 2 h at room temperature and then transferred to a 4°C refrigerator to be ready for subsequent experiments.

2.2.9 Biodistribution studies

For biodistribution studies, RBCm-AuNSs were first embedded with Cy7-NS for fluorescent imaging through a small animal optical molecular *in vivo* imaging system

(IVIS Spectrum; PerkinElmer, Waltham, MA, USA) assembled with an appropriate optical filter. RBCm-AuNSs and Cy7-NS were mixed at an 8:1 molar ratio and shaken overnight. Then, the mixture was centrifuged at 10000 rpm for 10 min, and the pellet was washed three times with dimethyl sulfoxide/PBS (v/v, 1:99) to remove any free Cy7-NS. Liver tumor-bearing mice were prepared by injecting 1×10^6 Hep-G2 cells into the livers of 3 mice. After 2 weeks-breeding, the mice were injected with 200 μL RBCm-AuNSs-Cy7 (2 mg/mL). Pilot pictures were taken using the IVIS before and 1, 3, 6, 8, 10, 12, 24, 36, 48, 60, 72 h after the injection to monitor the biodistribution of RBCm-AuNSs *in vivo*. After 72 h, the mice were necropsied; their organs and tumors were then used to study metabolic pathways by way of fluorescence intensity measurements. All animal procedures were carried out in accordance with the guidelines approved by the Animal Ethics Committee of the Chinese Academy of Sciences.

2.2.10 *In vitro* and *in vivo* PAI

For *in vitro* PAI, various concentrations (0, 20, 40, 60, 100, 150, and 200 μg/mL) of RBCm-AuNSs dispersions were filled into cylindrical phantoms made of agarose, which were then positioned in a Multispectral Optoacoustic Tomography (MSOT) system (iTheraMedical, Munich, Germany). The MSOT system contains an optical parametric oscillator laser with tunable wavelength to provide excitation for the PA effect. An arc transducer aligned with the laser detects the PA signals from the subject. ViewMSOT software was utilized to process the PA images after acquisition. For quantitative analysis, regions of interest were drawn over the sample, and their averaged PA intensity values were recorded and calculated.

For *in vivo* PAI, six male nude mice (BALB/c, 17–19 g, 5 weeks) were injected separately with 1×10^6 Hep-G2 cells into the liver and then bred for 2 weeks. These mice were randomly divided into two groups. After anesthetization with 5% isoflurane, the

mice were positioned in the MSOT system to acquire PA images at the liver section; this group of mice constituted the control group. Additional PA images at the same position were recorded at 1, 3, 6, 8, 12, 24, 36, 48, 60, and 72 h, after the mice received 200 μL of RBCm-AuNSs (2 mg/mL) intravenously. And the other group were treated with the same amount of AuNSs. PA signals from the AuNSs and RBCm-AuNSs were extracted using the unmixing spectra module of the imaging system to exclude signal contributions from oxy-/deoxy-hemoglobin *in vivo*. All mice were dissected at 72 h after imaging, with tumors being harvested, fixed with 4% paraformaldehyde, sectioned into slices, and stained with hematoxylin and eosin (H&E) for histological analysis.

2.2.11 *In vivo* PTT efficacy

Twenty-four liver tumor-bearing mice were prepared as described earlier. When tumor volume reached about 10 mm^3, mice were randomly divided into four evenly numbered groups: control group, RBCm-AuNSs group, laser group, and RBCm-AuNSs with laser group. In the control group, healthy mice did not receive any treatment. In the laser group, tumor-bearing mice were irradiated with a 785-nm laser (2 W/cm^2) for 5 min. In the other two groups, tumor-bearing mice received 200 μL of RBCm-AuNSs (2 mg/mL) intravenously, but only mice in the RBCm-AuNSs with laser group were also irradiated with a 785-nm laser (2 W/cm^2) for 5 min at 48 h post-injection. The temperature elevation of tumors was recorded during the photothermal treatment using an infrared thermal imaging camera. Body weight of each mouse from all groups was measured every other day. The mice were dissected after death, with tumors and major organs including the heart, liver, spleen, lung, and kidney being harvested, fixed with 4% paraformaldehyde, sectioned into slices, and stained with H&E for histological analysis.

2.2.12 Statistical analyses

GraphPad Prism 5 software (GraphPad Software, San Diego, CA, USA) was used for statistical analysis. A *t*-test was used to determine differences among different groups. **$p < 0.001$ and ***$p < 0.0001$ were considered statistically significant, whereas n.s. indicated no significant difference between the selected two groups.

2.3 Results

2.3.1 Synthesis and characteristics of RBCm-AuNSs

We successfully synthesized RBCm-AuNSs which have broad absorption spectrum and bio-protein characterization through the route illustrated in figure 18. Briefly, RBCm-AuNSs were prepared following two successive steps. First, AuNSs were synthesized by the seed-mediated growth method and appeared a blue-black color (Figure 20A) [136]. Then, the mixture containing RBC membranes and AuNSs were extruded through an Avanti mini extruder. The color of RBCm-AuNSs did not differ much from that of AuNSs (Figure 20B). The as-prepared AuNSs and RBCm-AuNSs were observed by TEM (Figure 21A, B). Semi-transparent membranes of less than 10 nm in thickness appeared tightly wrapped around the AuNS surface in a vacuum (Figure 21B). The hydrodynamic size of AuNS and RBCm-AuNS were tested by DLS and are shown in Figure 21C. The average diameter of RBCm-AuNS increased slightly from 103.6 nm (corresponding to that of AuNSs alone) to 125.4 nm. Such increase of 21.8 nm in diameter was attributed to the RBCm containing the lipid bilayer. The clothing process also shifted the zeta potential of AuNS from approximately -11.47 mV to -13.10 mV, the latter corresponding closely to the zeta potential of RBC membrane. Results from the TEM, DLS, and zeta potential measurements prove that RBC membranes successfully clothe the spiny AuNSs, and hence the as-prepared RBCm-AuNSs support their use for further experiments.

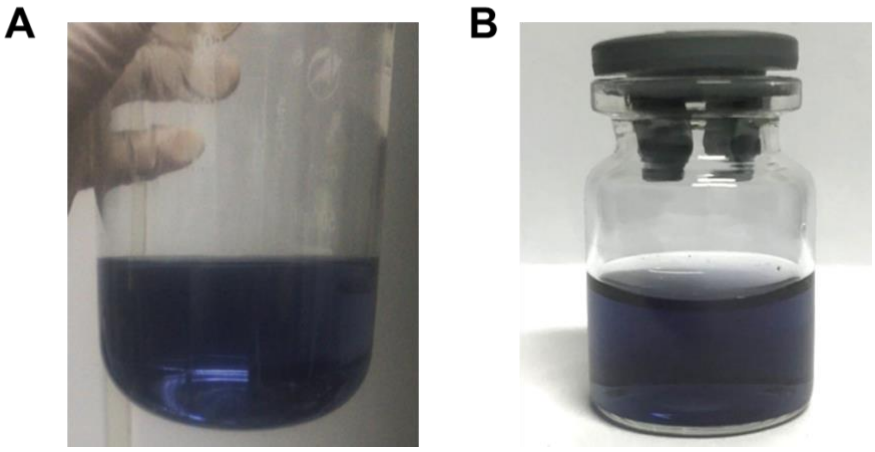

Figure 20. Appearance of AuNSs (A) and RBCm-AuNSs solutions (B).

Following the camouflage, complex membrane proteins on the surface of RBCm-AuNSs were examined by SDS-PAGE. Empty RBC membranes and AuNSs were employed as parallel controls. As shown in Figure 21D, empty RBC membrane and RBCm-AuNSs shared the same protein bands, whereas no bands were detected in the AuNSs lane, indicating that membrane proteins were preserved during the preparation of RBCm-AuNSs. The spectral absorption characteristic of RBCm-AuNS is also an important index for optical diagnosis and treatment. So, we measured the UV-VIS absorption spectrum of RBCm-AuNSs. It exhibited a broad and strong absorption in the NIR region from 600 to 1000 nm (Figure 21E), making it promising for both photoacoustic and photothermal effects. It is worth noted that the characteristic absorption peaks of RBCm-AuNSs can be distinguished from that of deoxyhemoglobin (Hb) and oxyhemoglobin (HbO_2). This allows for reliable extraction of signals contributed by the probes from the blood background during *in vivo* imaging. These results suggest that we have successfully synthesized RBCm-AuNSs, which retain the original structural features of both AuNSs and RBC membranes.

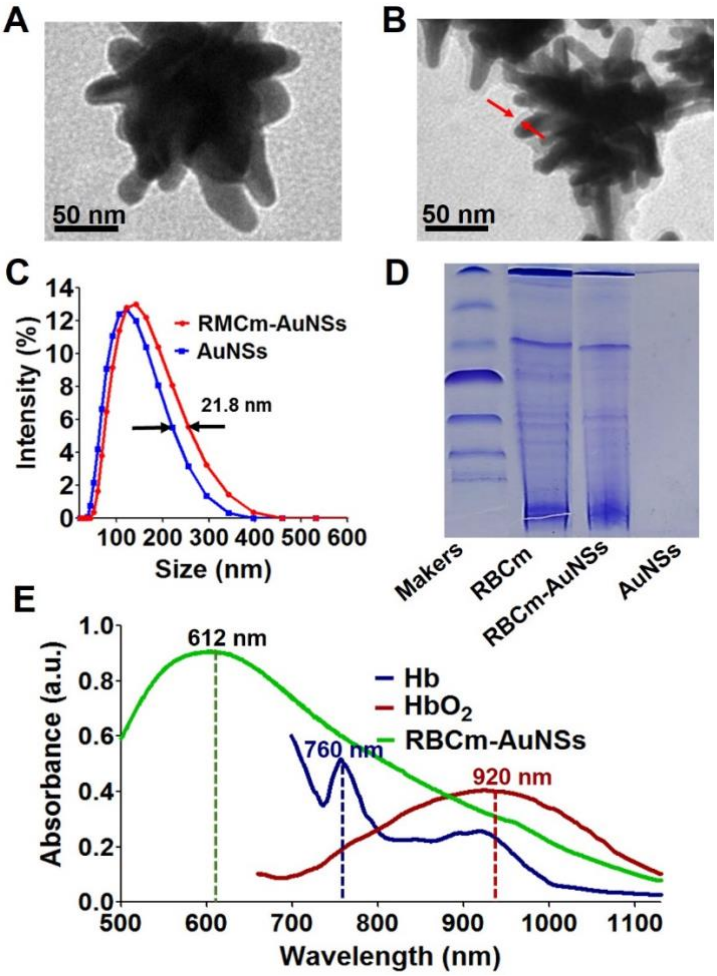

Figure 21. Characterization of RBCm-AuNSs. TEM images for uncoated AuNSs (A) and RBCm-AuNSs (B), respectively. (C) Hydrodynamic size of AuNSs and RBCm-AuNSs as measured by DLS. (D) SDS-PAGE protein analysis of empty RBCs, RBCm-AuNSs, and AuNSs, respectively. (E) UV-vis spectra of RBCm-AuNSs in water (100 μg/mL) and the standard absorption spectra of Hb and HbO_2 (obtained from MSOT).

2.3.2 The photoacoustic property of RBCm-AuNSs *in vitro*

Due to the strong absorption of RBCm-AuNSs from 600 to 950 nm, the as-prepared probes were expected to produce strong PA emissions. To assess that, phantom samples with different probe concentrations were tested using the MSOT system. As seen, the brightness increases with the probe concentration (Figure 22A). Actually, the PA signal strength, as measured by the pixel intensity, reveals an upward trend and a linear relationship with the concentration of RBCm-AuNSs (R^2 = 0.9922) of the sample

(Figure 22B). Therefore, the accumulation of the as-prepared probes allows us to better image the target site(s) photoacoustically. Note that. However, excessive probe concentration may result in osmosis that may affect the viability and activity of normal cells.

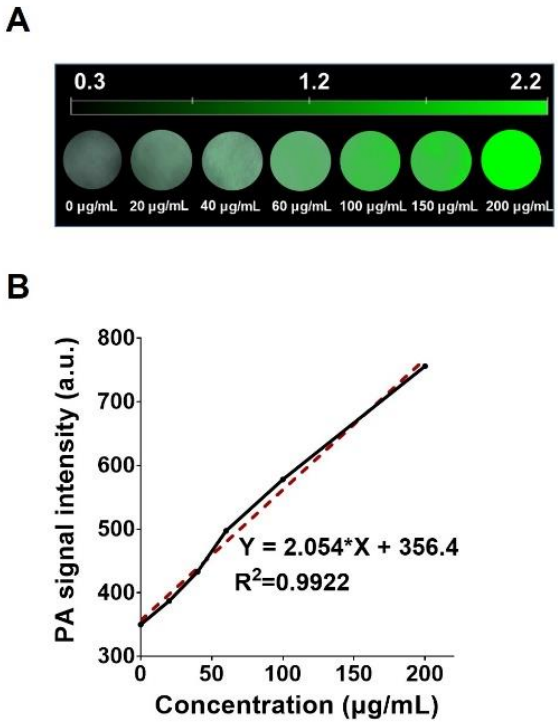

Figure 22. (A) PA images of phantom samples contains various concentrations of RBCm-AuNSs (0, 20, 40, 60, 100, 150, and 200 μg/ml). (B) *In vitro* PA signal strength versus RBCm-AuNSs concentration.

2.3.3 Stability, cytotoxicity evaluation and intracellular uptake of RBCm-AuNSs

In order to prove the beneficial properties of RBCm-AuNSs *in vivo*, their stability in FBS were examined. Even after suspending RBCm-AuNSs in FBS for 3 days, the absorption peaks at 415 nm were almost unchanged (Figure 23A), attesting to a stable structure of RBCm-AuNSs in FBS. The result suggests that RBCm-AuNSs can maintain effectiveness and performance *in vivo*. Moreover, owing to the camouflage provided by the RBC membrane extracted from mice, biomimetic RBCm-AuNSs were expected to be inherently non-toxic. To verify the hypothesis, we separately incubated

two types of cells, Hep-G2 and HUH-7, with RBCm-AuNSs. As depicted in Figure 23B, both cell lines yielded survival rates of >90% after incubation with gradient concentrations from 20 to 220 μg/mL of RBCm-AuNSs. As the concentration increased, cell activity tended to decrease slightly, probably due to the effect of osmosis. Nevertheless, both Hep-G2 and HUH-7 cell lines displayed relatively high cell viability following the addition of RBCm-AuNSs, proving that RBCm-AuNSs do not cause major cytotoxicity.

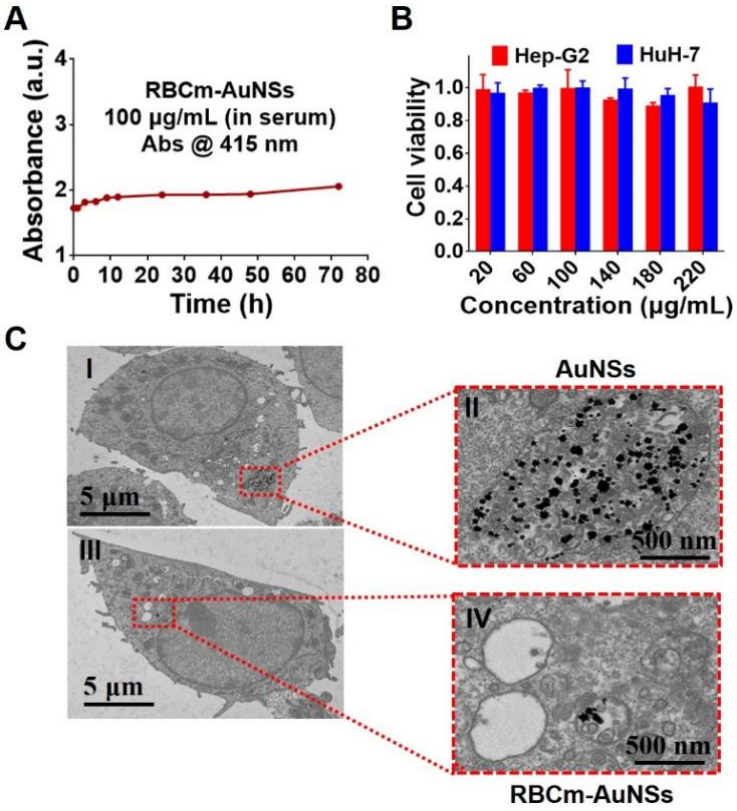

Figure 23. (A) Stability of optical absorption of RBCm-AuNSs dissolved in the serum stored under the room temperature for 3 days. Note that the observed slight increase of RBCm-AuNS absorption is probably caused by the vaporization during the course. (B) Cell viability of Hep-G2 and HuH-7 cells incubated with RBCm-AuNSs of various concentrations (20, 60, 100, 140, 180, and 220 μg/mL) for 24 h, respectively. (C) Cellular uptake by TEM of RAW264.7 cells cultured with AuNSs and RBCm-AuNSs, respectively, at 37 °C for 6 h. The dark spots in II and IV represent the unclothed and clothed AuNSs, respectively.

To confirm that RBC membranes could help the nanoprobe escape the MPS clearance, intracellular uptake of AuNSs and RBCm-AuNSs was investigated in RAW264.7 phagocytes. As presented in Figure 23C, substantially more AuNSs (Figure 23C I and II) than RBCm-AuNSs (Figure 23C III and IV) were trapped in RAW264.7 cells, suggesting that unclothed AuNSs are removed much more easily from the blood by the MPS. It also proves that AuNSs acquire sound capability to escape the MPS clearance after being wrapped by the erythrocyte membranes. It also should be clarified that the TEM images shown in Figure 23C do shown considerate morphology deformation to AuNS and RBCm-AuNS. Note, however, these probes are engulfed by phagocytes, being enclosed in the organelles of phagocytes; the action of intracellular forces and intracellular factors have deformed the probes [137]. In PA and PTT experiments, most RBCm-AuNS are free from the MPS. Thus, the abovementioned morphology and optical absorption deformations will not happen.

2.3.4 *In vivo* distribution of RBCm-AuNSs

To explore the biodistribution of RBCm-AuNSs *in vivo*, we used traditional fluorescence imaging. The circulation time of RBCm-AuNSs in mouse blood lasted for up to 72 h, as determined by the continuous monitoring of fluorescence intensity variations at time intervals before and 1 to 72 h after intravenous administration (Figure 24A). Note that the RBCm-AuNSs were not completely metabolized within 72 h, and the main pathway for its removal was *via* the kidney (Figure 24B). RBCm-AuNSs quickly accumulated in the liver, with the liver-to-background ratio reaching ~14 at 1 h (Figure 24C). To learn more about the accumulation of RBCm-AuNSs at the tumor site, we calculated the fluorescence intensity ratio between the strongest region (presumably the tumor site) and its neighborhood. The result is shown in Figure 24D, from which the retention of RBCm-AuNSs in the tumor is obvious: an increased concentration ratio is seen, ascribing to MPS escaping and accumulation of the clothed

nanoprobes. However, due to the low resolution of traditional fluorescence imaging caused by optical scattering, we could not discern the precise boundaries and features of the tumor. After monitoring the biodistribution of RBCm-AuNSs, the mouse was necropsied, and fluorescence intensity was measured directly in the organs and tumors to study the metabolic pathways participating in RBCm-AuNS clearance. The fluorescence signal at the tumor site was ~8×10^8, confirming the accumulation of RBCm-AuNSs in the liver tumor. This result confirmed that RBCm-AuNSs could escape elimination by the MPS and thus could accumulate at and be used to locate the liver tumors.

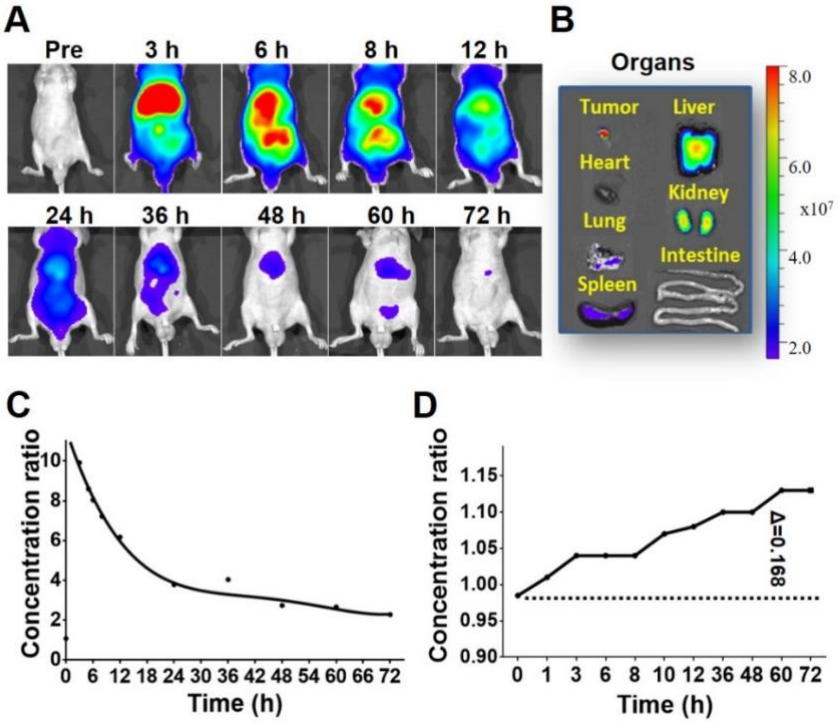

Figure 24. In vivo imaging and biodistribution of RBCm-AuNSs after intravenous injection. (A) The fluorescence images of Hep-G2 tumor bearing mouse at different time points. (B) The fluorescence image of organs dissected from the mouse after 72 h. (C) The ratio of the liver's signal value to the paw's over time. (D) The signal ratio between the strongest region (presumably the tumor site) and its neighborhood over time.

2.3.5 In vivo photoacoustic imaging and accumulation of RBCm-AuNSs at the tumor *site(s)*

In practice, the exact tumor site could be clearly detected only under dissection during fluorescence imaging. To avoid such procedure and obtain noninvasive high-resolution imaging of tumors, *in vivo* PAI experiments were performed following the protocols detailed in Section 2.11. Based on the *in vitro* photoacoustic property test for different probe concentrations (Figure 22), we injected intravenously 200 μL of a 2 mg/mL RBCm-AuNSs solution (determined by the mouse blood volume) into mice for *in vivo* detection. In comparison, the same amount of AuNSs were injected to another group of mice. Since the laser wavelengths were chosen to distinguish the peak absorption of the nanoprobes, Hb and HbO_2, the PA signal strength can be directly linked with the enrichment of the unclothed and clothed probes. As we can see from Figure 25A, with AuNSs the PA signal was strongest after 1-3 hr of injection due to the accumulation of probes in the blood. After that, the PA signal became weaker and weaker, suggesting that the unclothed probes at the moment had been mostly cleared by the MPS, even though. With RBCm-AuNSs, however, the circulation time of the probe *in vivo* was doubled and lasted for more than 72 h (Figure 25B), which is consistent with the time duration obtained by fluorescence imaging. The prolonged circulation time is attributed to the erythrocyte membrane that helps to camouflage the nanoprobes from being cleared by the MPS. This is critical for allowing gathering of the RBCm-AuNSs at tumor sites. It also further confirms that the liver sinusoid is a blood rich environment that allows accumulation of clothed probes for the gathering of the RBCm-AuNSs at the tumor sites. More importantly, at 60 h after RBCm-AuNSs tail intravenous injection, PAI revealed three small hepatocellular carcinomas of less than 2 mm in diameter (Figure 25B), and the SNR of imaging is increased by about 55% (from 1.17 to 1.82; Figure 26). The pathological morphological features of the tumor sites were validated by analyzing the anatomy (Figure 25C, D) and histological analysis with H&E staining of the mouse liver (Figure 25E). The benefits of RBCm-AuNSs escaping the MPS *in*

vivo are convincing: more RBCm-AuNSs enrich in tumor result in much higher SNR of PA detection due to a small amount of nanoprobe discharge and prolonged circulation time. It should be noted that such an outstanding imaging capability in terms of localization, resolution, and contrast from PAI is not possible with fluorescence imaging. Collectively, the use of RBCm-AuNSs enables the application of PAI for the *in vivo* early diagnosis of *in situ* liver cancer.

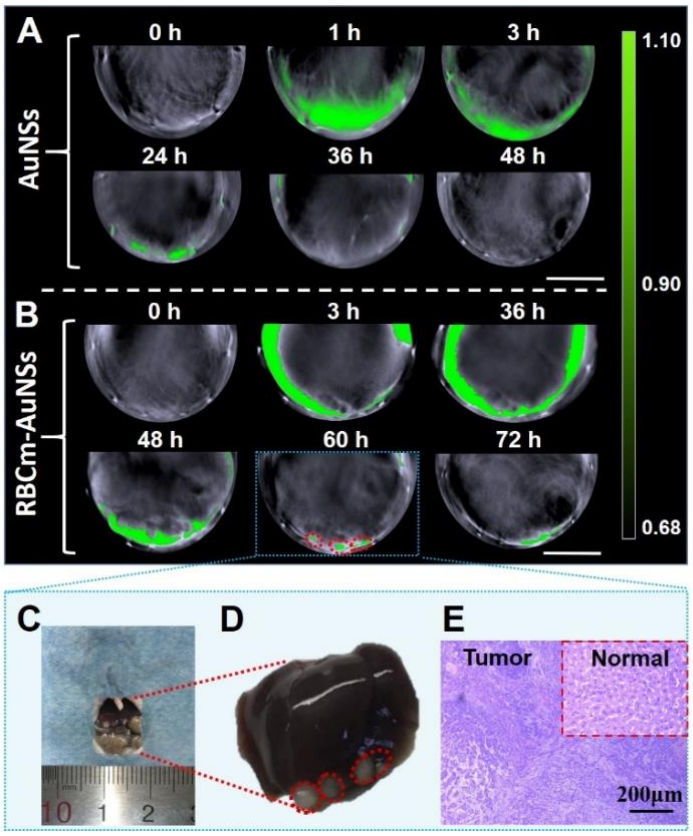

Figure 25. In vivo PA images of Hep-G2 tumor-bearing mice at the liver site, before injection (0 h) and 1, 3, 24, 36, 48 h after the injection of AuNSs (A), and 3, 36, 48, 60, 72 h after the injection of RBCm-AuNSs (B). Three tumor sites were revealed from the PAI in RBCm-AuNSs group. Scale bars =10 mm. C&D. The anatomy of the mouse liver after photoacoustic imaging. E. H&E staining images of tumor tissue and normal tissue of the liver.

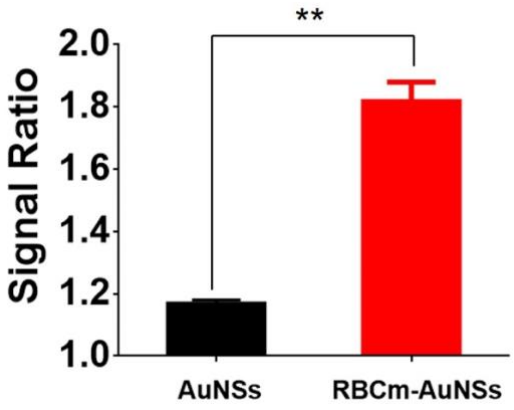

Figure 26. The signal ratio of AuNSs and RBCm-AuNSs in PAI.

2.3.6 *In vitro* photothermal effect and photothermal therapy with RBCm-AuNSs

We tested the photothermal conversion efficiency of RBCm-AuNSs after confirming their broad absorption spectrum and PA diagnosis capability. As shown in Figure 27A, the temperature of solutions containing different concentrations of RBCm-AuNSs (20, 60, 100 μg/mL, respectively) increased substantially with exposure time, and the higher is the probe concentration, the larger is the temperature increase. In contrast, the temperature of the PBS solvent experienced small changes as it failed to absorb much NIR light energy. Thus, the observed heat accumulation was attributed primarily to the RBCm-AuNSs. In Figure 27B, the temperature changes are quantified: the RBCm-AuNSs solutions exhibited a substantial rise in temperature, from the basal room temperature to averaged 48.0 and 62.8°C after irradiation for 500 s at 60 and 100 μg/mL, respectively. With identical exposure time, the photothermal effect became stronger at higher concentrations of the RBCm-AuNSs. Thus, RBCm-AuNSs could convert light energy into heat efficiently and raise the medium temperature to >45°C, which is sufficient for the photothermal treatment of tumors. A concentration of only 60 μg/mL is required to reach the effective cell-killing temperature within 250 s. Considering the signal degeneration caused by a prolonged exposure, the photostability of RBCm-AuNSs was examined through successive exposures to NIR illumination. As shown in Figure 27C, light irradiation and blockage modes were switched every 5 min, yet only negligible changes in the peaks and valleys were observed over the tested period,

indicating good photostability of RBCm-AuNSs. Therefore, RBCm-AuNSs exhibit excellent performance of photothermal conversion ability and photostability.

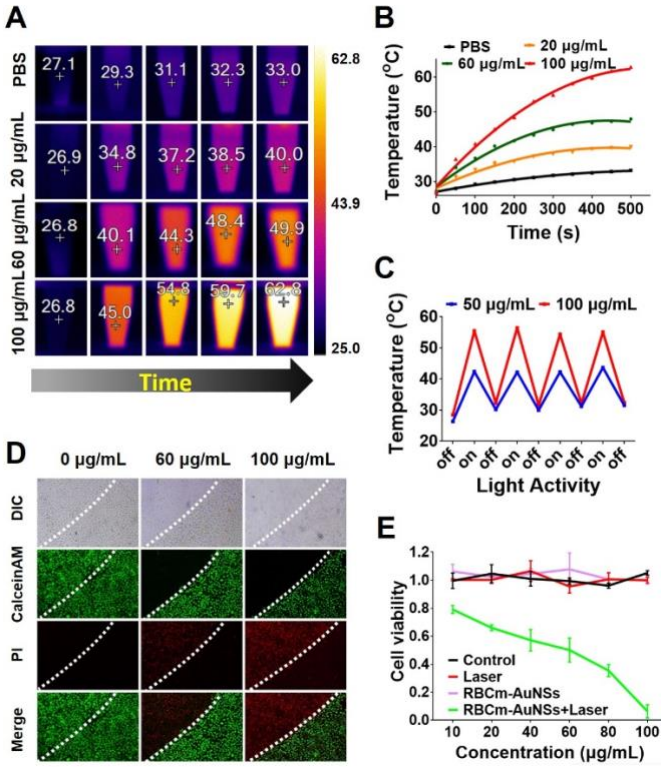

Figure 27. (A) Photothermal responses of various concentrations of RBCm-AuNSs as measured by an infrared thermal camera. (B) Photothermal responses of solution suspensions with various concentrations of RBCm-AuNSs, with PBS as a reference. (C) Temperature changes of RBCm-AuNSs suspensions upon five circles of NIR light irradiation-blockage gating (785 nm, 2 W/cm^2). (D) CLSM images of Hep-G2 cells stained with Calcein-AM and PI after incubation with 60 and 100 μg/mL of RBCm-AuNSs and NIR laser irradiation (incubation time = 4 h, 785 nm, 2 W/cm^2, irradiation time = 300 s). (E) Cell viability, representing the *in vitro* PTT efficacy, of RBCm-AuNSs of various concentrations on Hep-G2 cells upon NIR laser irradiation (Incubation time= 4 h, 785 nm, 2 W/cm^2, irradiation time = 300 s). Data was mean ± standard deviation with n=3.

The photothermal effect of RBCm-AuNSs against Hep-G2 cells was confirmed by fluorescence microscope with calcein-AM and PI staining. Calcein-AM is a cell-

permeable dye that labels living cells, whereas PI is a cell-impermeable dye that only labels dead cells. Green channel images were obtained from Calcein-AM (λ excitation / λ emission, 495/515 nm), while red channel images were obtained from PI (λ excitation / λ emission, 535/617 nm). As shown in Figure 27D, the control group (with 0 μg/mL RBCm-AuNSs) areas exhibited almost identical green fluorescence with and without laser treatment, confirming the presence of live cells. In comparison, in the 60 and 100 μg/mL RBCm-AuNSs groups, Hep-G2 cells display noticeable red fluorescence at the exposed areas, intuitively illustrating the striking photothermal effect of the RBCm-AuNSs. Notably, bright green fluorescence could be still detected at regions not exposed to laser irradiation, indicating that RBCm-AuNSs themselves did not cause tumor cell death. Moreover, the higher was the concentration of RBCm-AuNSs, the more lethal was its effect. Such an ablation capability proves that RBCm-AuNSs constitute an effective tool to eliminate cancerous cells based on the photothermal effect.

Photothermal lethality was further measured by the CCK-8 assay on different groups of cells. As reported in Figure 27E, cell viability showed only minimal fluctuations for the different concentrations and the different treatment groups. Only in the case of cells subjected to both RBCm-AuNSs and laser exposure, viability appeared to drop drastically with the concentration increasing, and nearly all cells being counted as dead at 100 μg/mL. These results are consistent with fluorescence microscope imaging, proving that RBCm-AuNSs or laser exposure alone have a negligible treatment effect, but their combination leads to a powerful photothermal effect against tumors.

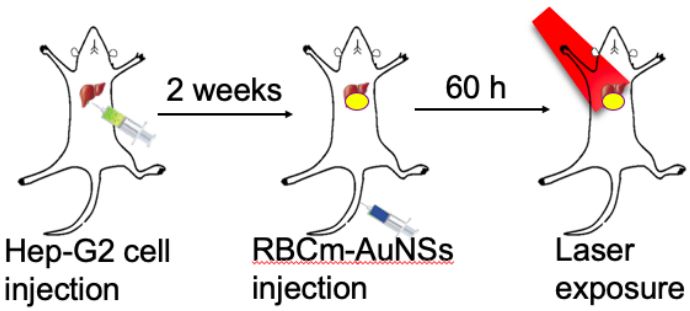

Figure 28. Illustration of the process of PTT with RBCm-AuNSs on the mice infected liver cancer. After building liver cancer mode by inject Hep-G2 cell into mouse liver, we injected the probe by tail vein injection. Then the mouse liver was treated by laser exposure at 60h, the highest level of SNR.

2.3.7 In vivo photothermal treatment with RBCm-AuNSs

The accurate detection of small tumors enabled by the clothed nanoprobes and PA image could allow the treatment of liver cancer at an early stage, which is crucial to foster long-term survival. To experimentally demonstrate this possibility, the *in vivo* photothermal antitumor experiment was explored on four different groups of mice with hepatocellular carcinoma (Figure 28). Figure 29 shows the temperature changes during photothermal treatment of mice in different groups. Figure 30A presents the changes in body weight of each group of mice over time. The increase in body weight observed in the control and laser groups in the later stage may be attributed to Hep-G2 cells entering a period of exponential proliferation, which enlarged the tumors. Note that, for statistical purposes, the end time here was set to the date of all deaths in the control group (no probes or laser treatment). Mice subjected to RBCm-AuNSs treatment and laser irradiation weighted substantially more than those in the other three groups throughout the course of the experiment, suggesting that photothermal treatment was effective and that mice in this group became much healthier. Such a significant beneficial effect was also observed when comparing the survival of each group over a period of 100 days.

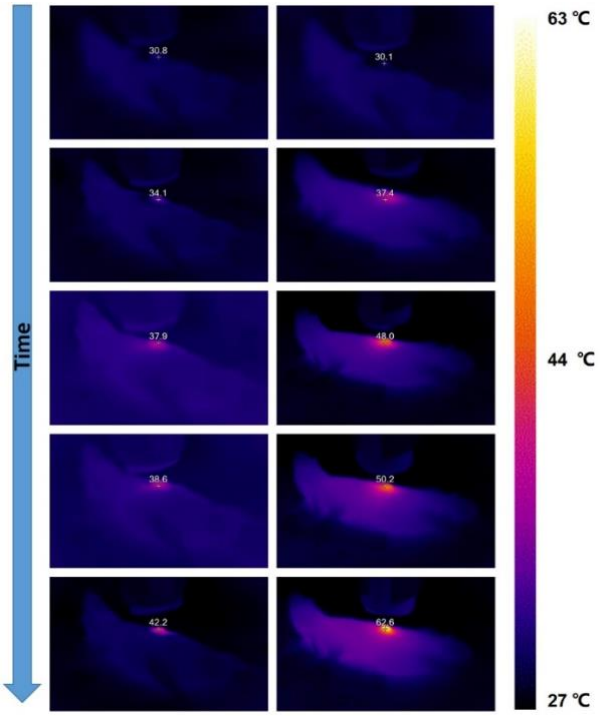

Figure 29. Photothermal responses of mice in the Laser (only) group (left column) and the RBCm-AuNSs with laser group (right column) as measured by an infrared thermal imaging camera.

As shown in Figure 30B, mice from the RBCm-AuNSs with laser group exhibited the longest life span, approximately 85 days. In contrast, the RBCm-AuNSs and control groups displayed similar life spans of 40 days and the laser treatment group is 45 days. Immediately after death, the mice were dissected, and the tumors and organs were isolated. As can be seen in Figure 30C, mice from the RBCm-AuNSs with laser group exhibited an almost complete disappearance of tumors following photothermal treatment, as indicated by the corresponding tumor weight. Combining tumor weight with body weight, revealed that the increase in the body weight observed in Figure 30A was due to an increase in tumor proliferation, with the tumor weighting up to 3.3 g. Finally, histological analysis with H&E staining of organs in each group revealed that the RBCm-AuNSs induced no or little toxicity in healthy organs (Figure 30D). This result again confirms the safety of the RBCm-AuNSs *in vivo*. Collectively, RBCm-

AuNSs can be used as an effective tool for photothermal treatment of hepatocellular carcinoma without damage to other healthy organs *in vivo*.

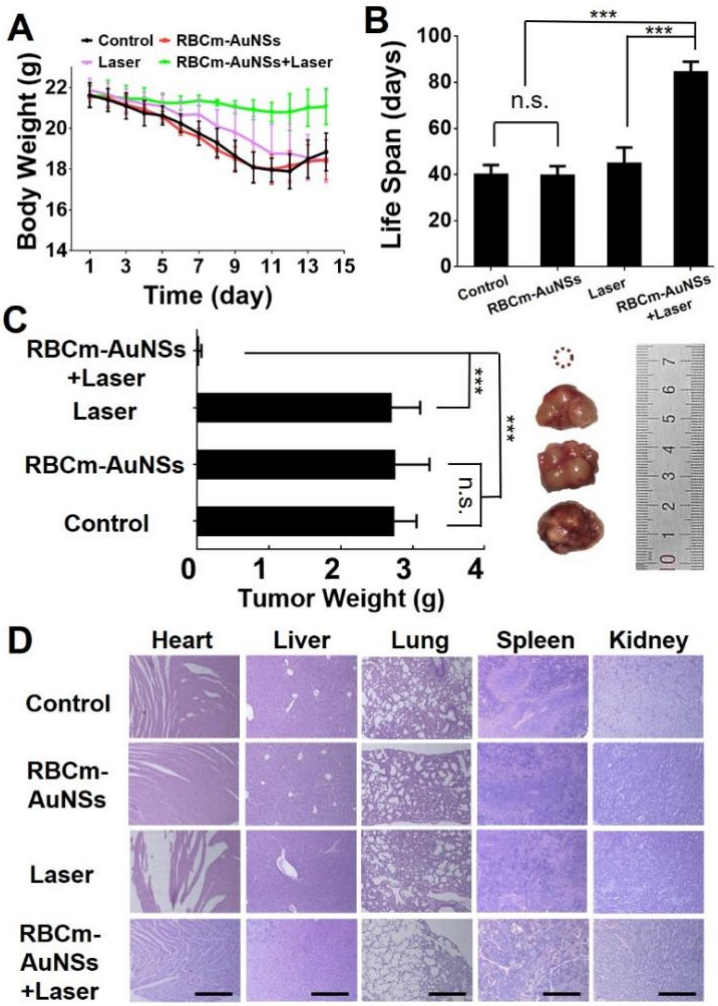

Figure 30. *In vivo* photothermal treatment. (A) Body weight of tumor bearing mice as a function of time for different groups. (B) The life span of tumor bearing mice of each group. (C) Tumors tissues dissected from each group after death and the comparison of tumor weight of different groups. *p < 0.01, **p < 0.001, ***p < 0.0001 and n.s. represents no significance. Data was mean ± standard deviation with n=6. (D) H&E staining images of major organs (heart, liver, spleen, lung, and kidney). Scale bars = 200 μm.

2.4 Discussion

MPS clearance, one of the major challenges for the use of NPs *in vivo*, restricts the enrichment of NPs in the tumor and hampers the enhancement to the diagnosis and treatment of liver cancer [76, 124]. The *in vivo* use of spiny nanoprobe composed of AuNSs sees no exception, although it possess excellent thermal performance and broad absorption wavelength range even in the NIR [138]. In this study, RBC membranes were applied to camouflage the AuNSs to reduce its rejection as foreign material. The results of TEM, DLS, zeta potential measurements and SDS-PAGE test demonstrated that the RBC membranes successfully clothed the spiny nanoprobes, while retaining the essential protein characteristics (Figure 21A-D). The absorption spectrum of the clothed nanoprobes is broad and had a strong peak that can be clearly distinguished from that of oxy- and deoxy-hemoglobin (Figure 21E). This allows for reliable extraction of PA signals contributed by the probes from a complex background such as a blood-rich environment. The result of photoacoustic property of RBCm-AuNS affirms it could be effective and excellent as a photoacoustic probe (Figure 22).

To assess the stability and safety of RBCm-AuNSs *in vivo*, serologic stability and cytotoxicity were tested, finding sound stability (Figure 23A) and negligible toxicity (Figure 23B). To verify the RBCm coating can help AuNSs to avoid the immune clearance, intracellular uptake in mouse macrophage cell lines (RAW 264.7), the main component of MPS [139], was studied. The results showed that phagocytes ingested much less RBCm-AuNSs than AuNSs (Figure 23C), indicating RBCm-camouflaged spiny nanoprobes can evade the recognition by the MPS. Therefore, with modified nanoprobes, longer circulation in the body and stronger accumulation at the tumor sites are expected (Figure 24). The hypothesis is that with prolonged circulation time, it is more conducive to passive targeting accumulation at the hepatic tumor due to the abundant blood in the liver sinusoid, leading to a high concentration environment of nanoprobes coated with RBCm.

Stronger immunity to the MPS clearance is also reflected from the imaging results: earlier studies [140] with AuNSs as the probe experienced substantial fluorescent signal reduction at 24 h, which is quite consistent with our photoacoustic observation (Figure 25A). With RBCm-AuNSs, the probing window for both fluorescent and photoacoustic imaging was considerably extended to up to 72 h (Figure 24A and Figure 24B). And the increase of SNR of fluorescence signal in Figure 24D also indicates that more nanoprobes have successfully escaped the sequestration of MPS in the liver and effectively accumulated at the tumor sites. It should be pointed out that, even though fluorescence imaging can also be used for cancer imaging and diagnosis, it cannot detect or localize small liver tumors due to limited resolution at such tissue depths [141]. Hence, PAI imaging is sought for to obtain ultrasonic resolution detection of optical absorption contrast. In experiment, PAI clearly revealed three isolated *in situ* small liver tumors with dimension smaller than 2 mm in diameter under the assistant by the RBCm-AuNSs at 60 h after intravenous injection. The SNR at 60 h is 1.82, which is much higher than that with AuNSs (the number is 1.17) (Figure 26). Such a precise diagnosis of early-stage liver cancer allows the noninvasive irradiation of tumor sites for photothermal treatment, and the elevated concentration of clothed nanoprobes also significantly benefits the photothermal treatment outcomes: considerably more heat were generated precisely at the tumor sites and killed tumor cells efficiently, resulting in healthier (Figure 30A) and longer (Figure 30B) life and complete disappearance of tumors (Figure 30C). Thus, RBCm-AuNSs-assisted laser treatment was seen to substantially improve the curative prospects of *in situ* liver cancer. To this point, we have clearly demonstrated that RBCm-AuNSs could evade the MPS， prolong the circulation time *in vivo,* and increase the possibility of nanoprobe enrichment at the tumor sites, which leads to enhanced photoacoustic and photothermal effects.

2.5 Summary of this study

To overcome the *in vivo* clearance of NPs mediated by MPS, RBCm-AuNSs were designed and synthesized in this study. Following extensive characterization, the RBCm-AuNS was found to exhibit a broad and preeminent NIR absorption spectrum, to be sufficiently stable over time, and to retain the intrinsic protein characteristics of the encapsulating RBC membrane. High photothermal conversion efficiency and favorable photostability have also been proved, leading to significantly enhanced photoacoustic and photothermal capabilities. After its feasibility assessment *in vitro*, the RBCm-AuNS was used for the accurate diagnosis and treatment of mice bearing liver cancer. Assisted by the RBCm-AuNSs, photoacoustic imaging could reveal not only the existence, but also the location and dimension of tumors smaller than 2 mm in diameter. Effective photothermal treatments have also been shown in our study. Collectively, our erythrocyte membrane-camouflaged AuNSs significantly improves the biocompatibility of NPs for *in vivo* use. If further advanced, the probe potentially provides a promising tool to assist the noninvasive diagnosis and treatment of early-stage cancers towards translational and clinical applications.

Chapter 3 Cancer cell membrane-functionalized nanoplatform driven by brain-blood-barrier breaking enables deep penetrating and sensitive targeted magnetic particle imaging and photothermal therapy of early glioblastoma

This chapter is reproduced with some adaptations from the manuscript "X. Huang, H. Hui, W. Shang, P. Gao, Y. Zhou, W. Pang, C. Woo, J. Tian and P. Lai. Deep penetrating and sensitive targeted magnetic particle imaging and photothermal therapy of early-stage glioblastoma based on a biomimetic nanoplatform". The contributions of authors are as follows: X. Huang, P. Lai, and J. Tian contributed the idea. X. Huang designed and ran the experiments. All authors were involved in the analysis and discussion of the results and manuscript preparing.

The effect of nano-probes in brain glioma imaging is unsatisfactory due to the presence of BBB and complex anatomy structure of the brain, which impede the delivery of theranostic agents to the tumor site. In this chapter, we propose a biomimetic magnetic nanoparticle (MNP) as a BBB breaking through-driven sequential glioma-targeted tracer and examine MPI's properties in cancer application.

3.1 Motivation of this study

3.1.1 MPI for glioma diagnosis

Glioblastoma multiforme (GBM), a grade IV astrocytoma in the World Health Organization (WHO). Classification of Tumors of the Central Nervous System, is one of the most aggressive malignancies [142, 143]; the average 5-year survival rate for patients with glioblastoma is only 6.8% because the diffusion may blur the boundary between the tumor area and normal tissue, resulting in an ineffective surgical excision . That said, if it is diagnosed early and treated appropriately, the survival period of gliomas can be considerably prolonged [144, 145]. Therefore, it is imperative to establish early, stable, and reliable cancer diagnosis methods to prolong the survival of

GBM patients [12, 13]. However, conventional imaging methods, such as MRI and CT, are inaccurate in determining the size and location of brain tumors, while optical imaging is constrained by strong scattering of light in tissue and hence limited tissue penetration depth, even at near-infrared II wavelengths [17, 146]. More importantly, these techniques lack the required sensitivity and specificity for predicting tumor aggressiveness and differentiating tumor progression from nonspecific treatment-related adjustments [147, 148]. According to the Gompertzian growth curve for solid tumors, proliferation of tumor cells triggers the angiogenesis when the number of cells is around 1×10^5, which in turn promotes the formation of tumor microenvironment, logarithmic increase of tumor cells, and eventually the tumor growth [3, 7, 149]. For early-stage tumors that are geometrically smaller than $1mm^3$, they can hardly be detected by present imaging techniques. As introduced in Chapter 1, MPI has an unique advantage of no background tissue signal and excellent imaging contrast due to limit existence of superparamagnetic nanoparticles in native biological tissues, which is different from the universal distribution of ^1H in water and biological tissues as detected in MRI [150-152]. So far, MPI has been exploited for different applications, such as cardiovascular, cerebral ischemia, and pulmonary imaging [61, 153, 154]. More promisingly, MPI overcomes the penetration depth limitation of optical imaging and exhibits high sensitivity, being able to quantize as few as 200 cells [57], which has immense potentials for early glioma diagnosis [59, 155, 156].

3.1.2 MPI contrast agent

MPI can be used as a precise and quantitative imaging method because its signal comes directly from the magnetic moment of MNP. Small-size ferromagnetic or ferrimagnetic MNP is superparamagnetic, *i.e.*, its relatively weak magnetic moment is linearly proportional to and aligned with the direction of the applied magnetic field, showing a non-linear magnetization curve. This is the basic principle of MPI signal generation. Currently, superparamagnetic iron oxide (SPION) NPs, including Fe_3O_4 (magnetite)

and γ-Fe_2O_4 (maghemite), are used as typical MPI tracers. MNP relaxes according to Brownian (physical) and Néel (internal) rotations with an oscillating magnetic field (Figure 31) [68]. Shorter relaxation time, which depends mainly on the size and anisotropy of MNP as well as the fluidity of the medium, indicates that MNP responds more quickly to magnetization behavior in time-varying external magnetic fields, which is critical for improving the resolution and sensitivity of MPI [152, 157].

Figure 31. Illustration of the magnetic relaxation mechanisms in MNPs. Image modified from Ref. [68].

Doped transition metal ions, including manganese (Mn^{2+}), cobalt (Co^{2+}), nickel (Ni^{2+}), zinc (Zn^{2+}) and others, forming $M_xFe_{3-x}O_4$ (M refers to other metal ions), also have superparamagnetic properties comparable to those of SPIONs, which can sometimes change the magnetic and physical properties of Fe_3O_4 [59, 155, 158]. It was demonstrated that the $MnFe_2O_4$ sample had the shortest relaxation time (2.24 μs), which is superior to other samples and commercial NPs [159]. However, the preparation of these innovative MPI tracers is complex, and the introduced transition metals themselves or the organic solvents used in the preparation process may raise safety concerns. Generally, SPION is widely accessible, easy to prepare, and reasonably priced compared to other applied tracers. Additionally, SPION is non-radioactive, non-degradable over time, and exhibits excellent biosafety. Several kinds of SPION have been approved by the FDA for clinical use or are undergoing clinical trials, such as Ferumoxytol, Resovist, and Ferucarbotran, which are by far the best choice of MPI tracers [46, 160].

3.1.3 Cancer cell membrane-coated SPIO for glioma-targeting diagnosis

Previous studies have proposed different MPI applications, including cardiovascular, cerebral ischemia, and pulmonary imaging [61, 153, 154]. However, thus far there has been no specific targeting ligand to functionalize MPI nanoprobes for *in vivo* glioma applications. To improve the performance of MPI for precise diagnosis of brain tumors, biomimetic materials become the prior choice due to their intrinsically immense advantages [161]. Cancer cell membranes (CCM) derived from the organism have special biological functions, such as long-term circulation and immune regulation. CCM-functionalized nanoprobes are born with outstanding biocompatibility and show less clearance by the immune system [126]. Moreover, conventional nanomaterials cannot effectively penetrate the tumor through the enhanced permeability and retention (EPR) effect alone due to the heterogeneity and unique BBB of glioma [162]. Cell membranes are characterized by the fluidity of the lipid bilayer and transmembrane proteins that encourage non-selective NPs to cross the BBB, the primary barrier in brain applications. In particular, surface antigens expressed by CCM have domains that bind to homologous cells, which further enhances the interaction and targeting ability with the source cells, and endows NPs coated with CCM with tumor-targeting properties[163].

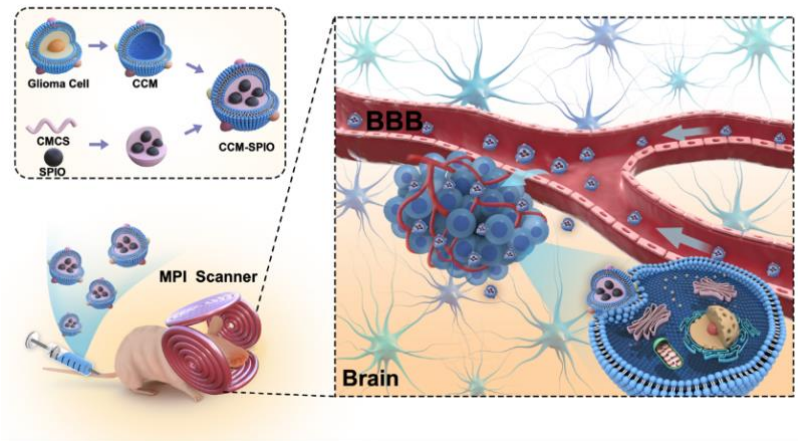

Figure 32. Schematic illustration of the synthetic and functional process of CCM-SPIO.

In this chapter, we extract the membrane of glioblastoma cells and cover it on the surface of SPIO by extrusion to prepare a nanoprobe (CCM-SPIO) that can break

through the BBB and subsequently target brain glioma (Figure 32). This nanoprobe possesses superior magnetic and photothermal effects and can be used for early and precise detection and intervention of GBM. The size of CCM-SPIO is designed to be around 90 nm, which is considered most conducive to enter the glioma [164]. *In vivo* and *in vitro* tests have shown that it can pass the BBB and has the ability to target glioblastoma. MPI and fluorescence imaging were used to accurately image mice infected with glioma and to study the *in vivo* behavior of the nanoprobe. In addition, the enhanced immune response provided by the CCM and the preeminent photothermal effect provided by the SPIO core make the nanoprobe a promising therapeutic agent. Furtherly, satisfactory photothermal therapy (PTT) effect on mouse glioma models is demonstrated and elevated immune response in the therapeutic groups is revealed. It is collectively implied that the emerging MPI technique equipped with the proposed biomimetic BBB-breaking nanoplatform can provide new insights and pathways to the noninvasive diagnosis and targeted treatment of *in situ* early-stage GBM.

3.2 Methodology

3.2.1 Synthesis and characterization of CCM-SPIO

CCM vesicles were extracted using the Membrane and Cytosol Protein Extraction Kit (Beyotime P0033). Briefly, the adherent cells were washed with PBS, scraped off with a cell scraper, and blown down with a pipette. The cells were collected by centrifugation (1000 rpm, 3 mins), then the supernatant was removed, and the cell precipitate was left for later use. After the collected cells were washed with cold PBS, they were fully suspended in membrane protein extraction reagent A with 1% PMSF. Then, the suspended cells were transferred into the glass homogenizer for 60-time homogenization after being pre-cooled in an ice bath for 15 mins. The supernatant was collected under centrifugation at 700 g (4°C, 10 mins), and the cell membrane fragments were precipitated under centrifugation at 14000 g (4°C, 30 mins). The collected CCM was suspended in PBS and sonicated in a glass bottle for 10 mins using

a bath sonicator (Fisher Scientific, Waltham, MA, USA) at 42 kHz and a power of 100 W under 4°C. The resultant CCM vesicles were subsequently extruded in sequence through polycarbonate porous membranes using an Avanti mini extruder (Avanti Polar Lipids, Alabaster, AL, USA). We then mixed the prepared CCM vesicles and SPIO solution (VivoTrax, Magnetic Insight, Inc., Alameda, CA, USA) at a surface ratio of 1:1 (S_{CCM}/S_{SPIOs}), following the surface area analysis [165]. The mixture was then extruded sequentially through 200-nm and 100-nm polycarbonate porous membranes using an Avanti mini extruder.

The resultant CCM-SPIO were then re-dispersed for further characterization by transmission electron microscopy (TEM), dynamic light scattering (DLS), zeta potential determination, and ultraviolet-visible (UV-VIS) spectroscopy. The morphology of CCM-SPIO was characterized by TEM using a FEI Tecnai F20 microscope (FEI, USA) with a 300 kV acceleration voltage. Zeta potential and size were analyzed with a ZEM 3600 Malvern Zetasizer (Malvern, UK). After that, sodium dodecyl sulfate-polyacrylamide gel electrophoresis (SDS-PAGE) was utilized to characterize membrane proteins. Optical absorption spectra were measured using a UV-VIS-NIR spectrophotometer (Shimadzu, Kyoto, Japan).

3.2.2 Cell culture and animal model

GL261, LO2, b.End.3, and HUVEC cells were cultured separately in DMEM supplemented with 10% (v/v) FBS and 1% penicillin-streptomycin solution under a 5% CO_2 atmosphere and at 37°C. For animal models, male BALB/c nude mice and male C57/6N mice were purchased from Charles River (Beijing, China). Male BALB/c nude mice were used for MPI, MRI, and fluorescence imaging, and male C57/6N mice were used for *in vivo* antitumor tests. For male C57/6N mice, GL261 cells (2×10^5 cmL^{-1}) in about 50 μL PBS were subcutaneously injected into the hind leg positions of the mice to set up the tumor model. All animal procedures were carried out according to the

guidelines approved by the Animal Ethics Committee of the Chinese Academy of Sciences.

3.2.3 Cytotoxicity assay

The cytotoxicity of the nanoprobes was tested on GL261 and LO2 cells. Cells were seeded at a density of 1×10^4/well in 96-well cell culture plates and incubated at 37°C under a 5% CO_2 atmosphere for 24 h. Then, cells were treated with various concentrations (0, 2.5, 5, 10, 20, 40, and 60 μg/mL) of CCM-SPIO (100 μL/well) for 24 h. Finally, 100 μL/well of CCK-8/culture medium (10 μL/100 μL) was supplemented in each well, and the plates were incubated for an additional 1 h under the same conditions. A Synergy HT microplate reader (BioTek, Winooski, VT, USA) was used to measure the absorbance of each well at 450 nm (OD 450). The following formula was used to calculate cell viability: Cell Viability (%) = [(As-Ab)/(Ac- Ab)] × 100%, where As, Ac, and Ab represent the OD 450 of the treatment group, control group, and blank, respectively.

3.2.4 Stability test of CCM-SPIO

The stability of CCM-SPIO was tested with the UV-VIS-NIR spectrophotometer by monitoring the change in optical absorption spectra. CCM-SPIO was dissolved in PBS, DMEM, and FBS, respectively, and stored at room temperature. To this end, the optical absorption spectra were recorded every 12 h for 3 days.

3.2.5 Photothermal performance assay

Continuous 785-nm NIR laser illumination with a spot size of 5 mm was used to test the photothermal effect. The power density was 0.5/0.8 W/cm^2. Before irradiation, the samples were dissolved in deionized water to achieve Fe concentrations of 0, 5, 10, 20, 30, and 40 μg/mL, respectively. Then, 100 μL of each sample was used for photothermal measurements. The temperature variations of all samples were recorded

using a FLUKE Ti25 infrared thermal imaging camera (Everett, WA, USA) at 30-second intervals with an accuracy of 0.1°C. For optical stability detection, 20 and 40 μg/mL Fe concentrations in CCM-SPIO solutions were analyzed at 5-min intervals by fits and starts using the same laser conditions stated above. All experiments were conducted in triplicate.

3.2.6 *In vitro* PTT assay

We used calcein-AM and PI staining to visually test the photothermal effect of CCM-SPIO. GL261 cells were cultured in 6-well plates at 37°C under a 5% CO_2 atmosphere for 24 h. The original medium was washed off, followed by adding a medium containing 10 μg/mL or 20 μg/mL Fe in CCM-SPIO, whereas the medium without nanoprobes was used as a control. After 4 h of continuous incubation, the cells were irradiated with a 785-nm laser (1 W/cm^2) for 5 mins in an already outlined area. Afterward, the cells were washed gently twice with 1× Assay buffer, followed by the addition of Calcein-AM and PI were added. The cells were incubated for another 15 mins and visualized by an inverted Leica M205 FA fluorescence microscope (Leica, Jena, Germany).

For quantitative analysis, GL261 cells were seeded at a density of 1×10^4/well in a 96-well plate at 37°C under a 5% CO2 atmosphere for 24 h. Then, the cells were randomly divided into four groups: control group, CCM-SPIO group, laser group, and CCM-SPIO with laser group. In the control group, the cells were replaced with a new routine culture medium as stated before. In the CCM-SPIO group and CCM-SPIO with laser group, the cells were treated with various concentrations (5, 10, 20, 30, and 40 μg/mL of iron) of CCM-SPIO for 4 h. Subsequently, cells in the CCM-SPIO with laser group were washed three times with PBS and then exposed to 785-nm laser illumination at 1 W/cm^2 for 3 mins. The same laser treatment procedure was also applied to the laser group but in the absence of CCM-SPIO. After that, CCK-8 was used as discussed earlier.

3.2.7 *In vitro* BBB model assay

HUVEC/b.End.3 cells (1.0×10^5 cells/well) were seeded in the 12-well transwell plate with a membrane with a mean pore size of 0.4 μm to simulate the BBB environment (Figure 33). The transendothelial electrical resistance (TEER) values were recorded by the Millicell ERS -2 Epithelial Volt-Ohm Meter volt-ohmmeter (Millipore, USA) to assess the cell monolayer integrity during cell culture. When the TEER value reaches 200 Ω cm^2 or above, it can be considered as an *in vitro* BBB model. Next, the fresh DMEM with uncoated SPIO/CCM-SPIO was replaced in the cells. Afterward, the medium in both apical and basolateral chambers was collected for ICP assays after another 6 h of incubation.

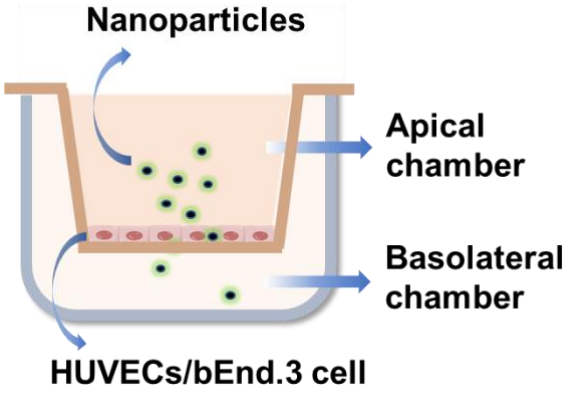

Figure 33. Schematic of the *in vitro* transwell model.

3.2.8 *In vitro* targeting studies

To verify that CCM could enhance the tumor-targeting ability of SPIO, glioma cells were co-cultured with CCM-SPIO and SPIO for 6 h separately. After washing with PBS, the cells were collected for MPI signaling test and biological electron microscopy. To further evaluate the targeting effect of CCM-SPIO, four different kinds of tumor cells, including breast cancer cell (4T1), glioblastoma cell (GL261), pancreatic cancer cell (Panc02), and gastric carcinoma cell (SGC-7901), were incubated overnight and co-incubated with CCM-SPIO for another 6 h. In the end, the cells were collected to test the MPI signals and ICP after being washed with PBS twice. On the other hand,

GL261 cells were co-incubated with ICG/CCM- SPIO-ICG for 6 h for confocal imaging assessment. After that, the cells were stained with Hoechst 33258 and imaged by confocal laser scanning microscopy (CLSM, Dragonfly 200, Andor, Shenzhen, China).

The cells were co-incubated with uncoated SPIO/CCM-SPIO for biological scanning electron microscopy. Following the incubation, DMEM was poured off from the dish without rinsing. The cells were immediately covered with electron microscope fixative and collected into a centrifuge tube by gently scraping them off the dish. After further addition of electron microscope fixative, the cells were fixed for 2 h at room temperature and then transferred to a 4 °C refrigerator to be ready for subsequent experiments.

3.2.9 *In vitro* and *in vivo* MPI

MPI was completed by an MPI scanner (MOMENTUM Imager, Magnetic Insight Inc.) with a frequency of 45 kHz and a magnetic gradient strength of 6 T/m. The scan mode is set as isotropic; Z field of view: 4 cm for measuring EP tubes, 5 cm for measuring chicken breast, 3 cm for measuring mouse head, and 12 cm for measuring the mouse whole body. Data analysis was performed using VivoQuant software (VivoQuant 4.0, Invicro, Boston, MA, USA). For the demonstration of penetration depth, the nanoprobe was tested in the capillary settled under the chicken at varying depths (1, 2, 3, 4, 5, 6 cm) using MPI.

3.2.10 Biodistribution Analysis

Pilot biodistribution images were taken using the In Vivo Imaging System (IVIS® SpectrumCT; PerkinElmer, Waltham, MA, USA) before and 1, 3, 6, 8, 10, 12, and 24 h after injection of 200 μL CCM-SPIO-ICG (2 mg/mL) into the glioma-bearing mice to monitor the biodistribution of the nanoprobe *in vivo*. After 72 h, the mice were

necropsied; their organs and tumors were then used to study metabolic pathways by measuring the fluorescence intensity.

3.2.11 *In vivo* photothermal therapy

Twenty-four liver tumor-bearing mice were prepared as described earlier. When the tumor volume reached about 10 mm^3, the mice were randomly divided into four evenly numbered groups: control group, CCM-SPIO group, laser group, and CCM-SPIO with laser group. In the control group, the healthy mice received no treatment. In the laser group, the tumor-bearing mice were irradiated with a 785-nm laser (2 W/cm^2) for 5 mins. In the other two groups, tumor-bearing mice received 200 μL of CCM-SPIO (2 mg/mL) intravenously, but only the mice in the CCM-SPIO with laser group were also irradiated with a 785-nm laser (2 W/cm^2) for 5 mins at 48 h post-injection. The temperature elevation of tumors was recorded with an infrared thermal imaging camera during photothermal treatment. The body weight of each mouse from all groups was measured every other day. Tumor volume calculation formula: $V = Length \times (Width)^2/2$. The mice were dissected after death, with tumors and major organs, including heart, liver, spleen, lung, and kidney, being harvested, fixed with 4% paraformaldehyde, sectioned into slices, and stained with H&E for histological analysis.

3.2.12 Immune Response Assay

When mice were sacrificed at 14 days after CCM-SPIO-guided PTT, the tumor, spleen, and inguinal lymph in the groups were collected and used for flow cytometry analysis of immune cells. To each sample tube with 100 μL of cell suspension (10^7 cells/mL), 1 μg of anti-mouse CD16/32 (TruStain FcX™) was added, mixed, and incubated for 10 minutes at room temperature. Fluorescence-labeled antibodies were added to the cell suspension according to the combination (CD45 BB515 / CD3 PE / CD4 APC / CD8 PE -Cy5) and incubated for 20 minutes at room temperature in a dark place. 2 mL of PBS containing 1% FBS was added to each sample tube. The mixtures were centrifuged

at 500 g for 5 mins to remove the supernatant. Then, 0.5 mL of PBS containing 1% FBS was added, and analytical data were acquired on a Cytek NL -CLC3000 flow cytometer (Thermofisher, USA).

3.2.13 Statistical Analysis

GraphPad Prism 8 software (GraphPad Software, San Diego, CA, USA) was used for statistical analysis. A t-test was performed to determine the differences among different groups. *$p < 0.05$, **$p < 0.01$, ***$p < 0.001$, and ***$p < 0.0001$ were considered statistically significant, whereas n.s. indicated no significant difference between the two selected groups.

3.3 Results

3.3.1 Characterize of CCM-SPIO

We tested the morphology, protein separation, hydrodynamic size, surface zeta potential, and absorption spectrum using TEM, SDS-PAGE, DLS, and UV-VIS-NIR, respectively, to characterize the synthesized nanoprobe. TEM observations display that CCM-SPIO (Figure 34A, B) represents a distinctive core shell indicating bilayer membrane structures. The unique biometric characteristics of CCM-SPIO are verified by SDS-PAGE. The total protein extracted from CCM-SPIO was identical to the complete protein in the original GL261 cell membrane (Figure 34C), suggesting that the biomimetic nanoprobe ultimately inherited the protein characteristics of the original cell and provided the basis for the *in vivo* targeting effect. The hydrodynamic size of CCM-SPIO was approximately 87.4 nm, which increased by 18.2 nm to the SPIO core (69.2 nm) (Figure 34D). The result consists of the thickness of cell lipid bilayer membranes, which is well-known to be 5-10 nm thick [166]. Small NPs of this size facilitate the EPR effect to penetrate the blood-brain tumor barrier to enhance passive aggregation in GBM tumors [162, 167]. Additionally, it has been reported that NPs larger than 100 nm in size can be occluded because glioblastoma cells have

characteristic pore cutoff sizes ranging from 7 to 100 nm [164]. The optical absorption spectrum of CCM-SPIO is exhibited in Figure34E, which presents a smooth absorption from 700 to 1000 nm, making it suitable for near infrared (NIR) optical therapy at depths.

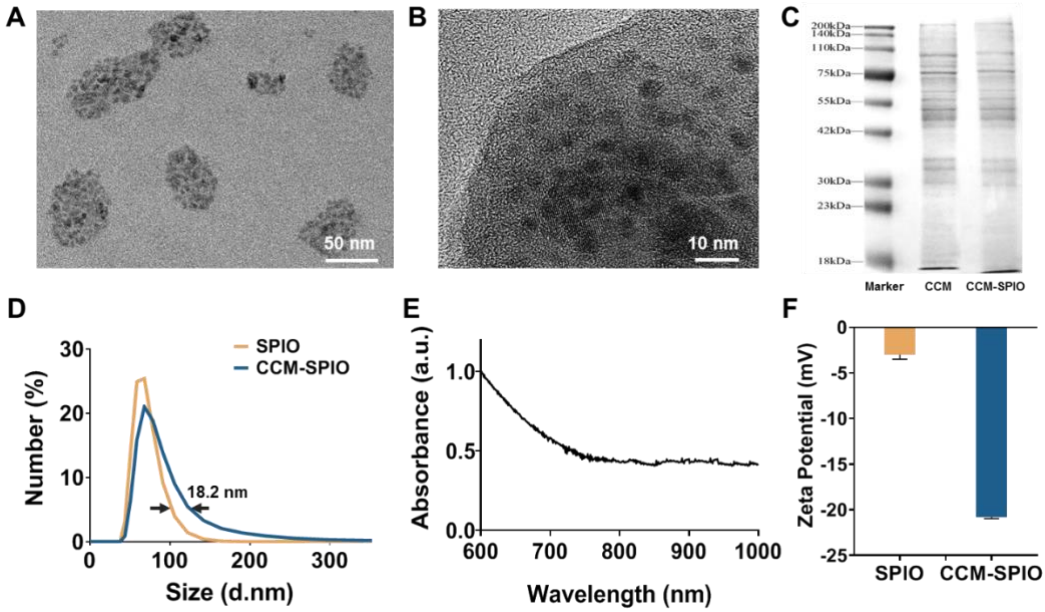

Figure 34. Characterization of the CCM-SPIO nanospheres. (A, B) TEM image of CCM-SPIO. (C) SDS-PAGE protein analysis results of cancer cell membrane vesicles, and CCM-SPIO. (D) DLS results of CCM-SPIO nanoprobes. (E) UV–Vis-NIR spectra of CCM-SPIO suspensions. (F) Zeta-potential of SPIO and CCM-SPIO nanoprobes (n = 3).

The stability of CCM-SPIO was tested by monitoring the change in optical absorption spectra of the solution with PBS/FBS/DMEM. From figure 35 we can see that the absorption spectra of the three solutions mentioned above were almost identical from different measurements, attesting to a stable structure of CCM-SPIO in PBS/FBS/DMEM. The outcome implies that CCM-SPIO can maintain effectiveness and performance in vivo. The zeta potential of the CCM-SPIO changed from - 3.0 to -20.8 mV after camouflaging (Figure 34F); the latter was similar to the surface charge of the cell membrane [168]. Such a change in zeta potential makes the magnetic

particles more biocompatible and more suitable for *in vivo* applications [169]. Characterization analysis showed that CCM-SPIO was successfully synthesized and retained the protein characteristics of the cell membrane.

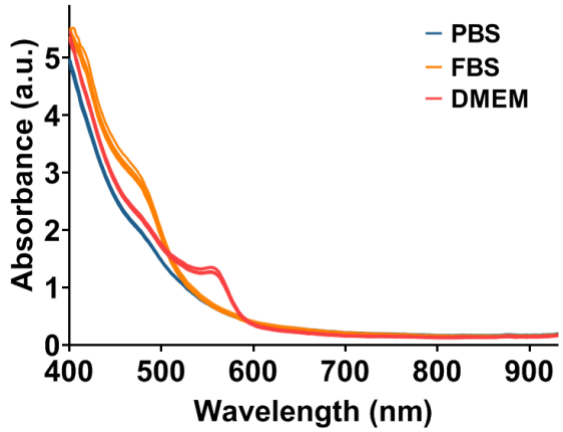

Figure 35: UV–Vis-NIR spectra of CCM-SPIO dissolved in the PBS/FBS/DMEM stored under room temperature for 3 days of testing. Each panel contained 6 sets of data at different time points.

3.3.2 BBB Breaking-Through and Homogenous Targeting of CCM-SPIO

To evaluate whether the CCM coating could enhance the nanoprobe to get through the BBB, which is a major biological barrier that prevents NPs from targeting and accumulating in gliomas, we successfully simulated an *in vitro* BBB model using bEnd.3/HUVEC cells as illustrated in Figure 36A. The results showed that the nanoprobe could more easily break through the tightly connected vascular endothelial cells after being coated with CCM (36.5% ±2.5 versus 21% ±2.0 at 8 h, *P=0.0401), indicating that CCM-SPIO can better penetrate the BBB (Figure 36B). In addition to BBB penetration, modification of CCM is expected to render a nanocarrier with tumor-targeted ability since the homogenous aggregation property of cancer cells. To demonstrate this, we compared the amount of SPIO and CCM-SPIO taken up by glioma cells *in vitro*. The MPI signal of the glioma cells co-cultured with CCM-SPIO is much higher than that of SPIO (5.286 ± 0.665 versus 2.623 ± 0.722, **p = 0.0093, Figure 36C), suggesting that CCM cloaking may promote nanoprobe accumulation in the tumor. In addition, biological electron microscopy also intuitively showed that much

more CCM-SPIO was phagocytized by the glioma cell than naked SPIO (Figure 36D, E), which further supports the improved tumor targeting by CCM cloaking.

Subsequently, four different kinds of tumor cells (4T1, GL261, Panc02, and SGC-7901) were incubated with CCM-SPIO separately to verify that NPs derived from tumor cell membrane modifications can promote uptake by homologous cells and improve targeting properties. It should be specified here the membrane source of CCM-SPIO was extracted from GL261 cells, so the nanoprobe is expected to target the GL261 cells. Detailed experimental procedures are presented in the Methodology section. After removing the supernatant, the cells were digested, collected, and tested for MPI signal. It can be seen from the results that the signal of MNPs in glioma cells is the strongest (Figure 36F). Consistent results were obtained by ICP quantification of Fe content in the cell precipitates (Figure 36G). The Fe content in glioma cells was significantly different from that in the other three groups (***$P < 0.001$). These indicate that the modified SPIO has a considerably improved targeting ability to target protein-derived glioma cells but has no binding ability to other types of tumor cells, that is, specificity. We also studied the fortified targeting ability with CLSM by ICG-marked CCM-SPIO. As expected, CLSM images showed stronger signals from the ICG channel in the CCM-SPIO-ICG group, indicating that the nanoprobe was effectively internalized into the glioma cells (Figure 36H). The mean fluorescent intensity between the two groups was statistically significant, further illustrating that much more ICG was attached to the tumor cells after being wrapped with CCM (**$P = 0.0041$, Figure 36I). These experiments revealed the feasibility of a tumor cell membrane encapsulation scheme to improve the tumor-specific targeting of NPs.

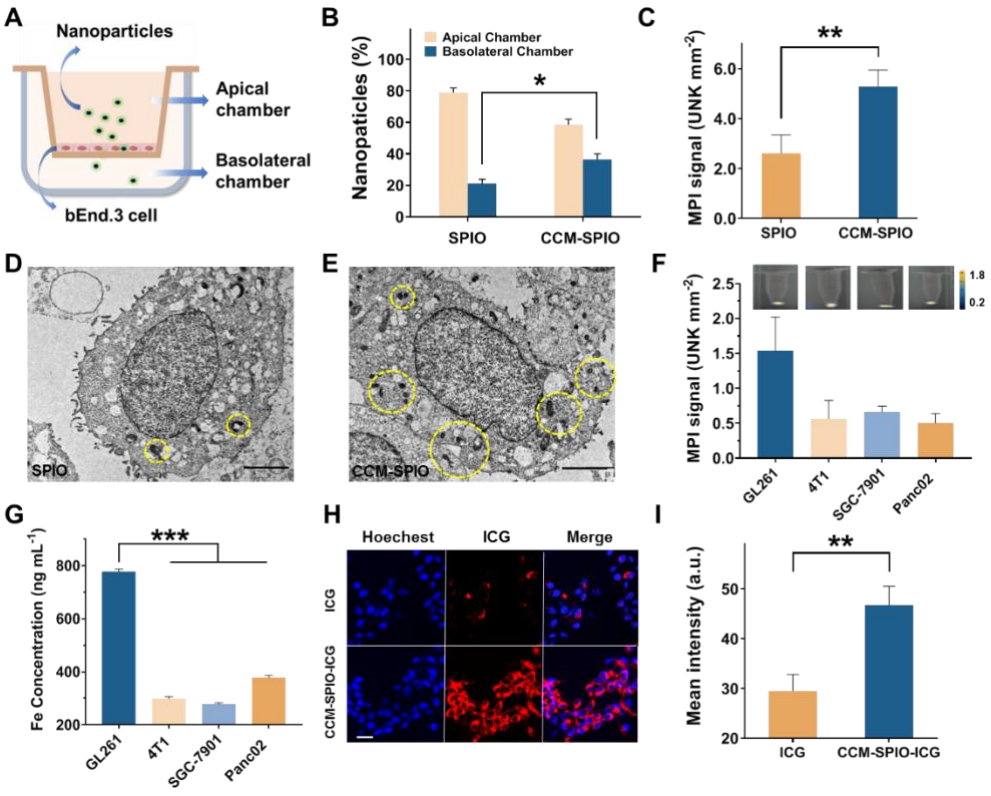

Figure 36. (A) Schematic of the *in vitro* transwell model (B) Transcytosis efficiency of various formulations in the BBB model measured by ICP. (C) MPI quantitative analysis of glioma cells treated with SPIO and CCM-SPIO. (D, E) TEM images of glioma cells treated with SPIO and CCM-SPIO. (F) MPI images and quantitative analysis of 4 different tumor cells after co-incubation with CCM-SPIO. (G) Quantitative Fe analysis of cells in (F) by ICP. (H) CLSM images of glioma cells treated with ICG and CCM-SPIO-ICG nanoprobes, respectively (the blue indicates nucleus stained with Hoechst, the red indicates ICG) (I) Quantitative analysis of CLSM images in (H).

3.3.3 Penetration depth and sensitivity demonstration of MPI

As an emerging imaging technique, MPI is considered to have exceptional sensitivity and penetrating properties in tissue. Hence, we first tested the MPI performance of CCM-SPIO *in vitro* to verify MPI's detection limit. As shown in Figure 37A, the MPI signal of the nanoprobes increased approximately linearly with the iron concentration in the probe. With such a linear relationship, the nanoprobes in the ROI can be quantitatively analyzed according to the MPI signal intensity. Pellets with increasing

numbers of CCM-SPIO-loaded glioma cells were examined to determine the minimum number of cells that could be detected by MPI. Overall, the MPI signal decreased significantly with decreasing cell number, indicating that MPI could distinguish different numbers of tumor cells labeled with CCM-SPIO (Figure 37B). It can be seen from the results that the MPI signal of 5×10^3 tumor cells co-incubated with CCM-SPIO was significantly different from that of an equal number of uninfected cells (5.333 ± 1.528 versus 0.133 ± 0.351, **P = 0.0045). The pellet containing 5×10^4 tumor cells labeled with CCM-SPIO was clearly distinguished from that containing 5×10^3 cells (12.667 ± 1.528 versus 5.333 ± 1.528, **P = 0.0042). Due to the inevitable background noise from the MPI scanner and the difference of the probe phagocytosis in cells, the smallest amount of CCM-SPIO-labeled tumor cells that can be detected by MPI in our study is 5×10^3, which is one quarter of the detection limit of 2×10^4 cells reported in literature for MRI [170]. This proves the supreme sensitivity of MPI assisted by CCM-SPIO, which is essential to assure the detection of early primary tumors.

The other important feature to enable diagnosis of early glioblastoma *in vivo* is the tissue penetration capability of the imaging modality. To demonstrate that of MPI, we chose fluorescence imaging (FI), one of the most popularly used imaging modalities in the field, as the reference. As known, FI can sensitively detect signals from biological tissues, which, however, is limited to shallow depth of a few millimeters beneath tissue surface and hence encounters insufficiency in large animals or humans. In Figure 37C, we compared the influence of tissue sample thickness to *in vivo* MPI (the top panel) and fluorescence imaging (the inset panel, with ICG loaded onto the CCM-SPIO probes) on glioma-bearing mice, by examining the changes of signal from samples covered by chicken breast tissue of varying thickness (0 - 6 cm). As expected, the MPI signal remained nearly constant with increased sample thickness, whereas the intensity of FI dropped rapidly to ~20% when the sample thickness was 1 cm and almost to zero when the thickness was increased to 2 cm. Additionally, the mouse tumor model labeled with

CCM-SPIO was investigated by placing the animal model at several positions consisting of different tissue depths for the tumor site. As seen (Figure 37D), there is no significant variations among the MPI signals with different tissue depths. These results in combination demonstrate the immunity of MPI to sample thickness and positioning, which is equally, if not more than, important to assure MPI for deep tissue applications.

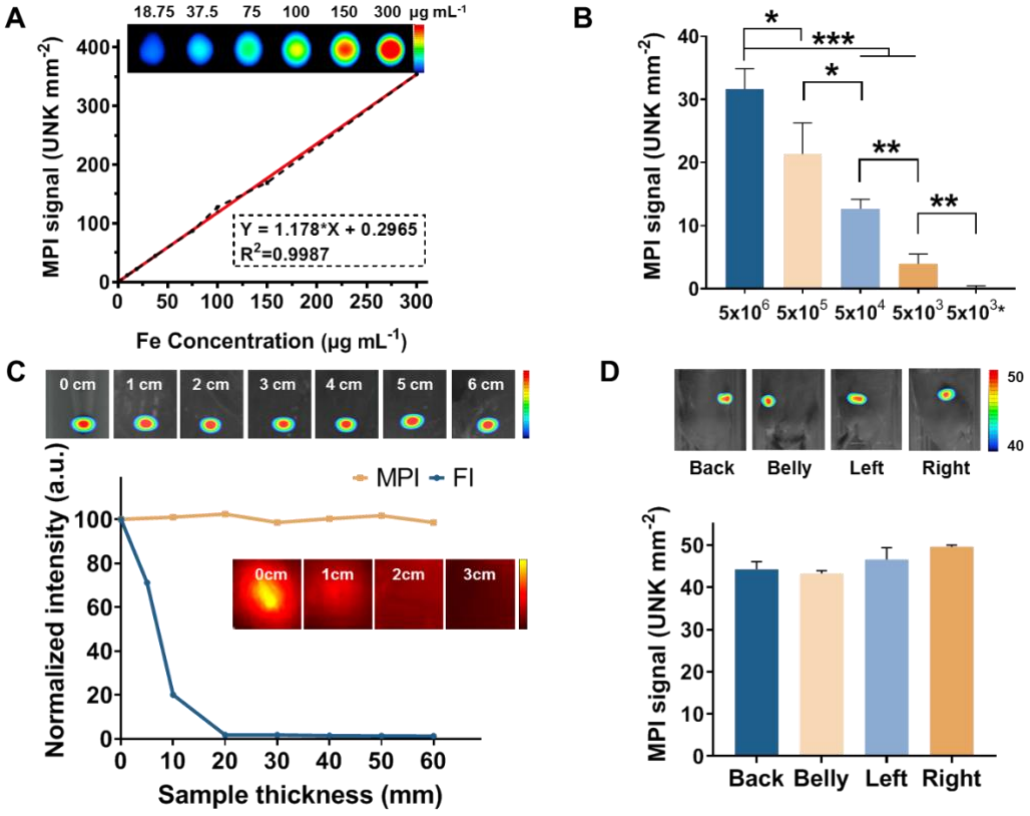

Figure 37. MPI sensitivity and penetration testing with CCM-SPIO. (A) *In vitro* MPI images of CCM-SPIO at different Iron concentrations (0, 25, 50, 100, 150 and 200 μg/mL). (B) MPI signals of variety amount of GL261 cells post co-incubate with CCM-SPIO. The last group 5×10^3* means cells without nanoprobe. (C) Intensity changes of MPI and fluorescence imaging with gradually increased thickness of chicken breast overlaid on the nanoprobes. (D) MPI images of mouse subcutaneous glioma models at different positions. The error bars represent standard deviation from measurements with n = 3.

3.3.4 Multimodality Imaging of Glioma Allografts in Mice

To further evaluate the deep-tissue tumor imaging capability of CCM-SPIO, mouse orthotopic glioblastoma tumor model was injected with CCM-SPIO. Initially, the fluorescence images demonstrated the bio-distribution of ICG-marked CCM-SPIO, which rapidly distributed throughout the body with the blood flow after intravenous injection and was subsequently excreted (Figure 38A, 39). It was observed to be fully distributed in the brain within an hour, and the signals of tumor areas gradually increased over time from 1 to 8 h post-administration, indicating that the ICG-loaded CCM-SPIO was efficiently delivered into the tumor. The *ex vivo* brain at 8 h confirmed that the ICG-marked CCM-SPIO was efficiently delivered into the tumor (Figure 39). Because of the relatively shallow penetration depth required in small animals, the nanoprobe can also be detected by fluorescence imaging and be observed to reach the brain glioma sites. The average radiant efficiency of ROI also displayed that the signal rapidly reached a maximum value at 1 h, then dramatically declined, and gradually reached another peak at 8 h, indicating that the nanoprobes accumulated at the tumor site by targeting effect (Figure 38B). Correspondingly, dynamic MPI visualized the gradual accumulation of CCM-SPIO in tumor areas from 1 to 8 h after the intravenous injection, as illustrated in the 2D MPI images in Figure 38D. As a comparison, a relatively weak MPI signal was observed in the tumor sites at the captioned time after the injection of SPIO (Figure 38C). At the 24 hour, the signal from SPIO in the brain had almost disappeared, while the signal from CCM-SPIO remained (Figure 38E), suggesting that CCM enhanced the ability of the nanoprobe to penetrate the BBB and the target glioma. It is also possible that the increased exposure of polyethylene glycol (PEG)-SPIO to reticuloendothelial system could accelerate its clearance; by contrast, biofilm modification could more wittily evade the clearance by the immune system and prolong the circulation time in the body.

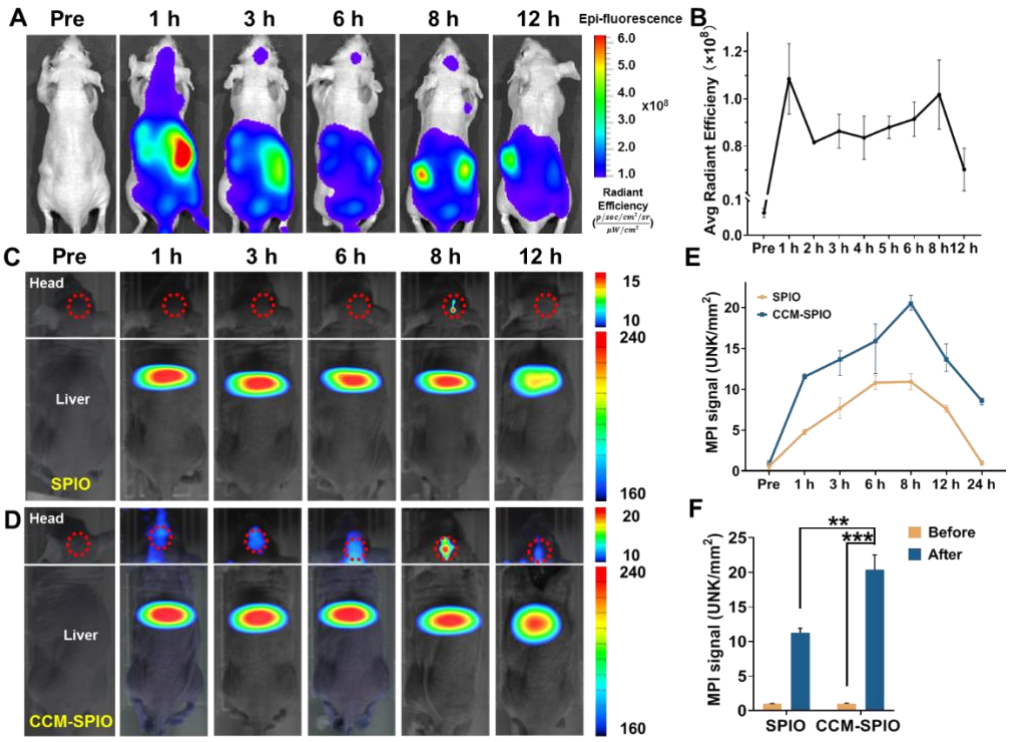

Figure 38. Multimodal imaging of orthotopic brain tumor xenografts in Mice. (A) Fluorescence images of GL261 tumor-bearing mice at different time points (pre-injection, 1, 3, 6, 8, and 12 h), and (B) the corresponding fluorescence intensities at the brain tumor site (n = 3). 2D MPI images of mouse head with orthotopic brain tumor after injection of SPIO (C) and CCM-SPIO (D), respectively. The dashed red circles represent the ROI. (E) The corresponding quantified analysis of brain MPI signal at different time points. (F) Brain MPI signal intensities before and 8 h post the injection of SPIO and CCM-SPIO, respectively.

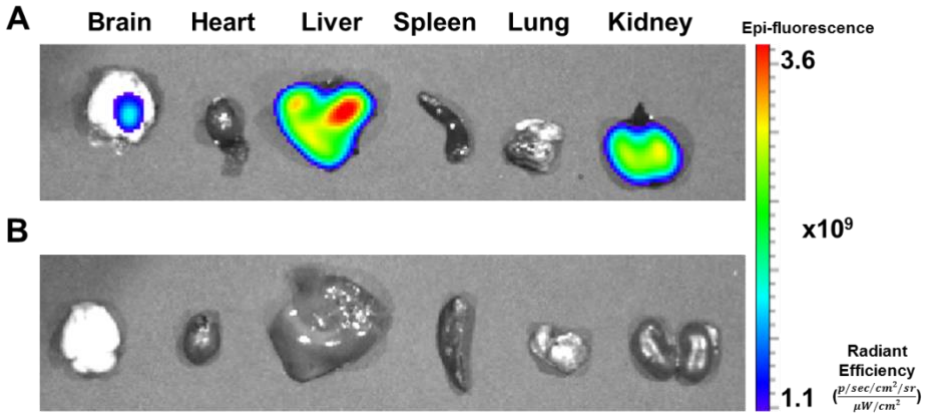

Figure 39. *Ex vivo* fluorescent imaging of mouse organs at 8 h (A) and 24 h (B) after ICG-loaded CCM-SPIO injection.

Quantification analysis showed a 20.6-fold increase in MPI signals from the marked tumor regions after CCM-SPIO injection (20.341 ± 2.187 versus 0.986 ± 0.043 at 8 h post the injection, ****P < 0.0001), which is 1.8-fold increase compared to that with SPIO injection (20.341 ± 2.187 versus 11.256 ± 0.662 at 8 h post the injection, **P = 0.0023, Figure 38F). It suggests that after coating, the nanoprobes could reach the mice's brain faster, accumulate more at the tumor site, and remained longer in the brain. This conclusion was also confirmed by *ex vivo* MPI and histopathological analysis as shown in Figure 40A. 3D CT/MPI imaging of the mouse brain was also performed (Figure 40B). With the structural information provided by CT, the location and size of the brain tumor can be clearly determined by the MPI signals from different orientations. The mice were dissected to isolate the brain after imaging. The tumors in the brain were visualized with an average diameter of 2 mm, and the maximum cross section of the tumor was 2.0 × 2.1 mm^2 in the H&E section of the brain (Figure 41). After all images were obtained, the tumor tissues from mice were dissected and analyzed by Prussian blue staining. The results (Figure 40C) showed that the blue color was more pronounced in the tumor site in the CCM-SPIO group than in the SPIO group, which could be further verified by the quantitative analysis (Figure 40D). These results indicate that CCM-SPIO is more effective than SPIO for glioma targeting.

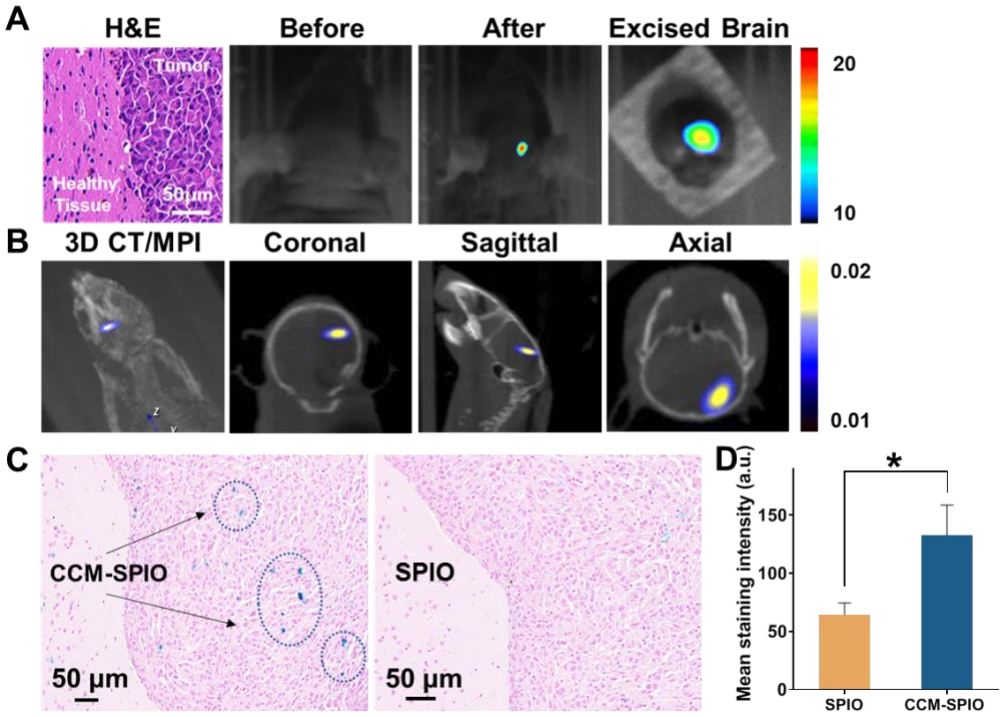

Figure 40. (A) H&E stanning and 2D MPI images of the brain from the mice injected with CCM-SPIO. (B) 3D MPI/CT images of mice head with glioma before and 8 h post the injection of CCM-SPIO. (C) Prussian blue staining of tumor sections at 8 h post the injection of CCM-SPIO. (D) The corresponding quantification of Prussian blue staining signals from the brain regions.

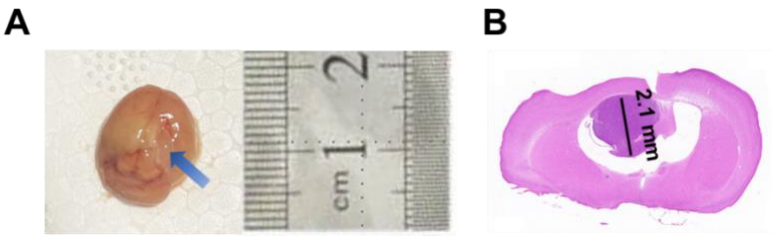

Figure 41. *Ex vivo* mouse brain tissue and the H&E slice of the maximum cross-section.

3.3.5 Cell Viability Test on CCM-SPIO

The toxicity of the synthesized nanoprobes was evaluated on the B. End.3 cells, the primary component cell of the mouse BBB, and LO2, a type of normal liver cell. The viability of both cell lines changed slightly after incubated with gradually increasing concentrations of the nanoprobe (0, 5, 10, 20, 30, and 40 μg/mL of iron), indicating that

the nanoprobe has good biocompatibility and minor toxicity (Figure 42A). The degradation process of CCM-SPIO in cells was observed by biological electron microscopy. It can be observed that the presence of dense aggregates of the CCM-SPIO inside the early and late endosomes and subsequently in the lysosomes. This is consistent with the intracellular metabolism characteristics of degradable nanomaterials which are internalized primarily through the endocytic process of vesicle formation [27]. Once inside the lysosome, the probe begins to degrade and disintegrate, as indicated by Figure 43). To evaluate the photothermal effect of the CCM-SPIO, a laser beam was directed to the neck of the EP tube containing PBS / CCM-SPIO with varying concentrations (5, 10, 20, 30, 40 μg/mL of iron), and the temperature of the nanoprobe solution was recorded every 30s (Figure 44). The temperature of the CCM-SPIO solution exhibited a sharp increase with the exposure time, implying that it has an excellent PTT ability (Figure 42B). The rate and final temperature of the solution increase with the concentration of CCM-SPIO, and only 10 μg/mL of iron exposure for 180 s can make the temperature reach almost 43 °C, which can lead to cell apoptosis (42.75 ± 0.55 °C) [171].

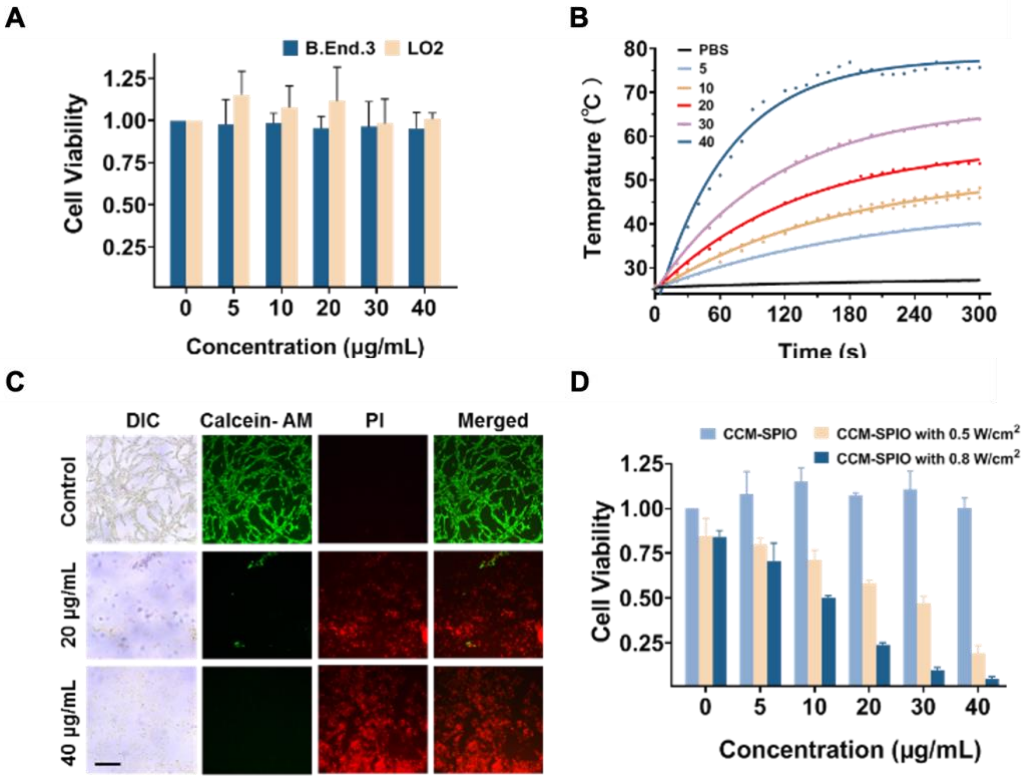

Figure 42. (A) Toxicity of different concentrations of CCM-SPIO on normal cells. (B) The photothermal temperature-time curves of CCM-SPIO at different concentrations (0, 5, 10, 20, 30 and 40 μg/mL) under 780 nm laser (0.8 W/cm^2, 5 min) irradiation. (C) CLSM images of cancer cells co-stained with CAM and PI after various treatments to distinguish the live (green fluorescence) and dead (red fluorescence) cells. (D) CCK8 results after various treatments (n = 3).

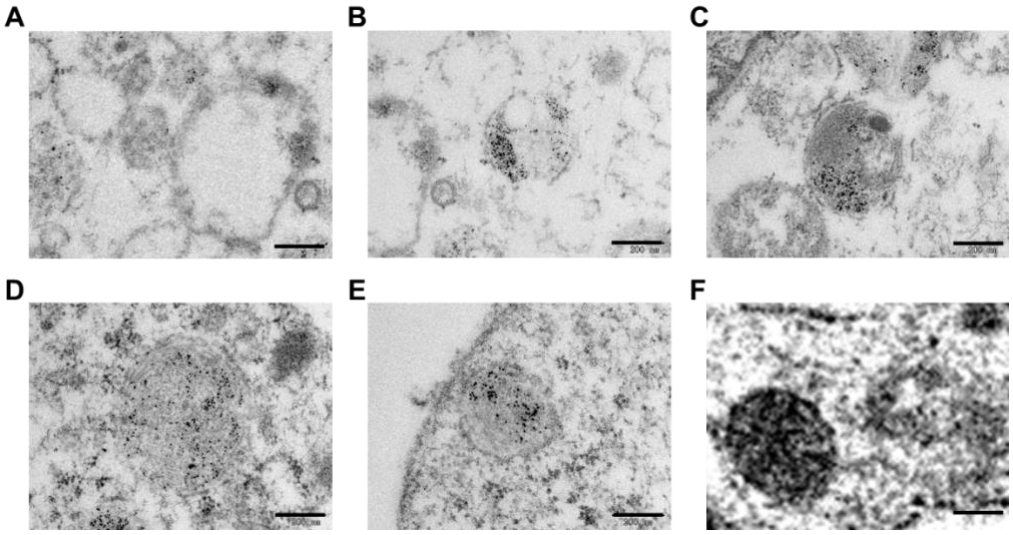

Figure 43. The cellular degradation of the CCM-SPIO at different stages was observed by TEM. A) Early endosome, B) late endosome, C-E) endo-lysosome, F) CCM-SPIO in the lysosome. Scale bar = 200 nm.

Subsequently, the photothermal capacity of the CCM-SPIO on the tumor cells was tested by calcein-AM and PI staining, which is responsible for visualizing live and dead cells, respectively. The cells incubated with the CCM-SPIO were dead after 5 mins of irradiation, while the control group showed superior viability (Figure 42C). The PI fluorescence is much stronger in the group with the higher concentration (40 μg/mL) than in the group with the lower concentration (20 μg/mL) according to the tendency of Figure 42B. The cell viability after irradiation was also evaluated by CCK-8 assay. Cell viability was significantly reduced after co-incubation with CCM-SPIO and irradiation, further demonstrating PTT's lethal effect on cells. Cell viability decreased

with the increase of concentration and irradiation intensity (0.1935 ± 0.044 at 0.5 W/cm^2, 0.0522 ± 0.012 at 0.8 W/cm^2 with 40 μg/mL concentration) (Figure 42D). The results indicate that CCM-SPIO has minimal cytotoxic effect on living cells without irradiation but could effectively eliminate tumor cells under light irradiation of 0.8 W/cm^2 for 5 mins, showing promising PTT competence.

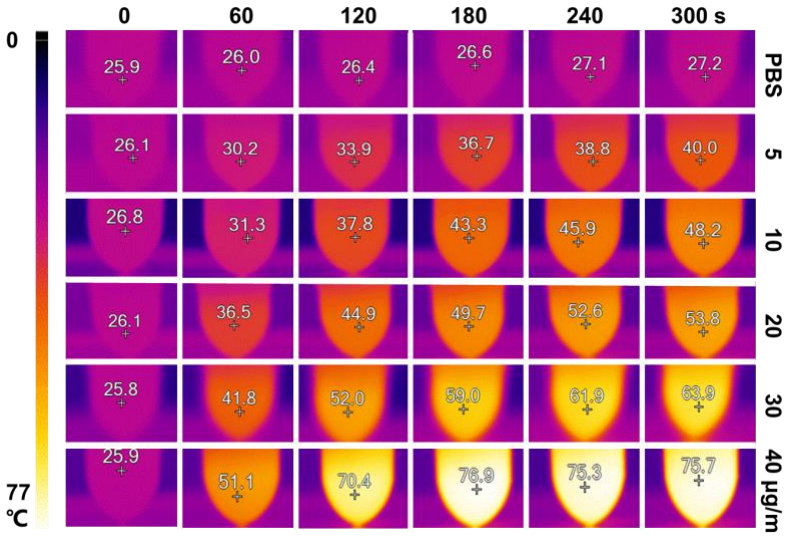

Figure 44. Temperature changes of the increasing concentration of the CCM-SPIO irradiated by 785 nm 0.6 W/cm^2 captured by infrared thermal imaging camera.

3.3.6 Anti-tumor Effect *in vivo*

We further studied the antitumor treatment efficacy of CCM-SPIO on the glioblastoma subcutaneous xenograft tumor model in C57/6N mice. The mouse body weight variation was recorded every other day for 2 weeks from the day of treatment. During monitoring, all mice behaved normally and had no significant weight loss (Figure 45A), indicating negligible toxicity of the CCM-SPIO. The mice in the treatment group gained a slight amount of weight, likely as a result of their improved health condition after tumor suppression. As shown in Figure 45B, after 785 nm irradiation (0.8 W cm^{-2}), the tumor volumes in the treatment group (CCM-SPIO + NIR) were significantly

suppressed, while the tumors in other groups showed malignant growth, demonstrating that the superior therapeutic effect of CCM-SPIO. Tumor shrinkage in the treatment group (CCM-SPIO + NIR) reached 92.0 ± 0.071%, and the antitumor effect was the best. After all monitoring studies, the tumor sites were dissected (the rightmost panel in Figure 45B) to measure their weights. The obtained average tumor weight of the treatment group (CCM-SPIO + NIR) diminished to 0.033 ± 0.058 g, which is more than one magnitude lower than that from all other groups, such as the control group (0.900 ± 0.100 g, ***p = 0.0002) and SPIO group (0.500 ± 0.100 g, **p = 0.0022, Figure 46). These results indicate that PTT with CCM-SPIO has excellent tumor therapeutic performance.

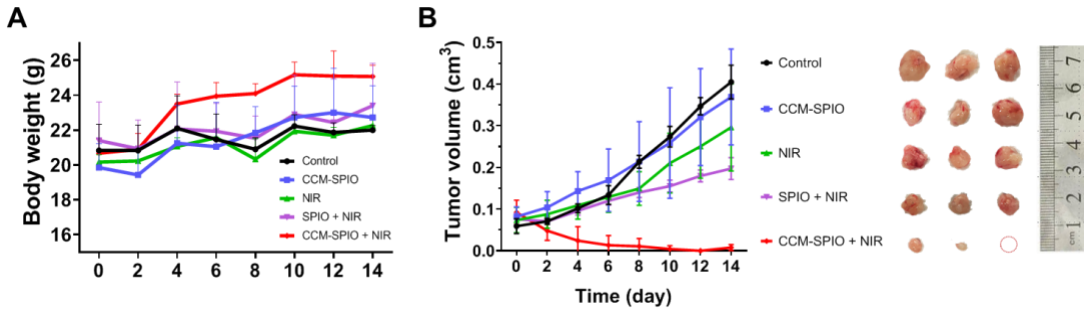

Figure 45. Anti-tumor effects of PTT based on CCM-SPIO on glioma mouse models. (A) Weight change in mice during treatment. Data are expressed as the mean ± SD (n = 4). (B) Tumor volume change and representative images of tumor in each group.

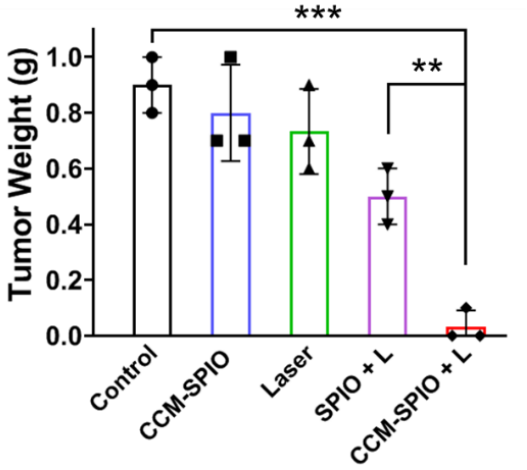

Figure 46. Quantitative analysis of the tumor weight from each group of mice.

In addition, as the CCM-modified nanoprobes were expected to induce cancer antigen immunotherapy [129, 172], spleens, inguinal lymph nodes (LNs), and tumors were dissected at 14 days after the therapy and digested into individual cell suspensions for flow cytometry analysis to measure the percentage of the cytotoxic T- lymphocytes (CTL). The results (Figure 47B, C) showed that the CTL-mediated antitumor response was elicited after treatment, as reflected by a remarkably increased percentage of CD3+CD8+T cells (*p = 0.0102). Some representative images are shown in Figure 47A. Notably, mice injected with CCM-SPIO also displayed a significantly increased percentage of CD3+CD8+T cells compared with the control group, which could be considered as evidence of immunotoxicity induced by CCM (*p = 0.0414).

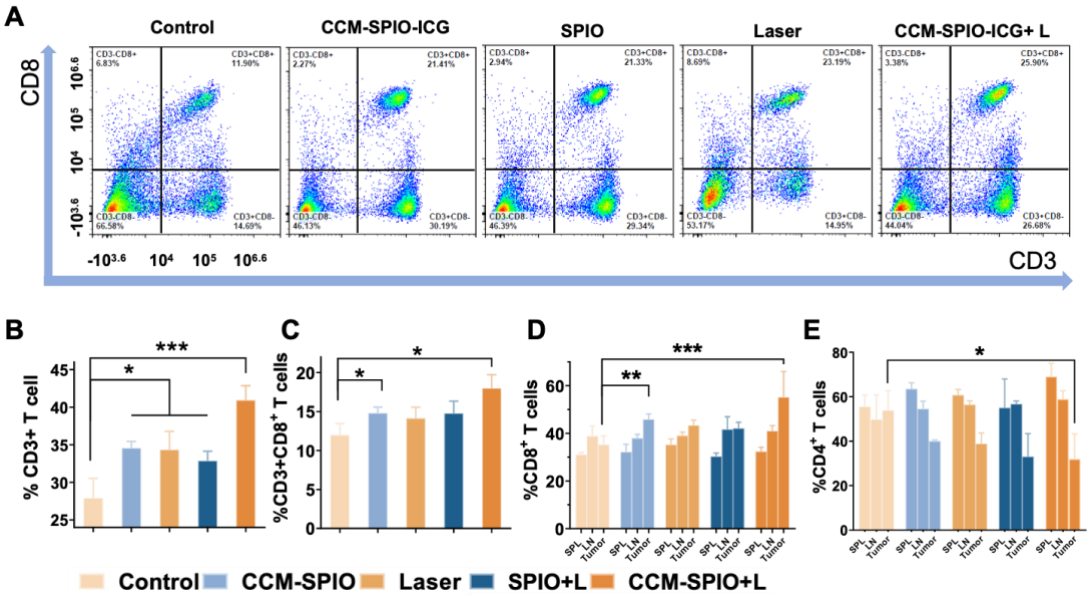

Figure 47. (A) Representative populations of CD3+CD8+ CTLs isolated from LNs at 14 days post-treatment in each group. (B, C) Percentage of CD3+and CD3+CD8+ CTLs in spleens and LNs in each group. (D, E) Percentage of CD3+CD8+/ CD3+CD4+in T cells infiltrated in the treated tumors in each group.

After observing the indication of a systemic immune response, we further profiled CTL entering the tumors. It is found (Figure 47D) that a significantly increased proportion of cytotoxic CD3+CD8+T cells infiltrated the treated tumors following PTT with CCM-SPIO compared with the other groups. A corresponding significant decrease in CD3+CD4+T cells was also analyzed in more detail, which is considered to be suppression of T-regs responsible for inhibiting the antitumor immune responses (Figure 47E). Overall, the evidence of the shifts in CD4+ and CD8+T cell populations was consistent with the hypothesis that CCM-SPIO can induce positive immunomodulation following PTT, assisting in achieving better therapeutic effects. Last but not the least, the major organs of the mice were investigated by H&E staining

at the end of the treatment to determine the biocompatibility and safety after the different groups of treatment. The results (Figure 48 displayed no apparent damage to the major organs of the mice, further confirming the low systemic toxicity *in vivo* of the synthesized CCM-SPIO nanoprobes.

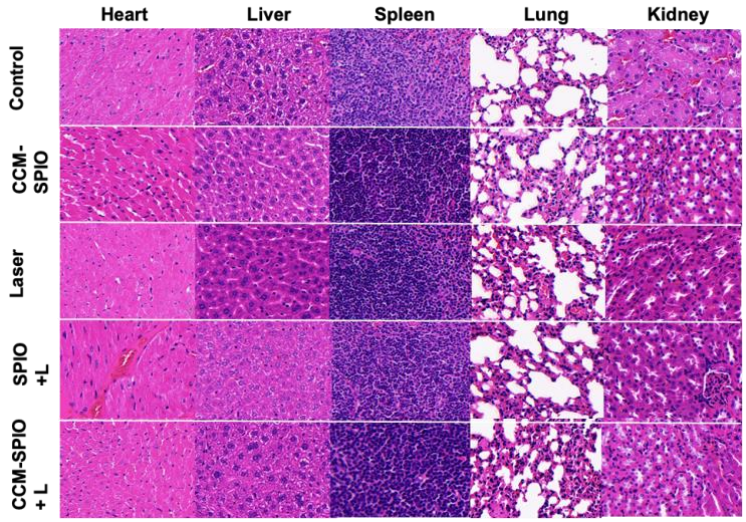

Figure 48. Representative H&E staining images of the tissues of each group.

3.4 Summary of this study

In this work, based on an enveloped bioinspired design strategy, we have developed a CCM-coated SPIO nanoprobe for sensitive and deep-penetrating MPI diagnosis and effective PTT of early glioma. The resultant formulation (CCM-SPIO) exhibited favorable BBB breaking and homologous tumor- targeting intelligence owing to the CCM coating. Compared to commercially available SPIO, the nanoprobe can more effectively cross the BBB and be encapsulated by the glioma cells, endowing noninvasive MPI with the capability to diagnose early-stage glioma. More importantly, with the assistance of the nanoprobe, the sensitivity and deep penetrating features of MPI were demonstrated. Notably, the smallest amount of CCM-SPIO-labeled tumor cells that can be detected in this study is as low as 5×10^3, which is 25% of the detection

limit with the state-of-the-art MRI and 5% of the threshold that triggers tumor angiogenesis (1×10^5) [8, 149], displaying convincing basics for the early detection of glioma. The targeting ability of the CCM-SPIO was tested by MPI on orthotopic glioma mouse models. It was found that CCM-SPIO reached the mice's brain faster, was more potent at the tumor site, and remained in the brain longer compared with nonmodified SPIO. The MPI signal of the brain tumor increased more than 20 times after the injection of the CCM-SPIO, manifesting outstanding glioma-targeting competence of the nanoprobe. In addition, benefitting from the excellent photothermal effect of the inner SPIO of the nanoprobe in the near-infrared absorbance band, we could have effective PPT on mouse glioma models, with results demonstrating enhanced antitumor effect with CCM-SPIO accumulation at the tumor site. Collectively, the strategy of combining biomimetic cell membrane coating with magnetic nanoparticles provides indispensable pathways in MPI for deep-penetrating and sensitive tissue applications. Once patient-specific CCM can be obtained from the source cancer cells, it may be of greatest interest to address the cancer heterogeneity arising from the coexistence of multiple cell types with different phenotypes and improve patient-specific treatment and promote the development of personalized treatment. Lastly, it should be noted that we were unable to work with large animals in this study due to the space confinement of the current MPI system, which, however, is not bounded in principle (as demonstrated in Figure 37C&D) and can be extended for large animals or even human applications once the MPI system can be engineered to hold large samples. It is collectively implied that the proposed platform can provide new insights and pathways to the noninvasive diagnosis and targeted treatment of *in situ* early-stage GBM.

Chapter 4 In situ therapeutic agent delivery monitoring with photoacoustic imaging

This chapter is reproduced with some adaptations from the manuscript "Y. Zhou, X. Huang*, J. Li, T. Zhu, W. Pang, L. Chow, L. Nie, L. Sun, P. Lai. Small Animal In Situ Drug Delivery Effects via Transdermal Microneedles Array versus Intravenous Injection: A Pilot Observation Based on Photoacoustic Tomography, Pharmaceutics, 2022, 14(12): 2689". The contributions of authors are as follows: P. Lai, Y. Zhou, and X. Huang conceived the idea. Y. Zhou and X. Huang ran the experiments. * make the equal contribution to this work. All authors were participated the manuscript and involved in revision.*

The heterogeneity of tumors and individual differences of patients will lead to differences in treatment effects, and new drug delivery methods will be explored. Non-invasive imaging is imperative to monitor the delivery of therapeutic agents to the brain and assess their efficacy. In this chapter, we demonstrated the scenario that using bio-imaging stratagem for drug delivery monitoring. The real-time distribution and concentration of the drugs can be used to optimize the therapeutic strategy and improve the treatment outcomes for patients with glioblastoma.

4.1 Motivation of this study

As one of the most common drug delivery methods, intravenous injection provides a fast, cost-effective, and direct way to deliver almost any biotherapeutic and vaccines into the body to realize the goal of treatment. Injection syringe, however, usually needs to be operated by healthcare professionals, which is not convenient for home care. Moreover, the pain and potential risk of wound infection associated with the injection of syringe lead to further inaccessibility to certain patients, especially kids [173, 174]. Transdermal drug delivery overcomes the disadvantages of intravenous administration, offering various merits such as better compliance and reduced systemic drug

interactions [175]. Microneedles (MNs), a promising minimally invasive transdermal drug delivery method, have drawn significant interest and attention in biomedicine in recent years [176, 177]. MNs, in general, are fabricated with hundreds of needles of micrometer length to puncture through the stratum corneum barrier to deliver drugs, which are painless, noninvasive or minimally invasive, and operate convenient [178]. Among diverse types of MNs, polymer MNs is one of the most popular branches due to its satisfactory properties in biocompatibility, biodegradability, nontoxicity, controllable dosage, and easy fabrication [179, 180].

As a symbolic drug delivery method, timely monitoring and evaluation of the administration effects of MNs are profitable and worthwhile in appraising the drug performance in specific diseases. It is also constructive to guide further renovation of the MNs fabrication. Current techniques to evaluate the drug administration effects of deep-tissue diseases like brain tumors [181] and diabetes [182, 183] mainly rely on blood test and bioluminescence imaging, which, however, encounters cumbersome and painfulness for blood tests or instability for bioluminescence imaging based on the metabolism circulation time and quantity of luciferase substrate [184]. Therefore, imaging technologies that can provide real-time, noninvasive, precise, and *in vivo* monitoring and analysis are highly desired for evaluating the effects of drug delivery via MNs.

PAI is believed to provide low-cost, high-resolution, real-time imaging of clinical brain function. Existing high-resolution brain imaging methods, including CT, MRI, and US, have limitations. Non-ionizing, high-resolution, and real-time imaging patterns help detect brain functions such as stroke, head injury, tumors, and brain infections. In some cases, ultrasound brain imaging comes close to meeting these goals. Ultrasound is the established pediatric brain imaging method before the fontanelle closes. After the fontanelle approaches, the image quality decreases significantly because the skull is

severely attenuated and distorted by ultrasound. Fortunately, unlike pulse-echo ultrasound imaging, PAT only involves unidirectional ultrasonic attenuation and distortion due to the skull. PAT provides rich contrast for high-resolution structural and functional imaging. As demonstrated by diffuse optical tomography, near-infrared light can penetrate the skull to reach the cortex and has been used for functional brain imaging with low spatial resolution. PAT may provide similar penetration but with higher resolution [185]. Benefiting from the wavelength-dependent featured absorption spectrum for different tissue components, PAI can detect specific targets via endogenous or exogenous absorption contrasts, which can serve as a valuable tool to track the delivery of drugs and further evaluate their effects [186, 187]. Monthanchery *et al*. presented to utilize optical resolution PAM to characterize the transdermal delivery of NPs using microneedles but is still limited in superficial skin [188].

In this chapter, we propose to use PACT to precisely and non-invasively monitor the drug delivery effects of transdermal administration by degradable indocyanine green (ICG)-loaded hyaluronic acid MNs (ICG-HA-MNs) in deep mouse glioma models. The drug delivery effects are further systematically and quantitatively compared with intravenous injection. With PACT, signals originating from ICG can be sensitively detected in the tumor region after tail vein injection or MNs puncturing the skin surface. Experimental results indicate that intravenous injection could bring a faster drug-responsive effect but shorter drug duration performance. As opposed, the tumor regions of mice in the MNs group demonstrate a lower drug signal intensity yet prolonged drug lasting time, corresponding to limited drug loading and controllable drug release characteristics, respectively. The efficiency of transdermal administration by MNs can be further improved if more ICG can be loaded. Although many aspects can be further improved in the next phase, this pilot study suggests that PACT can be used as a potential in situ imaging modality to evaluate the effects of drug delivery on small animals and provide constructive guidance for the design and fabrication of MNs.

4.2 Methodology

4.2.1 Cells Culturing and Preparation

Luciferase-tagged U87 glioma cells were cultured with high glucose Dulbecco's modified Eagle's medium (DMEM) supplemented with 10% fetal bovine serum (FBS) and 0.1% penicillin-streptomycin [189]. After three cell passage times, the cells in good conditions were centrifugated and washed twice with the PBS to get the cell pellet.

4.2.2 U87 Xenograft Tumor Model

Twelve female Balb/c nude mice were anesthetized by a mixture of ketamine (100 mg/kg), xylazine (10 mg/kg). With the help of a stereotaxic instrument, the Luciferase-tagged U87 cells (1×10^6 cells in a volume of 5 μL) were inoculated into the right caudate nucleus of the mice to establish the U87 xenograft tumor model [190]. All procedures in the animal experiments were approved by the animal ethical committee of the Hong Kong Polytechnic University. Bioluminescence imaging using the Perkin-Elmer IVIS Lumina Series III system was conducted approximately 14 days after cell implantation to ensure the successful creation of glioma tumor models [191]. The U87 tumor model would express fluorescence signals only a few minutes after the injection of luciferin substrate.

4.2.3 Materials and The Fabrication Process of ICG Microneedles Array

Indocyanine green (ICG), the sole infrared-contrast agent approved by Food and Drug Administration (USA) for clinical applications, was used to serve as the drug to be delivered and monitored. The ICG (dye content 90%) was purchased from Beijing J&K Scientific Co. Ltd. (China). Hyaluronic acid (HA), widely adopted to fabricate dissolving microneedles for transdermal drug delivery, was chosen in this study [192-194]. The sodium hyaluronic (Mw < 10000) was supplied by Bloomage Biotech (China).

The ICG-HA-MNs was fabricated via two-casting methods [195]. Firstly, the MNs metal master mold containing MNs arranged in 10 × 10 arrays, with a needle height of 900 μm and base area of 0.09 mm^2 (300 μm × 300 μm), was immersed into SPION solution. The PDMS solution with MNs mold was put into the oven at a temperature of 65-70 centigrade for 3 h to dry after being degassed. The MNs metal master was removed after the PDMS was cured, obtaining the PDMS mold as shown in Figure 49A. 2 mL casting solution mixed with ICG solution (1 mg/ ml) and HA solution (1 g/ ml) at a volume ratio of 1:1 was then cast into the PDMS mold which was placed in a 50 mL corning tube. The final mixed solution spread on the surface of the PDMS mold. The corning tube containing the PDMS mold and drug-loaded solution was centrifugated at 4000 rpm for 10 min to fill the cavities in the PDMS mold. Subsequently, the PDMS mold filled with ICG-loaded solution was taken out and dried at room temperature for 24 h. The microneedles array could be easily demolded in the next day, and the microneedles array was finally ready.

4.2.4 Optical and Mechanical Characterizations of MNs

Macro- and micro-optical images of the ICG-HA-MNs were obtained by digital camera and microscopy, respectively. To ensure the mechanical property of the MNs, a patch of fresh porcine skin was vertically punctured by the ICG-HA-MNs for 5 min, and then taken for tissue fixation and histological examination. Skin sections were attached on a glass slide, and the intactness of the stratum corneum was observed under microscopy.

4.2.5 PACT Monitoring and Evaluation of The Drug Delivery Effects

The PA platform used for this work was FUJIFILM Visual Vevo LAZR multi-modality imaging system, equipped with a broadband ultrasound frequency transducer (Vevo LAZR LZ250, 13-24 MHz). The wavelengths used in this study were 680, 695, 732, 882, and 924 nm. Here we used five wavelengths to locate the tumor region accurately,

and we only analyzed the ICG signals by unmixing the spectrum using the VevoLAB software.

Before experiments, the mice were divided into two groups (n = 3/group) and anesthetized with isoflurane. In the injection group, ICG solutions (200 nmol in 0.15 mL for each mouse) were injected into the tail veins. In the MNs group, two patches of ICG-HA-MNs were punctured into the back skin of mice for 5 min. Well-prepared mice were placed on the heating pad and monitored by the abovementioned PA/US dual-mode platform following the timeline. Given the high metabolism rate of the ICG, the timeline we chose in this study was pre-experiment, 15 min, 30 min, 1 h, 2 h, 3 h, 4 h, and 24 h post-drug delivery.

4.2.6 Statistical Analysis

The student's two-tailed, unpaired t-test was adopted to compare the two groups with the corresponding p-value. Each asterisk in a plot denotes a significant difference between the two data groups ($p < 0.05$) unless additionally specified in the figure caption. Standard errors were noted, taking into the account of the subject-to-subject variations, and represented as error bars in the result figures.

4.3 Results

4.3.1 Characterization of MNs

As shown in Figure 49B, 10 × 10 cone-shaped microneedles are orderly and uniformly fabricated on the substrate. The whole patch expresses a uniform dark green color, reflecting the color of the ICG solution. Figure 49C shows the cross-section of the ICG-HA-MNs patch. The uniform green color of the needles indicates that the ICG was loaded into the HA microneedles homogenously. The microneedles' average height and base diameter were 900 and 300 μm, respectively. More information about the

microneedle tips can be observed in Figure 49D, where the sharp feature helps to puncture the skin more easily.

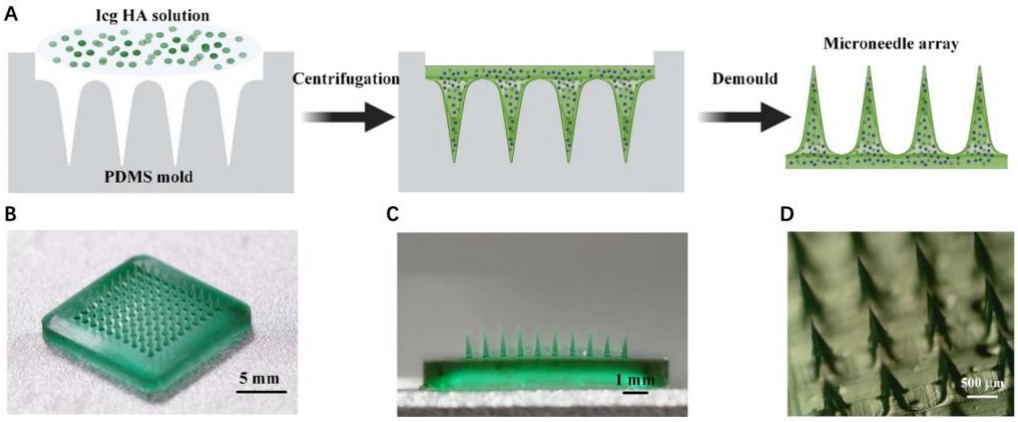

Figure 49. (A) Schematic of the fabrication process of ICG-HA-MNs. (B) Photography of ICG-HA-MNs patch in full view. (C) Cross-sectional view of the ICG-HA-MNs patch. (D) Stereomicroscopy image of the ICG-HA-MNs.

4.3.2 Skin penetration test

After being punctured by the ICG-HA-MNs for around 5 min, the substrate of the MNs patch was removed from the porcine skin. The tips of the MNs patch were dissolved in the skin, as shown in Figure 50A. The surface of the porcine skin resembles the regular and uniform shape of the MNs. The light green ICG dot array on the skin surface fitted well with the arrangements of microneedles. Figure 50B shows the histological view of the cross-section of the punctured porcine skin. A hole with a depth of approximately 80 μm created by the microneedles can be observed, with ICG dissolved inside. This result indicates that the ICG-HA-MNs possess enough mechanical property to penetrate the stratum corneum to deliver the drugs as the layer thickness of the stratum corneum is around 10-15 μm.

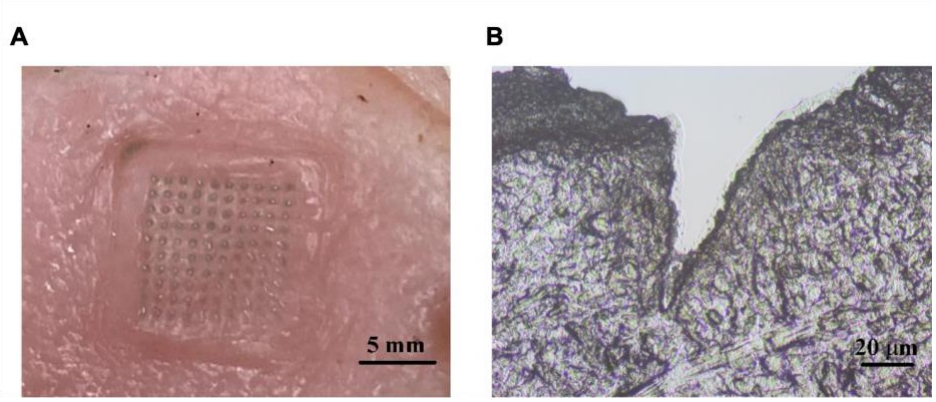

Figure 50. (A) Photography of MNs punctured porcine skin. (B) Histological slice of the porcine skin along the cross section in the punctured site, showing the trace of microneedle insertion into the tissue sample.

4.3.3 Dynamic monitoring of drug delivery effects via intravenous injection

With the help of the IVIS bioluminescence detection system, we first checked if the U87 xenograft tumor model was established successfully. The mouse brain tumor regions presented fluorescence signals after luciferin injection, indicating successful animal tumor modeling. Then the PACT monitoring experiments were conducted. Figure 51A shows the ultrasound (grey background) and PA (colored values) images of the tumor region that change with time. As seen, no ICG signal is observed before injection, and the tumor region expresses strong ICG signals just 15 min post-injection. The strong ICG signals sustain for 30 min, which, however, is followed with rapid decrease and even reduce to baseline 4-h post-injection. The PA signals in the encircled ROIs are selected and calculated to make a quantitative comparison, as illustrated in Figure 51B. It is confirmed that the ROIs manifest strong ICG signals in 15 min post-injection with a statistically significant difference compared to the baseline. The ICG signals display a maximum amplitude in 30 min, a rapid drop after 30 min, and then gradual decrease back to the baseline after ~4 h, which is consistent with the trend shown in Figure 51A and previous reported results [196].

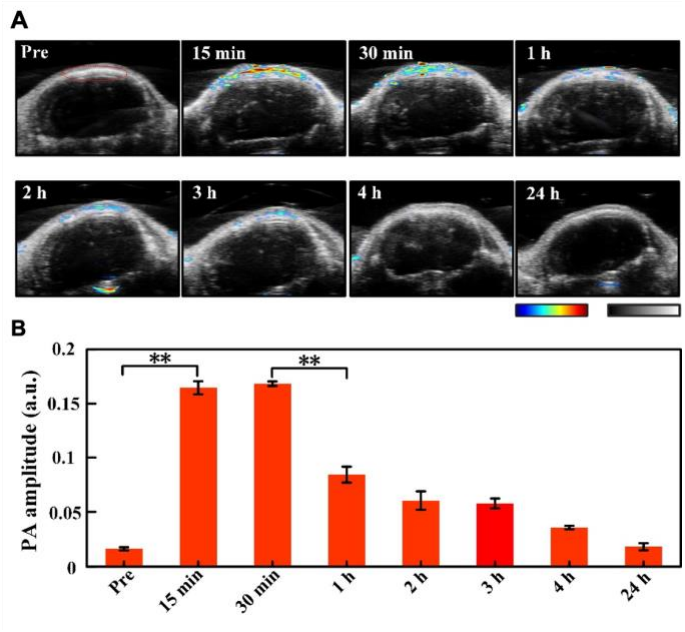

Figure 51. (A) Ultrasound (the grey background) and PA (the colored values) images of the tumor region with time pre- and post-injection. The region encircled by the red curve in the "Pre" picture is the ROI used for data analysis, which is identical for all images acquired at different time moments. (B) Quantitative PA amplitude of ICG signals (spectral unmixing) in the tumor region at different time points after injection. **, $p < 0.01$, *, $p < 0.05$ (tested by Student's two-tailed, unpaired t-test). The error bars in b are standard deviations.

4.3.4 Dynamic monitoring of the transdermal administration effects via MNs

Figure 52A depicts the ultrasound and PA images of the tumor region with time using the MNs to deliver ICG. As seen, the tumor site shows a clear PA signal from ICG 15 min after MNs puncture, and the strong PA signal lasts about 3 h. PA images acquired 4 h after MNs puncture still demonstrates a significant ICG level. Quantitative PA amplitude analysis of the ROIs circled by the red line in Figure 52A is exhibited in Figure 52B, where the ICG signal in the tumor region elevates to a statistically significant different level 15 min post-MNs puncture as compared to the baseline. The PA signal of ICG rises to its maximum amplitude around 1-h post-MNs puncture, and

the high-level PA signal lasts ~3 h. Even 4 h post-MNs puncture, the PA signal remains at more than half of the maximum level.

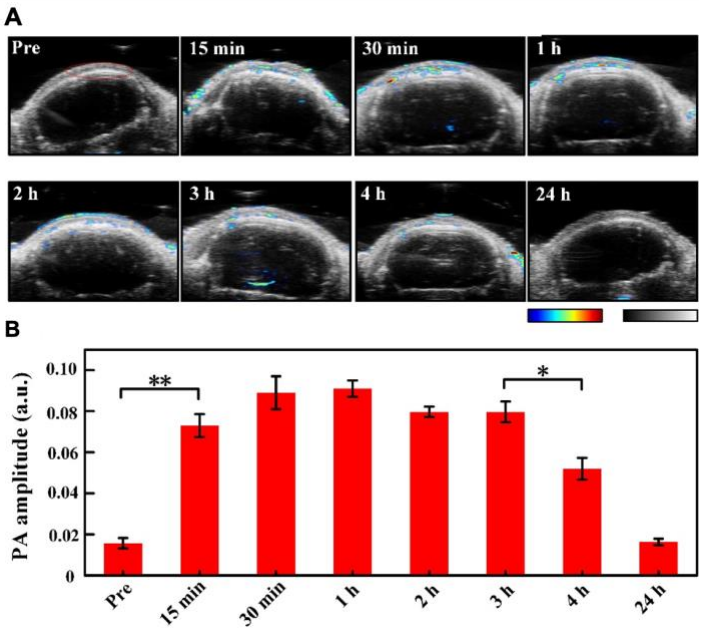

Figure 52. (A) Ultrasound (the grey background) and PA (the colored values) images of the tumor region with time pre- and post-MNs puncturing. The region encircled by the red curve in the "Pre" picture is the ROI used for data analysis, which is identical for all images acquired at different time moments. (B) Quantitative PA amplitude of ICG signals (spectral unmixing) in the tumor region at different time points after MNs puncturing. **, $p < 0.01$, *, $p < 0.05$ (tested by Student's two-tailed, unpaired t-test). The error bars in b are standard deviations.

4.3.5 Comparison of the drug delivery effects between injection and MNs

Figure 53 presents the comparison of the PA signal amplitudes over time following the administration of ICG via the two different drug delivery methods. As seen, the drug signals demonstrate a sharper and higher-level (maximum PA amplitude) elevation within the same time frame by intravenous injection, indicating a faster drug-responsive effect and higher drug-loading performance. That said, the duration of the strong ICG signals in the injection group is shorter than that in the transdermal administration group. In comparison, the ICG signals reveal a lower-level intensity rise yet prolonged durable

performance by MNs, suggesting lower drug loading behavior and slower drug release characteristics. Also, the ICG signals in both groups increased significantly 15 min post administration of ICG, suggesting a high metabolism rate and fast, responsive property of ICG in the blood circulatory system, which is also consistent with the reported findings [196]. The first time point we chose is 15 min not mean that no ICG signals are detected before 15 min. It also should be clarified that the observed difference in drug delivery effects between intravenous injection and transdermal administration via MNs may be limited to ICG only; if other micro-dose high-efficiency drugs like insulin are applied, the trend might not be that obvious or even be rather different [182].

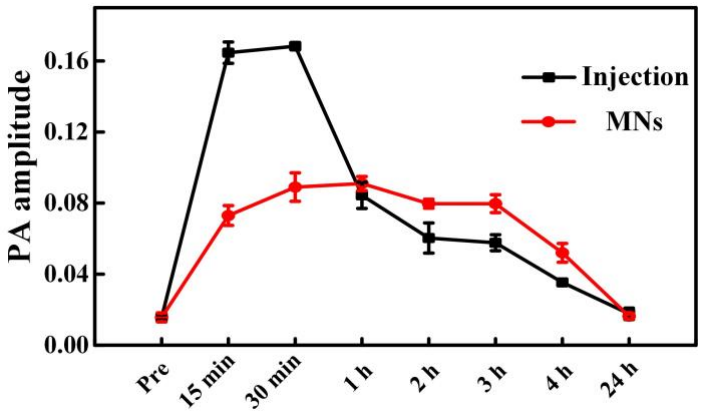

Figure 53. Comparison of the amplitude of PA signals originated from the delivered ICG after injection and transdermal administration of the ICG-HA-MNs.

4.4 Summary of this study

To precisely, non-invasively, and timely monitor and evaluate the drug delivery efficiency of transdermal administration by MNs and intravenous injection, we introduce PACT to record the in-situ responses from drugs, i.e., PA signals from ICGs, at different time slots and quantitatively compare the ICG signal intensities in the glioma tumor region. It reveals that the in the intravenous injection group, ICG signals exhibit a rapid increase 15 min after tail injection, and the strong PA signals start to decrease rapidly only 30 min post-injection. In contrast, in the MNs group, the maximum amplitude of ICG signals is much lower than its peer in the injection group,

suggesting less drug loading features of MNs for ICG. Nevertheless, the ICG signals express a more durable lasting time post-MNs puncture, and the declining time point is much later (around 3 h post-MNs) than the injection group. These results suggest that intravenous injection presents a fast drug-responsive property yet reduces drug duration time. At the same time, the transdermal administration by MNs has a relatively low ICG loading efficiency yet prolonged drug release duration. Note that the contrast of PA signals in this study is based on the ICG. Thus, the PA signal amplitudes in the injection group differ significantly from the MNs group (lower ICG load). The differences may not be evident if other micro-dose high-efficiency drugs are used or if more ICGs can be loaded in the MNs array. It is exactly this point that indicates that the transdermal administration by MNs should be more suitable for low-dose sensitive drugs of high curing efficiency (not delivery efficiency) in the current stage. In the future, the MNs may also be further improved to carry more drugs to optimize their performance based on requirements. To summarize, this pilot study suggests that the PACT can be used as a potential imaging modality to precisely, non-invasively, and timely evaluate the drug delivery performance and provide constructive guidance for designing and fabricating MNs.

Chapter 5 Conclusion and outlook

A series of biological changes occur in the early stages of a tumor, such as metabolites, circulating tumor genes, microorganisms, and nerves. After angiogenesis, a tumor microenvironment is formed that accelerates tumor growth or metastasis. Detecting tumor formation at the earliest possible stage and then providing active intervention is the key to improving the survival rate of cancer patients. Identification of early tumorigenesis events requires high-resolution imaging that can penetrate deep into biological tissue and sensitively respond to molecular probes that can precisely target and accumulate at the tumor site(s). This thesis mainly focuses on the applications of two emerging molecular imaging modalities, PAI and MPI, in cancer diagnosis and therapeutic monitoring. Starting from the basics and system introduction, we have explored the unique and novel properties of these two modalities that afford them great potentials for early cancer diagnosis.

Basically, PAI is a convenient and cost-effective imaging modality that combines ultrasonic spatial resolution and optical absorption contrast to visualize molecular events in deep tissues. With endogenous contrast agents, such as oxy/deoxygenated hemoglobin, PAI can reveal the structural information that shows the abnormal behavior due to tumor neogenesis. For instance, for developing tumors, angiogenesis can be detected, which supplies nutrients to the tumor, as evidenced by a stronger oxygenated hemoglobin PA signal with higher intensity of the vascular. Moreover, with the assistance of exogenous contrast agents, the PA signals can be magnified to visualize tiny changes that are otherwise difficult to be determined, for example, in our study, 2-mm-diameter tumors in the small animal liver.

MPI is a tracer-based functional and tomographic imaging technique that identifies the spatial distribution of MNPs. MPI signal only comes from the superparamagnetic MNPs, based on the instantaneous non-linear response of MNPs from zero to saturation

to the oscillating magnetic field. This leads to extremely high spatial and temporal resolution even with very thick biological tissues. By excluding the background noise, precise imaging with high SNR can be achieved. Furthermore, MPI has no penetration limit, so the number of SPION can be linearly quantified, which is impossible with optical imaging. As the MPI signal is generated by the MNPs' magnetic response voltage, traces are essential elements in MPI, which is a bit different from the scenario in PAI.

Nevertheless, NPs used in both imaging modalities have been discussed in this thesis. Many NPs have entered clinical trials, fortunately including gold and iron oxide NPs, the representative contrast agents for PAI and MPI, respectively. Therefore, the clinical implementation of PAI and MPI with exogenous contrast agents for cancer diagnosis and treatment monitoring is predictable. That said, MPS, which are abundant in organs such as the liver and spleen, captures most of these contrast agents and prevent them from reaching and accumulating at the target diseased sites, leading to significant challenges in the efficacy and biocompatibility of NPs. In this thesis, biomimetic strategies using original membranes from red blood cells or cancer cells to camouflage NPs are recommended because of their natural properties of immune escape, prolonged blood circulation, immune regulation, and homogenous targeting. In addition, the lipid vesicle structure is the ideal delivery platform that can load a large amount of imaging contrast agents and drugs. In one study, red blood cell membranes-coated AuNSs were investigated for early diagnosis of liver cancer. Due to the MPS escape and prolonged circulation, the probe can accumulate more in the tumor site by EPR effect, resulting in enhanced PAI sensitivity in the detection of small tumors. Another study demonstrated that the homogenous cancer cell membrane-coated SPIO can break through the BBB and target the glioma, which can be precisely visualized by 2D-MPI and 3D-MPI/CT. For drug delivery monitoring, PAI is used to monitor MNs delivery, revealing the novel drug delivery characteristics and dynamic distribution in glioma. This study

demonstrates the feasibility of real-time *in vivo* drug imaging and provides a basis for personalized medicine research.

In future works, multiple imaging modalities could be combined to better visualize the tumor microenvironment. Taking the advantages of PAI's natural optical contrast imaging and MPI's precise quantification of NP, for example, it is possible to visualize and study the critical molecules in tumor development. Understanding how the key molecules function during tumor development can help solve the problem of tumor grading and classification, thus contributing to personalized treatment. As a novel imaging approach, MPI's biological applications remain to be explored, especially in the tracking and quantification of therapeutic agents, such as therapeutic cells and MNs administration. Moreover, although we were unable to do experiments on large animals in this work, it should be highlighted that the combination strategy of a biomimetic cell membrane coating and MNPs provides indispensable advantages in MPI for deep tissue precise detection. From the perspective of biomimetic nanoprobes, more efficient preparation methods could be investigated to obtain stable and uniformly wrapped probes. In addition, hybrid cell membranes and genetic engineering could be utilized to obtain fully functional biomimetic NPs. For clinical transformation, the biosafety and pharmacokinetics of biomimetic nanoprobes are worthy of deep thinking and research. The combination of imaging technology and artificial intelligence can be used to systematically study and analyze the behavior of biomimetic nanoprobes *in vivo*. In conclusion, high-resolution and deep-penetrating cancer diagnosis and treatment technologies are around the corner. With the assistance or enhancement of biomimetic molecular probes, sensitive and personalized theranostics of cancer are on the horizon.

REFERENCES

[1] A. Srivastava, D.J. Creek, Discovery and Validation of Clinical Biomarkers of Cancer: A Review Combining Metabolomics and Proteomics, Proteomics 19(10) (2019) e1700448.
[2] R.L. Siegel, K.D. Miller, A. Jemal, Cancer statistics, 2018, CA Cancer J Clin 68(1) (2018) 7-30.
[3] D. Crosby, S. Bhatia, K.M. Brindle, L.M. Coussens, C. Dive, M. Emberton, S. Esener, R.C. Fitzgerald, S.S. Gambhir, P. Kuhn, T.R. Rebbeck, S. Balasubramanian, Early detection of cancer, Science 375(6586) (2022) eaay9040.
[4] S. Cristiano, A. Leal, J. Phallen, J. Fiksel, V. Adleff, D.C. Bruhm, S.O. Jensen, J.E. Medina, C. Hruban, J.R. White, D.N. Palsgrove, N. Niknafs, V. Anagnostou, P. Forde, J. Naidoo, K. Marrone, J. Brahmer, B.D. Woodward, H. Husain, K.L. van Rooijen, M.W. Orntoft, A.H. Madsen, C.J.H. van de Velde, M. Verheij, A. Cats, C.J.A. Punt, G.R. Vink, N.C.T. van Grieken, M. Koopman, R.J.A. Fijneman, J.S. Johansen, H.J. Nielsen, G.A. Meijer, C.L. Andersen, R.B. Scharpf, V.E. Velculescu, Genome-wide cell-free DNA fragmentation in patients with cancer, Nature 570(7761) (2019) 385-389.
[5] V. Gopalakrishnan, C.N. Spencer, L. Nezi, A. Reuben, M.C. Andrews, T.V. Karpinets, P.A. Prieto, D. Vicente, K. Hoffman, S.C. Wei, A.P. Cogdill, L. Zhao, C.W. Hudgens, D.S. Hutchinson, T. Manzo, M. Petaccia de Macedo, T. Cotechini, T. Kumar, W.S. Chen, S.M. Reddy, R. Szczepaniak Sloane, J. Galloway-Pena, H. Jiang, P.L. Chen, E.J. Shpall, K. Rezvani, A.M. Alousi, R.F. Chemaly, S. Shelburne, L.M. Vence, P.C. Okhuysen, V.B. Jensen, A.G. Swennes, F. McAllister, E. Marcelo Riquelme Sanchez, Y. Zhang, E. Le Chatelier, L. Zitvogel, N. Pons, J.L. Austin-Breneman, L.E. Haydu, E.M. Burton, J.M. Gardner, E. Sirmans, J. Hu, A.J. Lazar, T. Tsujikawa, A. Diab, H. Tawbi, I.C. Glitza, W.J. Hwu, S.P. Patel, S.E. Woodman, R.N. Amaria, M.A. Davies, J.E. Gershenwald, P. Hwu, J.E. Lee, J. Zhang, L.M. Coussens, Z.A. Cooper, P.A. Futreal, C.R. Daniel, N.J. Ajami, J.F. Petrosino, M.T. Tetzlaff, P. Sharma, J.P. Allison, R.R. Jenq, J.A. Wargo, Gut microbiome modulates response to anti-PD-1 immunotherapy in melanoma patients, Science 359(6371) (2018) 97-103.
[6] R.L. Siegel, K.D. Miller, S.A. Fedewa, D.J. Ahnen, R.G.S. Meester, A. Barzi, A. Jemal, Colorectal cancer statistics, 2017, CA Cancer J Clin 67(3) (2017) 177-193.
[7] D. Hanahan, L.M. Coussens, Accessories to the crime: functions of cells recruited to the tumor microenvironment, Cancer Cell 21(3) (2012) 309-22.
[8] A.K. Palucka, L.M. Coussens, The Basis of Oncoimmunology, Cell 164(6) (2016) 1233-1247.
[9] S.P. Rowe, M.G. Pomper, Molecular imaging in oncology: Current impact and future directions, CA Cancer J Clin 72(4) (2022) 333-352.
[10] M.A. Pysz, S.S. Gambhir, J.K. Willmann, Molecular imaging: current status and emerging strategies, Clin Radiol 65(7) (2010) 500-16.
[11] M. Saeed, Z. Xu, B.G. De Geest, H. Xu, H. Yu, Molecular Imaging for Cancer Immunotherapy: Seeing Is Believing, Bioconjug Chem 31(2) (2020) 404-415.
[12] T. Hussain, Q.T. Nguyen, Molecular imaging for cancer diagnosis and surgery, Adv Drug Deliv Rev 66 (2014) 90-100.
[13] R. Weissleder, M.J. Pittet, Imaging in the era of molecular oncology, Nature 452(7187) (2008) 580-9.
[14] M.H. Xu, L.H.V. Wang, Photoacoustic imaging in biomedicine, Rev Sci Instrum 77(4) (2006).

[15] L.H.V. Wang, J.J. Yao, A practical guide to photoacoustic tomography in the life sciences, Nat Methods 13(8) (2016) 627-638.
[16] P.X. Lai, L.M. Nie, L.D. Wang, Special issue "Photoacoustic imaging: microscopy, tomography, and their recent applications in biomedicine" in visual computation for industry, biomedicine, and art, Vis Comput Ind Biome 4(1) (2021).
[17] Z. Yu, H. Li, T. Zhong, J.H. Park, S. Cheng, C.M. Woo, Q. Zhao, J. Yao, Y. Zhou, X. Huang, W. Pang, H. Yoon, Y. Shen, H. Liu, Y. Zheng, Y. Park, L.V. Wang, P. Lai, Wavefront shaping: A versatile tool to conquer multiple scattering in multidisciplinary fields, Innovation (Camb) 3(5) (2022) 100292.
[18] L.V. Wang, J. Yao, A practical guide to photoacoustic tomography in the life sciences, Nat Methods 13(8) (2016) 627-38.
[19] L.H.V. Wang, L. Gao, Photoacoustic Microscopy and Computed Tomography: From Bench to Bedside, Annu Rev Biomed Eng 16 (2014) 155-185.
[20] L.V. Wang, Tutorial on photoacoustic microscopy and computed tomography, Ieee J Sel Top Quant 14(1) (2008) 171-179.
[21] Y.Y. Zhou, F. Cao, H.H. Li, X.Z. Huang, D.S. Wei, L.D. Wang, P.X. Lai, Photoacoustic imaging of microenvironmental changes in facial cupping therapy, Biomed Opt Express 11(5) (2020) 2394-2401.
[22] M.M. Chen, X.Y. Duan, B.X. Lan, T. Vu, X.Y. Zhu, Q.Z. Rong, W. Yang, U. Hoffmann, J. Zou, J.J. Yao, High-speed functional photoacoustic microscopy using a water-immersible two-axis torsion-bending scanner, Photoacoustics 24 (2021).
[23] W. Qin, Q. Gan, L. Yang, Y.C. Wang, W.Z. Qi, B.W. Ke, L. Xi, High-resolution in vivo imaging of rhesus cerebral cortex with ultrafast portable photoacoustic microscopy, Neuroimage 238 (2021).
[24] L. Lin, P. Hu, X. Tong, S. Na, R. Cao, X.Y. Yuan, D.C. Garrett, J.H. Shi, K. Maslov, L.H.V. Wang, High-speed three-dimensional photoacoustic computed tomography for preclinical research and clinical translation, Nat Commun 12(1) (2021).
[25] L. Lin, P. Hu, J.H. Shi, C.M. Appleton, K. Maslov, L. Li, R.Y. Zhang, L.H.V. Wang, Single-breath-hold photoacoustic computed tomography of the breast, Nat Commun 9 (2018).
[26] X.Z. Huang, W.T. Shang, H. Deng, Y.Y. Zhou, F. Cao, C.H. Fang, P.X. Lai, J. Tian, Clothing spiny nanoprobes against the mononuclear phagocyte system clearance in vivo: Photoacoustic diagnosis and photothermal treatment of early stage liver cancer with erythrocyte membrane-camouflaged gold nanostars, Appl Mater Today 18 (2020).
[27] L.V. Wang, S. Hu, Photoacoustic tomography: in vivo imaging from organelles to organs, Science 335(6075) (2012) 1458-62.
[28] Y. Li, W. Zhang, V.P. Nguyen, X. Xia, X. Wang, Y.M. Paulus, Real-time guidance and monitoring of CNV through subretinal injection in rabbit eyes using multimodal PAM and OCT imaging system, Investigative Ophthalmology & Visual Science 60(9) (2019) 196-196.
[29] Y. Zhou, W. Xing, K.I. Maslov, L.A. Cornelius, L.V. Wang, Handheld photoacoustic microscopy to detect melanoma depth in vivo, Opt Lett 39(16) (2014) 4731-4.

[30] J. Yao, L. Wang, J.M. Yang, K.I. Maslov, T.T. Wong, L. Li, C.H. Huang, J. Zou, L.V. Wang, High-speed label-free functional photoacoustic microscopy of mouse brain in action, Nat Methods 12(5) (2015) 407-10.
[31] T. Jin, H. Guo, H. Jiang, B. Ke, L. Xi, Portable optical resolution photoacoustic microscopy (pORPAM) for human oral imaging, Opt Lett 42(21) (2017) 4434-4437.
[32] X. Zhu, Q. Huang, A. DiSpirito, T. Vu, Q. Rong, X. Peng, H. Sheng, X. Shen, Q. Zhou, L. Jiang, U. Hoffmann, J. Yao, Real-time whole-brain imaging of hemodynamics and oxygenation at micro-vessel resolution with ultrafast wide-field photoacoustic microscopy, Light Sci Appl 11(1) (2022) 138.
[33] Z. Ali, C. Zakian, Q. Li, J. Gloriod, S. Crozat, F. Bouvet, G. Pierre, V. Sarantos, M. Di Pietro, K. Flisikowski, P. Andersen, W. Drexler, V. Ntziachristos, 360(masculine) optoacoustic capsule endoscopy at 50 Hz for esophageal imaging, Photoacoustics 25 (2022) 100333.
[34] H. Ikematsu, M. Ishihara, S. Okawa, T. Minamide, T. Mitsui, T. Kuwata, M. Ito, T. Kinoshita, T. Fujita, T. Yano, T. Omori, S. Ozawa, D. Murakoshi, K. Irisawa, A. Ochiai, Photoacoustic imaging of fresh human surgically and endoscopically resected gastrointestinal specimens, DEN Open 2(1) (2022) e28.
[35] J. Aguirre, M. Schwarz, N. Garzorz, M. Omar, A. Buehler, K. Eyerich, V. Ntziachristos, Precision assessment of label-free psoriasis biomarkers with ultra-broadband optoacoustic mesoscopy, Nature Biomedical Engineering 1(5) (2017) 0068.
[36] Y. Ishida, A. Otsuka, T. Honda, Y. Asao, H. Sekiguchi, A. Yoshikawa, T. Yagi, K. Kabashima, Photoacoustic imaging system visualizes restoration of peripheral oxygenation in psoriatic lesions, J Eur Acad Dermatol Venereol 32(12) (2018) e449-e451.
[37] J. Reber, M. Willershauser, A. Karlas, K. Paul-Yuan, G. Diot, D. Franz, T. Fromme, S.V. Ovsepian, N. Beziere, E. Dubikovskaya, D.C. Karampinos, C. Holzapfel, H. Hauner, M. Klingenspor, V. Ntziachristos, Non-invasive Measurement of Brown Fat Metabolism Based on Optoacoustic Imaging of Hemoglobin Gradients, Cell Metab 27(3) (2018) 689-701 e4.
[38] L. Lin, L.V. Wang, The emerging role of photoacoustic imaging in clinical oncology, Nat Rev Clin Oncol 19(6) (2022) 365-384.
[39] S. Wang, L. Zhang, J. Zhao, M. He, Y. Huang, S. Zhao, A tumor microenvironment-induced absorption red-shifted polymer nanoparticle for simultaneously activated photoacoustic imaging and photothermal therapy, Sci Adv 7(12) (2021) eabe3588.
[40] X. Cai, L. Li, A. Krumholz, Z. Guo, T.N. Erpelding, C. Zhang, Y. Zhang, Y. Xia, L.V. Wang, Multi-scale molecular photoacoustic tomography of gene expression, PLoS One 7(8) (2012) e43999.
[41] K. Sivasubramanian, V. Periyasamy, M. Pramanik, Non-invasive sentinel lymph node mapping and needle guidance using clinical handheld photoacoustic imaging system in small animal, J Biophotonics 11(1) (2018).
[42] A.A. Oraevsky, B. Clingman, J. Zalev, A.T. Stavros, W.T. Yang, J.R. Parikh, Clinical optoacoustic imaging combined with ultrasound for coregistered functional and anatomical mapping of breast tumors, Photoacoustics 12 (2018) 30-45.
[43] B. Gleich, J. Weizenecker, Tomographic imaging using the nonlinear response of magnetic particles, Nature 435(7046) (2005) 1214-7.

[44] N. Panagiotopoulos, R.L. Duschka, M. Ahlborg, G. Bringout, C. Debbeler, M. Graeser, C. Kaethner, K. Ludtke-Buzug, H. Medimagh, J. Stelzner, T.M. Buzug, J. Barkhausen, F.M. Vogt, J. Haegele, Magnetic particle imaging: current developments and future directions, Int J Nanomedicine 10 (2015) 3097-114.
[45] X. Yang, G. Shao, Y. Zhang, W. Wang, Y. Qi, S. Han, H. Li, Applications of Magnetic Particle Imaging in Biomedicine: Advancements and Prospects, Front Physiol 13 (2022) 898426.
[46] P. Chandrasekharan, Z.W. Tay, X.Y. Zhou, E. Yu, R. Orendorff, D. Hensley, Q. Huynh, K.L.B. Fung, C.C. VanHook, P. Goodwill, B. Zheng, S. Conolly, A perspective on a rapid and radiation-free tracer imaging modality, magnetic particle imaging, with promise for clinical translation, Br J Radiol 91(1091) (2018) 20180326.
[47] E.U. Saritas, P.W. Goodwill, L.R. Croft, J.J. Konkle, K. Lu, B. Zheng, S.M. Conolly, Magnetic particle imaging (MPI) for NMR and MRI researchers, J Magn Reson 229 (2013) 116-26.
[48] L.M. Bauer, S.F. Situ, M.A. Griswold, A.C. Samia, Magnetic Particle Imaging Tracers: State-of-the-Art and Future Directions, J Phys Chem Lett 6(13) (2015) 2509-17.
[49] P. Keselman, E.Y. Yu, X.Y. Zhou, P.W. Goodwill, P. Chandrasekharan, R.M. Ferguson, A.P. Khandhar, S.J. Kemp, K.M. Krishnan, B. Zheng, S.M. Conolly, Tracking short-term biodistribution and long-term clearance of SPIO tracers in magnetic particle imaging, Phys Med Biol 62(9) (2017) 3440-3453.
[50] E.Y. Yu, P. Chandrasekharan, R. Berzon, Z.W. Tay, X.Y. Zhou, A.P. Khandhar, R.M. Ferguson, S.J. Kemp, B. Zheng, P.W. Goodwill, M.F. Wendland, K.M. Krishnan, S. Behr, J. Carter, S.M. Conolly, Magnetic Particle Imaging for Highly Sensitive, Quantitative, and Safe in Vivo Gut Bleed Detection in a Murine Model, ACS Nano 11(12) (2017) 12067-12076.
[51] A.C. Bakenecker, M. Ahlborg, C. Debbeler, C. Kaethner, T.M. Buzug, K. Ludtke-Buzug, Magnetic particle imaging in vascular medicine, Innov Surg Sci 3(3) (2018) 179-192.
[52] K.M. Parkins, K.P. Melo, Y. Chen, J.A. Ronald, P.J. Foster, Visualizing tumour self-homing with magnetic particle imaging, Nanoscale 13(12) (2021) 6016-6023.
[53] P. Ludewig, N. Gdaniec, J. Sedlacik, N.D. Forkert, P. Szwargulski, M. Graeser, G. Adam, M.G. Kaul, K.M. Krishnan, R.M. Ferguson, A.P. Khandhar, P. Walczak, J. Fiehler, G. Thomalla, C. Gerloff, T. Knopp, T. Magnus, Magnetic Particle Imaging for Real-Time Perfusion Imaging in Acute Stroke, ACS Nano 11(10) (2017) 10480-10488.
[54] X.Y. Zhou, K.E. Jeffris, E.Y. Yu, B. Zheng, P.W. Goodwill, P. Nahid, S.M. Conolly, First in vivo magnetic particle imaging of lung perfusion in rats, Phys Med Biol 62(9) (2017) 3510-3522.
[55] Q. Wang, X. Ma, H. Liao, Z. Liang, F. Li, J. Tian, D. Ling, Artificially Engineered Cubic Iron Oxide Nanoparticle as a High-Performance Magnetic Particle Imaging Tracer for Stem Cell Tracking, ACS Nano 14(2) (2020) 2053-2062.
[56] G. Song, M. Chen, Y. Zhang, L. Cui, H. Qu, X. Zheng, M. Wintermark, Z. Liu, J. Rao, Janus Iron Oxides @ Semiconducting Polymer Nanoparticle Tracer for Cell Tracking by Magnetic Particle Imaging, Nano Lett 18(1) (2018) 182-189.
[57] B. Zheng, T. Vazin, P.W. Goodwill, A. Conway, A. Verma, E.U. Saritas, D. Schaffer, S.M. Conolly, Magnetic Particle Imaging tracks the long-term fate of in vivo neural cell implants with high image contrast, Sci Rep 5 (2015) 14055.

[58] S. Hildebrand, N. Lowa, H. Paysen, R.M. Fratila, L. Reverte-Salisa, T. Trakoolwilaiwan, Z. Niu, G. Kasparis, S.F. Preuss, O. Kosch, M.d.I.F. J, N.T.K. Thanh, F. Wiekhorst, A. Pfeifer, Quantification of Lipoprotein Uptake in Vivo Using Magnetic Particle Imaging and Spectroscopy, ACS Nano 15(1) (2021) 434-446.
[59] G. Song, M. Kenney, Y.S. Chen, X. Zheng, Y. Deng, Z. Chen, S.X. Wang, S.S. Gambhir, H. Dai, J. Rao, Carbon-coated FeCo nanoparticles as sensitive magnetic-particle-imaging tracers with photothermal and magnetothermal properties, Nat Biomed Eng 4(3) (2020) 325-334.
[60] X. Zhu, J. Li, P. Peng, N. Hosseini Nassab, B.R. Smith, Quantitative Drug Release Monitoring in Tumors of Living Subjects by Magnetic Particle Imaging Nanocomposite, Nano Lett 19(10) (2019) 6725-6733.
[61] W. Tong, H. Hui, W. Shang, Y. Zhang, F. Tian, Q. Ma, X. Yang, J. Tian, Y. Chen, Highly sensitive magnetic particle imaging of vulnerable atherosclerotic plaque with active myeloperoxidase-targeted nanoparticles, Theranostics 11(2) (2021) 506-521.
[62] J. Franke, N. Baxan, H. Lehr, U. Heinen, S. Reinartz, J. Schnorr, M. Heidenreich, F. Kiessling, V. Schulz, Hybrid MPI-MRI System for Dual-Modal In Situ Cardiovascular Assessments of Real-Time 3D Blood Flow Quantification-A Pre-Clinical In Vivo Feasibility Investigation, IEEE Trans Med Imaging 39(12) (2020) 4335-4345.
[63] R. Orendorff, A.J. Peck, B. Zheng, S.N. Shirazi, R. Matthew Ferguson, A.P. Khandhar, S.J. Kemp, P. Goodwill, K.M. Krishnan, G.A. Brooks, D. Kaufer, S. Conolly, First in vivo traumatic brain injury imaging via magnetic particle imaging, Phys Med Biol 62(9) (2017) 3501-3509.
[64] G. Song, X. Zheng, Y. Wang, X. Xia, S. Chu, J. Rao, A Magneto-Optical Nanoplatform for Multimodality Imaging of Tumors in Mice, ACS Nano 13(7) (2019) 7750-7758.
[65] N. Naseri, E. Ajorlou, F. Asghari, Y. Pilehvar-Soltanahmadi, An update on nanoparticle-based contrast agents in medical imaging, Artif Cells Nanomed Biotechnol 46(6) (2018) 1111-1121.
[66] W. Li, X. Chen, Gold nanoparticles for photoacoustic imaging, Nanomedicine (Lond) 10(2) (2015) 299-320.
[67] G.P. Luke, D. Yeager, S.Y. Emelianov, Biomedical applications of photoacoustic imaging with exogenous contrast agents, Ann Biomed Eng 40(2) (2012) 422-37.
[68] C. Lu, L. Han, J. Wang, J. Wan, G. Song, J. Rao, Engineering of magnetic nanoparticles as magnetic particle imaging tracers, Chem Soc Rev 50(14) (2021) 8102-8146.
[69] N. Talebloo, M. Gudi, N. Robertson, P. Wang, Magnetic Particle Imaging: Current Applications in Biomedical Research, J Magn Reson Imaging 51(6) (2020) 1659-1668.
[70] C. Billings, M. Langley, G. Warrington, F. Mashali, J.A. Johnson, Magnetic Particle Imaging: Current and Future Applications, Magnetic Nanoparticle Synthesis Methods and Safety Measures, Int J Mol Sci 22(14) (2021) 7651.
[71] A.S. Thakor, J.V. Jokerst, P. Ghanouni, J.L. Campbell, E. Mittra, S.S. Gambhir, Clinically Approved Nanoparticle Imaging Agents, J Nucl Med 57(12) (2016) 1833-1837.
[72] D.E. Owens, 3rd, N.A. Peppas, Opsonization, biodistribution, and pharmacokinetics of polymeric nanoparticles, Int J Pharm 307(1) (2006) 93-102.
[73] J. Shi, P.W. Kantoff, R. Wooster, O.C. Farokhzad, Cancer nanomedicine: progress, challenges and opportunities, Nat Rev Cancer 17(1) (2017) 20-37.

[74] F. Alexis, E. Pridgen, L.K. Molnar, O.C. Farokhzad, Factors affecting the clearance and biodistribution of polymeric nanoparticles, Mol Pharm 5(4) (2008) 505-15.
[75] L. Shi, J. Zhang, M. Zhao, S. Tang, X. Cheng, W. Zhang, W. Li, X. Liu, H. Peng, Q. Wang, Effects of polyethylene glycol on the surface of nanoparticles for targeted drug delivery, Nanoscale 13(24) (2021) 10748-10764.
[76] K.M. Tsoi, S.A. MacParland, X.Z. Ma, V.N. Spetzler, J. Echeverri, B. Ouyang, S.M. Fadel, E.A. Sykes, N. Goldaracena, J.M. Kaths, J.B. Conneely, B.A. Alman, M. Selzner, M.A. Ostrowski, O.A. Adeyi, A. Zilman, I.D. McGilvray, W.C. Chan, Mechanism of hard-nanomaterial clearance by the liver, Nat Mater 15(11) (2016) 1212-1221.
[77] C.P. Shih, X. Tang, C.W. Kuo, D.Y. Chueh, P. Chen, Design principles of bioinspired interfaces for biomedical applications in therapeutics and imaging, Front Chem 10 (2022) 990171.
[78] C.M. Hu, R.H. Fang, K.C. Wang, B.T. Luk, S. Thamphiwatana, D. Dehaini, P. Nguyen, P. Angsantikul, C.H. Wen, A.V. Kroll, C. Carpenter, M. Ramesh, V. Qu, S.H. Patel, J. Zhu, W. Shi, F.M. Hofman, T.C. Chen, W. Gao, K. Zhang, S. Chien, L. Zhang, Nanoparticle biointerfacing by platelet membrane cloaking, Nature 526(7571) (2015) 118-21.
[79] C. Jimenez-Jimenez, M. Manzano, M. Vallet-Regi, Nanoparticles Coated with Cell Membranes for Biomedical Applications, Biology (Basel) 9(11) (2020).
[80] B. Li, F. Wang, L. Gui, Q. He, Y. Yao, H. Chen, The potential of biomimetic nanoparticles for tumor-targeted drug delivery, Nanomedicine (Lond) 13(16) (2018) 2099-2118.
[81] J. Jin, Z.M. Bhujwalla, Biomimetic Nanoparticles Camouflaged in Cancer Cell Membranes and Their Applications in Cancer Theranostics, Front Oncol 9 (2019) 1560.
[82] M. Gao, C. Liang, X. Song, Q. Chen, Q. Jin, C. Wang, Z. Liu, Erythrocyte-Membrane-Enveloped Perfluorocarbon as Nanoscale Artificial Red Blood Cells to Relieve Tumor Hypoxia and Enhance Cancer Radiotherapy, Adv Mater 29(35) (2017).
[83] Q. Wang, Y. Ren, J. Mu, N.K. Egilmez, X. Zhuang, Z. Deng, L. Zhang, J. Yan, D. Miller, H.G. Zhang, Grapefruit-Derived Nanovectors Use an Activated Leukocyte Trafficking Pathway to Deliver Therapeutic Agents to Inflammatory Tumor Sites, Cancer Res 75(12) (2015) 2520-9.
[84] Y. Zhang, K. Cai, C. Li, Q. Guo, Q. Chen, X. He, L. Liu, Y. Zhang, Y. Lu, X. Chen, T. Sun, Y. Huang, J. Cheng, C. Jiang, Macrophage-Membrane-Coated Nanoparticles for Tumor-Targeted Chemotherapy, Nano Lett 18(3) (2018) 1908-1915.
[85] L. Alvarez-Erviti, Y. Seow, H. Yin, C. Betts, S. Lakhal, M.J. Wood, Delivery of siRNA to the mouse brain by systemic injection of targeted exosomes, Nat Biotechnol 29(4) (2011) 341-5.
[86] L. Brillault, P.V. Jutras, N. Dashti, E.C. Thuenemann, G. Morgan, G.P. Lomonossoff, M.J. Landsberg, F. Sainsbury, Engineering Recombinant Virus-like Nanoparticles from Plants for Cellular Delivery, ACS Nano 11(4) (2017) 3476-3484.
[87] L. Chen, H. Qin, R. Zhao, X. Zhao, L. Lin, Y. Chen, Y. Lin, Y. Li, Y. Qin, Y. Li, S. Liu, K. Cheng, H. Chen, J. Shi, G.J. Anderson, Y. Wu, Y. Zhao, G. Nie, Bacterial cytoplasmic membranes synergistically enhance the antitumor activity of autologous cancer vaccines, Sci Transl Med 13(601) (2021) eabc2816.
[88] X. Ai, M. Hu, Z. Wang, W. Zhang, J. Li, H. Yang, J. Lin, B. Xing, Recent Advances of Membrane-Cloaked Nanoplatforms for Biomedical Applications, Bioconjug Chem 29(4) (2018) 838-851.

[89] C. Wang, S. Wu, Research update on cell membrane camouflaged nanoparticles for cancer therapy, Front Bioeng Biotechnol 10 (2022) 944518.
[90] L. Rao, B. Cai, L.L. Bu, Q.Q. Liao, S.S. Guo, X.Z. Zhao, W.F. Dong, W. Liu, Microfluidic Electroporation-Facilitated Synthesis of Erythrocyte Membrane-Coated Magnetic Nanoparticles for Enhanced Imaging-Guided Cancer Therapy, ACS Nano 11(4) (2017) 3496-3505.
[91] L. Rao, Q.F. Meng, L.L. Bu, B. Cai, Q. Huang, Z.J. Sun, W.F. Zhang, A. Li, S.S. Guo, W. Liu, T.H. Wang, X.Z. Zhao, Erythrocyte Membrane-Coated Upconversion Nanoparticles with Minimal Protein Adsorption for Enhanced Tumor Imaging, ACS Appl Mater Interfaces 9(3) (2017) 2159-2168.
[92] Z. Liu, F. Wang, X. Liu, Y. Sang, L. Zhang, J. Ren, X. Qu, Cell membrane-camouflaged liposomes for tumor cell-selective glycans engineering and imaging in vivo, Proc Natl Acad Sci U S A 118(30) (2021) e2022769118.
[93] D. Dehaini, X. Wei, R.H. Fang, S. Masson, P. Angsantikul, B.T. Luk, Y. Zhang, M. Ying, Y. Jiang, A.V. Kroll, W. Gao, L. Zhang, Erythrocyte-Platelet Hybrid Membrane Coating for Enhanced Nanoparticle Functionalization, Adv Mater 29(16) (2017).
[94] S. Parveen, R. Misra, S.K. Sahoo, Nanoparticles: a boon to drug delivery, therapeutics, diagnostics and imaging, Nanomedicine 8(2) (2012) 147-66.
[95] P. Li, D. Wang, J. Hu, X. Yang, The role of imaging in targeted delivery of nanomedicine for cancer therapy, Adv Drug Deliv Rev 189 (2022) 114447.
[96] E.K. Chow, D. Ho, Cancer nanomedicine: from drug delivery to imaging, Sci Transl Med 5(216) (2013) 216rv4.
[97] M. Mir, S. Ishtiaq, S. Rabia, M. Khatoon, A. Zeb, G.M. Khan, A. Ur Rehman, F. Ud Din, Nanotechnology: from In Vivo Imaging System to Controlled Drug Delivery, Nanoscale Res Lett 12(1) (2017) 500.
[98] F. Cao, Z. Qiu, H. Li, P. Lai, Photoacoustic Imaging in Oxygen Detection, Applied Sciences 7(12) (2017) 1262.
[99] P. Lai, L. Wang, J.W. Tay, L.V. Wang, Photoacoustically guided wavefront shaping for enhanced optical focusing in scattering media, Nat Photonics 9(2) (2015) 126-132.
[100] Y. Liu, H. Liu, H. Yan, Y. Liu, J. Zhang, W. Shan, P. Lai, H. Li, L. Ren, Z. Li, L. Nie, Aggregation-Induced Absorption Enhancement for Deep Near-Infrared II Photoacoustic Imaging of Brain Gliomas In Vivo, Adv Sci (Weinh) 6(8) (2019) 1801615.
[101] J. Xia, J.J. Yao, L.V. Wang, Photoacoustic Tomography: Principles and Advances, Prog Electromagn Res 147 (2014) 1-22.
[102] H. Deng, W. Shang, G. Lu, P. Guo, T. Ai, C. Fang, J. Tian, Targeted and Multifunctional Technology for Identification between Hepatocellular Carcinoma and Liver Cirrhosis, ACS Appl Mater Interfaces 11(16) (2019) 14526-14537.
[103] Z. Yu, H. Li, P. Lai, Wavefront Shaping and Its Application to Enhance Photoacoustic Imaging, Applied Sciences 7(12) (2017) 1320.
[104] F. Bray, J. Ferlay, I. Soerjomataram, R.L. Siegel, L.A. Torre, A. Jemal, Global cancer statistics 2018: GLOBOCAN estimates of incidence and mortality worldwide for 36 cancers in 185 countries, CA Cancer J Clin 68(6) (2018) 394-424.

[105] Y. Liu, P. Lai, C. Ma, X. Xu, A.A. Grabar, L.V. Wang, Optical focusing deep inside dynamic scattering media with near-infrared time-reversed ultrasonically encoded (TRUE) light, Nat Commun 6 (2015) 5904.
[106] K.H. Song, C. Kim, C.M. Cobley, Y. Xia, L.V. Wang, Near-infrared gold nanocages as a new class of tracers for photoacoustic sentinel lymph node mapping on a rat model, Nano Lett 9(1) (2009) 183-8.
[107] J. Weber, P.C. Beard, S.E. Bohndiek, Contrast agents for molecular photoacoustic imaging, Nat Methods 13(8) (2016) 639-50.
[108] H. Yuan, C.G. Khoury, H. Hwang, C.M. Wilson, G.A. Grant, T. Vo-Dinh, Gold nanostars: surfactant-free synthesis, 3D modelling, and two-photon photoluminescence imaging, Nanotechnology 23(7) (2012) 075102.
[109] H. Chen, L. Shao, T. Ming, Z. Sun, C. Zhao, B. Yang, J. Wang, Understanding the photothermal conversion efficiency of gold nanocrystals, Small 6(20) (2010) 2272-80.
[110] D. Wu, L. Huang, M.S. Jiang, H. Jiang, Contrast agents for photoacoustic and thermoacoustic imaging: a review, Int J Mol Sci 15(12) (2014) 23616-39.
[111] Q. Fu, R. Zhu, J. Song, H. Yang, X. Chen, Photoacoustic Imaging: Contrast Agents and Their Biomedical Applications, Adv Mater 31(6) (2019) e1805875.
[112] C.G. Khoury, T. Vo-Dinh, Gold Nanostars For Surface-Enhanced Raman Scattering: Synthesis, Characterization and Optimization, J Phys Chem C Nanomater Interfaces 2008(112) (2008) 18849-18859.
[113] S.K. Libutti, G.F. Paciotti, A.A. Byrnes, H.R. Alexander, Jr., W.E. Gannon, M. Walker, G.D. Seidel, N. Yuldasheva, L. Tamarkin, Phase I and pharmacokinetic studies of CYT-6091, a novel PEGylated colloidal gold-rhTNF nanomedicine, Clin Cancer Res 16(24) (2010) 6139-49.
[114] S. Wang, P. Huang, L. Nie, R. Xing, D. Liu, Z. Wang, J. Lin, S. Chen, G. Niu, G. Lu, X. Chen, Single continuous wave laser induced photodynamic/plasmonic photothermal therapy using photosensitizer-functionalized gold nanostars, Adv Mater 25(22) (2013) 3055-61.
[115] J. An, X.Q. Yang, K. Cheng, X.L. Song, L. Zhang, C. Li, X.S. Zhang, Y. Xuan, Y.Y. Song, B.Y. Fang, X.L. Hou, Y.D. Zhao, B. Liu, In Vivo Computed Tomography/Photoacoustic Imaging and NIR-Triggered Chemo-Photothermal Combined Therapy Based on a Gold Nanostar-, Mesoporous Silica-, and Thermosensitive Liposome-Composited Nanoprobe, ACS Appl Mater Interfaces 9(48) (2017) 41748-41759.
[116] V. Raghavan, C. O'Flatharta, R. Dwyer, A. Breathnach, H. Zafar, P. Dockery, A. Wheatley, I. Keogh, M. Leahy, M. Olivo, Dual plasmonic gold nanostars for photoacoustic imaging and photothermal therapy, Nanomedicine (Lond) 12(5) (2017) 457-471.
[117] W. Li, X. Sun, Y. Wang, G. Niu, X. Chen, Z. Qian, L. Nie, In vivo quantitative photoacoustic microscopy of gold nanostar kinetics in mouse organs, Biomed Opt Express 5(8) (2014) 2679-85.
[118] K. Yang, S. Zhang, G. Zhang, X. Sun, S.T. Lee, Z. Liu, Graphene in mice: ultrahigh in vivo tumor uptake and efficient photothermal therapy, Nano Lett 10(9) (2010) 3318-23.
[119] A.M. Gobin, M.H. Lee, N.J. Halas, W.D. James, R.A. Drezek, J.L. West, Near-infrared resonant nanoshells for combined optical imaging and photothermal cancer therapy, Nano Lett 7(7) (2007) 1929-34.

[120] B. Jang, L. Xu, M.S. Moorthy, W. Zhang, L. Zeng, M. Kang, M. Kwak, J. Oh, J.O. Jin, Lipopolysaccharide-coated CuS nanoparticles promoted anti-cancer and anti-metastatic effect by immuno-photothermal therapy, Oncotarget 8(62) (2017) 105584-105595.
[121] S. Kumari, N. Sharma, S.V. Sahi, Advances in Cancer Therapeutics: Conventional Thermal Therapy to Nanotechnology-Based Photothermal Therapy, Pharmaceutics 13(8) (2021) 1174.
[122] J. Wang, Y. Xie, L. Wang, J. Tang, J. Li, D. Kocaefe, Y. Kocaefe, Z. Zhang, Y. Li, C. Chen, In vivo pharmacokinetic features and biodistribution of star and rod shaped gold nanoparticles by multispectral optoacoustic tomography, RSC Advances 5(10) (2015) 7529-7538.
[123] N. Desai, Challenges in development of nanoparticle-based therapeutics, AAPS J 14(2) (2012) 282-95.
[124] H.H. Gustafson, D. Holt-Casper, D.W. Grainger, H. Ghandehari, Nanoparticle Uptake: The Phagocyte Problem, Nano Today 10(4) (2015) 487-510.
[125] Y. Han, R. Zhao, F. Xu, Neutrophil-Based Delivery Systems for Nanotherapeutics, Small 14(42) (2018) e1801674.
[126] P. Zhang, G. Liu, X. Chen, Nanobiotechnology: Cell Membrane-Based Delivery Systems, Nano Today 13 (2017) 7-9.
[127] S. de Oliveira, C. Saldanha, An overview about erythrocyte membrane, Clin Hemorheol Microcirc 44(1) (2010) 63-74.
[128] P. Lv, X. Liu, X. Chen, C. Liu, Y. Zhang, C. Chu, J. Wang, X. Wang, X. Chen, G. Liu, Genetically Engineered Cell Membrane Nanovesicles for Oncolytic Adenovirus Delivery: A Versatile Platform for Cancer Virotherapy, Nano Lett 19(5) (2019) 2993-3001.
[129] R.H. Fang, Y. Jiang, J.C. Fang, L. Zhang, Cell membrane-derived nanomaterials for biomedical applications, Biomaterials 128 (2017) 69-83.
[130] P.A. Oldenborg, Role of CD47 as a Marker of Self on Red Blood Cells, Science 288(5473) (2000) 2051-2054.
[131] W. Chen, K. Zeng, H. Liu, J. Ouyang, L. Wang, Y. Liu, H. Wang, L. Deng, Y.-N. Liu, Cell Membrane Camouflaged Hollow Prussian Blue Nanoparticles for Synergistic Photothermal-/Chemotherapy of Cancer, Advanced Functional Materials 27(11) (2017) 1605795.
[132] H. Ding, Y. Lv, D. Ni, J. Wang, Z. Tian, W. Wei, G. Ma, Erythrocyte membrane-coated NIR-triggered biomimetic nanovectors with programmed delivery for photodynamic therapy of cancer, Nanoscale 7(21) (2015) 9806-15.
[133] L. Gao, H. Wang, L. Nan, T. Peng, L. Sun, J. Zhou, Y. Xiao, J. Wang, J. Sun, W. Lu, L. Zhang, Z. Yan, L. Yu, Y. Wang, Erythrocyte Membrane-Wrapped pH Sensitive Polymeric Nanoparticles for Non-Small Cell Lung Cancer Therapy, Bioconjug Chem 28(10) (2017) 2591-2598.
[134] L. Rao, L.L. Bu, J.H. Xu, B. Cai, G.T. Yu, X. Yu, Z. He, Q. Huang, A. Li, S.S. Guo, W.F. Zhang, W. Liu, Z.J. Sun, H. Wang, T.H. Wang, X.Z. Zhao, Red Blood Cell Membrane as a Biomimetic Nanocoating for Prolonged Circulation Time and Reduced Accelerated Blood Clearance, Small 11(46) (2015) 6225-36.
[135] C.M. Hu, L. Zhang, S. Aryal, C. Cheung, R.H. Fang, L. Zhang, Erythrocyte membrane-camouflaged polymeric nanoparticles as a biomimetic delivery platform, Proc Natl Acad Sci U S A 108(27) (2011) 10980-5.

[136] Q. Cui, B. Xia, S. Mitzscherling, A. Masic, L. Li, M. Bargheer, H. Möhwald, Preparation of gold nanostars and their study in selective catalytic reactions, Colloids and Surfaces A: Physicochemical and Engineering Aspects 465 (2015) 20-25.
[137] N.G. Sosale, K.R. Spinler, C. Alvey, D.E. Discher, Macrophage engulfment of a cell or nanoparticle is regulated by unavoidable opsonization, a species-specific 'Marker of Self' CD47, and target physical properties, Curr Opin Immunol 35 (2015) 107-12.
[138] Y. Wu, M.R.K. Ali, K. Chen, N. Fang, M.A. El-Sayed, Gold nanoparticles in biological optical imaging, Nano Today 24 (2019) 120-140.
[139] S. Wilhelm, A.J. Tavares, Q. Dai, S. Ohta, J. Audet, H.F. Dvorak, W.C.W. Chan, Analysis of nanoparticle delivery to tumours, Nature Reviews Materials 1(5) (2016) 16014.
[140] H. Chen, X. Zhang, S. Dai, Y. Ma, S. Cui, S. Achilefu, Y. Gu, Multifunctional gold nanostar conjugates for tumor imaging and combined photothermal and chemo-therapy, Theranostics 3(9) (2013) 633-49.
[141] L.V. Wang, Multiscale photoacoustic microscopy and computed tomography, Nat Photonics 3(9) (2009) 503-509.
[142] D.N. Louis, A. Perry, P. Wesseling, D.J. Brat, I.A. Cree, D. Figarella-Branger, C. Hawkins, H.K. Ng, S.M. Pfister, G. Reifenberger, R. Soffietti, A. von Deimling, D.W. Ellison, The 2021 WHO Classification of Tumors of the Central Nervous System: a summary, Neuro Oncol 23(8) (2021) 1231-1251.
[143] G. Abdalla, A. Hammam, M. Anjari, D.F. D'Arco, D.S. Bisdas, Glioma surveillance imaging: current strategies, shortcomings, challenges and outlook, BJR Open 2(1) (2020) 20200009.
[144] I. Ceravolo, G. Barchetti, F. Biraschi, C. Gerace, E. Pampana, A. Pingi, A. Stasolla, Early stage glioblastoma: retrospective multicentric analysis of clinical and radiological features, Radiol Med 126(11) (2021) 1468-1476.
[145] Y. Zhou, X. Huang, J. Li, T. Zhu, W. Pang, L. Chow, L. Nie, L. Sun, P. Lai, Small Animal In Situ Drug Delivery Effects via Transdermal Microneedles Array versus Intravenous Injection: A Pilot Observation Based on Photoacoustic Tomography, Pharmaceutics 14(12) (2022) 2689.
[146] Y. Zhou, J. Ni, C. Wen, P. Lai, Light on osteoarthritic joint: from bench to bed, Theranostics 12(2) (2022) 542-557.
[147] K.J. Langen, C. Watts, Neuro-oncology: Amino acid PET for brain tumours - ready for the clinic?, Nat Rev Neurol 12(7) (2016) 375-6.
[148] A. Vartanian, S.K. Singh, S. Agnihotri, S. Jalali, K. Burrell, K.D. Aldape, G. Zadeh, GBM's multifaceted landscape: highlighting regional and microenvironmental heterogeneity, Neuro Oncol 16(9) (2014) 1167-75.
[149] P. Waliszewski, J. Konarski, The Gompertzian curve reveals fractal properties of tumor growth, Chaos, Solitons & Fractals 16(5) (2003) 665-674.
[150] Z.W. Tay, P. Chandrasekharan, B.D. Fellows, I.R. Arrizabalaga, E. Yu, M. Olivo, S.M. Conolly, Magnetic Particle Imaging: An Emerging Modality with Prospects in Diagnosis, Targeting and Therapy of Cancer, Cancers (Basel) 13(21) (2021) 5285.
[151] A. Chiu-Lam, E. Staples, C.J. Pepine, C. Rinaldi, Perfusion, cryopreservation, and nanowarming of whole hearts using colloidally stable magnetic cryopreservation agent solutions, Sci Adv 7(2) (2021).

[152] C. Billings, M. Langley, G. Warrington, F. Mashali, J.A. Johnson, Magnetic Particle Imaging: Current and Future Applications, Magnetic Nanoparticle Synthesis Methods and Safety Measures, Int J Mol Sci 22(14) (2021).
[153] P. Szwargulski, M. Wilmes, E. Javidi, F. Thieben, M. Graeser, M. Koch, C. Gruettner, G. Adam, C. Gerloff, T. Magnus, T. Knopp, P. Ludewig, Monitoring Intracranial Cerebral Hemorrhage Using Multicontrast Real-Time Magnetic Particle Imaging, ACS Nano 14(10) (2020) 13913-13923.
[154] Z.W. Tay, P. Chandrasekharan, X.Y. Zhou, E. Yu, B. Zheng, S. Conolly, In vivo tracking and quantification of inhaled aerosol using magnetic particle imaging towards inhaled therapeutic monitoring, Theranostics 8(13) (2018) 3676-3687.
[155] Z. Jiang, X. Han, Y. Du, Y. Li, Y. Li, J. Li, J. Tian, A. Wu, Mixed Metal Metal-Organic Frameworks Derived Carbon Supporting ZnFe2O4/C for High-Performance Magnetic Particle Imaging, Nano Lett 21(7) (2021) 2730-2737.
[156] J. Zhuo, Y. Wang, H. Hui, C. Li, J. Yang, P. Zhang, C. Fang, J. Tian, Enhanced glypican-3-targeted identification of hepatocellular carcinoma with liver fibrosis by pre-degrading excess fibrotic collagen, Acta Biomater (2023).
[157] Z.W. Tay, S. Savliwala, D.W. Hensley, K.L.B. Fung, C. Colson, B.D. Fellows, X. Zhou, Q. Huynh, Y. Lu, B. Zheng, P. Chandrasekharan, S.M. Rivera-Jimenez, C.M. Rinaldi-Ramos, S.M. Conolly, Superferromagnetic Nanoparticles Enable Order-of-Magnitude Resolution & Sensitivity Gain in Magnetic Particle Imaging, Small Methods 5(11) (2021) e2100796.
[158] M. Irfan, N. Dogan, A. Bingolbali, F. Aliew, Synthesis and characterization of NiFe2O4 magnetic nanoparticles with different coating materials for magnetic particle imaging (MPI), Journal of Magnetism and Magnetic Materials 537 (2021).
[159] N. Dogan, O.M. Dogan, M. Irfan, F. Ozel, A.S. Kamzin, V.G. Semenov, I.V. Buryanenko, Manganese doped-iron oxide nanoparticles and their potential as tracer agents for magnetic particle imaging (MPI), Journal of Magnetism and Magnetic Materials 561 (2022).
[160] S. Liu, A. Chiu-Lam, A. Rivera-Rodriguez, R. DeGroff, S. Savliwala, N. Sarna, C.M. Rinaldi-Ramos, Long circulating tracer tailored for magnetic particle imaging, Nanotheranostics 5(3) (2021) 348-361.
[161] R. Molinaro, C. Corbo, J.O. Martinez, F. Taraballi, M. Evangelopoulos, S. Minardi, I.K. Yazdi, P. Zhao, E. De Rosa, M.B. Sherman, A. De Vita, N.E. Toledano Furman, X. Wang, A. Parodi, E. Tasciotti, Biomimetic proteolipid vesicles for targeting inflamed tissues, Nat Mater 15(9) (2016) 1037-46.
[162] S.K. Golombek, J.N. May, B. Theek, L. Appold, N. Drude, F. Kiessling, T. Lammers, Tumor targeting via EPR: Strategies to enhance patient responses, Adv Drug Deliv Rev 130 (2018) 17-38.
[163] X.-F. Bai, Y. Chen, M.-Z. Zou, C.-X. Li, Y. Zhang, M.-J. Li, S.-X. Cheng, X.-Z. Zhang, Homotypic Targeted Photosensitive Nanointerferer for Tumor Cell Cycle Arrest to Boost Tumor Photoimmunotherapy, ACS Nano (2022).
[164] K. Wiwatchaitawee, J.C. Quarterman, S.M. Geary, A.K. Salem, Enhancement of Therapies for Glioblastoma (GBM) Using Nanoparticle-based Delivery Systems, AAPS PharmSciTech 22(2) (2021) 71.

[165] X. Huang, W. Shang, H. Deng, Y. Zhou, F. Cao, C. Fang, P. Lai, J. Tian, Clothing spiny nanoprobes against the mononuclear phagocyte system clearance in vivo: Photoacoustic diagnosis and photothermal treatment of early stage liver cancer with erythrocyte membrane-camouflaged gold nanostars, Applied Materials Today 18 (2020).
[166] J.C. Harris, M.A. Scully, E.S. Day, Cancer Cell Membrane-Coated Nanoparticles for Cancer Management, Cancers (Basel) 11(12) (2019).
[167] Y. Yang, Z. Yan, D. Wei, J. Zhong, L. Liu, L. Zhang, F. Wang, X. Wei, C. Xie, W. Lu, D. He, Tumor-penetrating peptide functionalization enhances the anti-glioblastoma effect of doxorubicin liposomes, Nanotechnology 24(40) (2013) 405101.
[168] Y. Zhang, M. Yang, N.G. Portney, D. Cui, G. Budak, E. Ozbay, M. Ozkan, C.S. Ozkan, Zeta potential: a surface electrical characteristic to probe the interaction of nanoparticles with normal and cancer human breast epithelial cells, Biomed Microdevices 10(2) (2008) 321-8.
[169] M.K. Rasmussen, J.N. Pedersen, R. Marie, Size and surface charge characterization of nanoparticles with a salt gradient, Nature Communications 11(1) (2020).
[170] L. Kiru, A. Zlitni, A.M. Tousley, G.N. Dalton, W. Wu, F. Lafortune, A. Liu, K.M. Cunanan, H. Nejadnik, T. Sulchek, M.E. Moseley, R.G. Majzner, H.E. Daldrup-Link, In vivo imaging of nanoparticle-labeled CAR T cells, Proc Natl Acad Sci U S A 119(6) (2022).
[171] X. Zhu, W. Feng, J. Chang, Y.W. Tan, J. Li, M. Chen, Y. Sun, F. Li, Temperature-feedback upconversion nanocomposite for accurate photothermal therapy at facile temperature, Nat Commun 7 (2016) 10437.
[172] J. Jin, B. Krishnamachary, J.D. Barnett, S. Chatterjee, D. Chang, Y. Mironchik, F. Wildes, E.M. Jaffee, S. Nimmagadda, Z.M. Bhujwalla, Human Cancer Cell Membrane-Coated Biomimetic Nanoparticles Reduce Fibroblast-Mediated Invasion and Metastasis and Induce T-Cells, ACS Appl Mater Interfaces 11(8) (2019) 7850-7861.
[173] E.L. Giudice, J.D. Campbell, Needle-free vaccine delivery, Adv Drug Deliver Rev 58(1) (2006) 68-89.
[174] Y.C. Kim, J.H. Park, M.R. Prausnitz, Microneedles for drug and vaccine delivery, Adv Drug Deliver Rev 64(14) (2012) 1547-1568.
[175] S.H. Bariya, M.C. Gohel, T.A. Mehta, O.P. Sharma, Microneedles: an emerging transdermal drug delivery system, J Pharm Pharmacol 64(1) (2012) 11-29.
[176] K. Lee, H. Jung, Drawing lithography for microneedles: A review of fundamentals and biomedical applications, Biomaterials 33(30) (2012) 7309-7326.
[177] J. Yang, X.L. Liu, Y.Z. Fu, Y.J. Song, Recent advances of microneedles for biomedical applications: drug delivery and beyond, Acta Pharm Sin B 9(3) (2019) 469-483.
[178] S. Indermun, R. Luttge, Y.E. Choonara, P. Kumar, L.C. du Toit, G. Modi, V. Pillay, Current advances in the fabrication of microneedles for transdermal delivery, J Control Release 185 (2014) 130-138.
[179] J.E. Millstone, S. Park, K.L. Shuford, L. Qin, G.C. Schatz, C.A. Mirkin, Observation of a quadrupole plasmon mode for a colloidal solution of gold nanoprisms, J Am Chem Soc 127(15) (2005) 5312-3.
[180] J.W. Lee, M.R. Han, J.H. Park, Polymer microneedles for transdermal drug delivery, J Drug Target 21(3) (2013) 211-223.

[181] Z. Wang, Z. Yang, J. Jiang, Z. Shi, Y. Mao, N. Qin, T.H. Tao, Silk Microneedle Patch Capable of On-Demand Multidrug Delivery to the Brain for Glioblastoma Treatment, Adv Mater 34(1) (2022) e2106606.
[182] J.Y. Li, Y.Y. Zhou, J.B. Yang, R. Ye, J. Gao, L. Ren, B. Liu, L. Liang, L.L. Jiang, Fabrication of gradient porous microneedle array by modified hot embossing for transdermal drug delivery, Mat Sci Eng C-Mater 96 (2019) 576-582.
[183] S.P. Davis, W. Martanto, M.G. Allen, M.R. Prausnitz, Hollow metal microneedles for insulin delivery to diabetic rats, Ieee T Bio-Med Eng 52(5) (2005) 909-915.
[184] D.M. Close, T.T. Xu, G.S. Sayler, S. Ripp, In Vivo Bioluminescent Imaging (BLI): Noninvasive Visualization and Interrogation of Biological Processes in Living Animals, Sensors-Basel 11(1) (2011) 180-206.
[185] L.V. Wang, Prospects of photoacoustic tomography, Med Phys 35(12) (2008) 5758-67.
[186] S. Mallidi, G.P. Luke, S. Emelianov, Photoacoustic imaging in cancer detection, diagnosis, and treatment guidance, Trends Biotechnol 29(5) (2011) 213-221.
[187] G.P. Luke, S.Y. Nam, S.Y. Emelianov, Optical wavelength selection for improved spectroscopic photoacoustic imaging, Photoacoustics 1(2) (2013) 36-42.
[188] M. Moothanchery, R.Z. Seeni, C. Xu, M. Pramanik, In vivo studies of transdermal nanoparticle delivery with microneedles using photoacoustic microscopy, Biomedical Optics Express 8(12) (2017).
[189] S.C. Yu, Y.F. Ping, L. Yi, Z.H. Zhou, H.H. Chen, X.H. Yao, L. Gao, J.M. Wang, X.W. Bian, Isolation and characterization of cancer stem cells from a human glioblastoma cell line U87, Cancer Lett 265(1) (2008) 124-134.
[190] M. Candolfi, J.F. Curtin, W.S. Nichols, A.K.M.G. Muhammad, G.D. King, G.E. Pluhar, E.A. McNiel, J.R. Ohlfest, A.B. Freese, P.F. Moore, J. Lerner, P.R. Lowenstein, M.G. Castro, Intracranial glioblastoma models in preclinical neuro-oncology: neuropathological characterization and tumor progression, J Neuro-Oncol 85(2) (2007) 133-148.
[191] N. Hite, A. Klinger, L. Hellmers, G.A. Maresh, P.E. Miller, X. Zhang, L. Li, D.A. Margolin, An optimal orthotopic mouse model for human colorectal cancer primary tumor growth and spontaneous metastasis, Diseases of the Colon & Rectum 61(6) (2018) 698-705.
[192] H. Du, P. Liu, J. Zhu, J. Lan, Y. Li, L. Zhang, J. Zhu, J. Tao, Hyaluronic Acid-Based Dissolving Microneedle Patch Loaded with Methotrexate for Improved Treatment of Psoriasis, ACS Applied Materials & Interfaces 11(46) (2019) 43588-43598.
[193] X. Zhao, X. Li, P. Zhang, J. Du, Y. Wang, Tip-loaded fast-dissolving microneedle patches for photodynamic therapy of subcutaneous tumor, J Control Release 286 (2018) 201-209.
[194] P.P. Yang, M.L. Chen, W.B. Qin, C.N. Shi, X.Q. Bai, G.L. Quan, X. Pan, C.B. Wu, Effective Photothermal Therapy Mediated by Indocyanine Green Nanoparticle Tip-Loaded Microneedles to Enhance Checkpoint Inhibitor Immunotherapy for Melanoma Treatment, Acs Appl Nano Mater 4(6) (2021) 5921-5931.
[195] B. Bediz, E. Korkmaz, R. Khilwani, C. Donahue, G. Erdos, L.D. Falo, O.B. Ozdoganlar, Dissolvable Microneedle Arrays for Intradermal Delivery of Biologics: Fabrication and Application, Pharm Res-Dordr 31(1) (2014) 117-135.

[196] M. Capozza, F. Blasi, G. Valbusa, P. Oliva, C. Cabella, F. Buonsanti, A. Cordaro, L. Pizzuto, A. Maiocchi, L. Poggi, Photoacoustic imaging of integrin-overexpressing tumors using a novel ICG-based contrast agent in mice, Photoacoustics 11 (2018) 36-45.